Interactions of single nanoparticles with microelectrode surfaces

(Wechselwirkung einzelner Nanopartikel mit Oberflächen von Mikroelektroden)

Von der Fakultät für Mathematik und Naturwissenschaften
der Carl von Ossietzky Universität Oldenburg
zur Erlangung des Grades und Titels eines

Doktors der Naturwissenschaften (Dr. rer. nat.)
angenommene Dissertation

von Herrn **Abdallatif Alshalfouh**, M.Sc.
geboren am 05.01.1988 in Libyen

Oldenburg, September 2020

This research was done from April 2016 to August 2020 at the Carl von Ossietzky University of Oldenburg, School of Mathematics and Sciences, Department of Chemistry, under the supervision of Prof. Dr. Gunther Wittstock and PD Dr. Carsten Dosche. The results of this project were presented in different international and local conferences. Part of these results was published in ChemElectroChem journal. This project was funded by Deutsche Akademische Austausch Dienst (DAAD).

Erstgutachter: Prof. Dr. Gunther Wittstock

Zweitgutachter: Prof. Dr. Michael Wark

Tag der Disputation: 07.12.2020

Table of contents

Abstract…… II

Zusammenfassung…… III

Acknowledgements…….. V

Contents…… VI

Abbreviations…… IX

Symbols……. X

Abstract

Nanoparticles (NPs) have emerged as active materials for various technically relevant processes like photochemistry, electrochemistry, and catalysis. Although numerous studies have been reported on the redox chemistry and electrochemistry of NPs, the dynamics and kinetics of individual NPs at electrode surfaces are still poorly understood to date. The electrochemistry of the NPs becomes more complicated at size of nanoscale. It is not clear till now if the oxidation of the particles < 10 nm will lead to a complete dissolution in a single collision or just like the bigger one > 10 nm require a sequence of collisions for complete oxidative dissolution. To understand the behaviour of the extremely small NPs under the oxidation, more information about adsorption and desorption of NPs on the electrode surface, resting times and kinetics of NPs modification or degradation process are required. In order to obtain such information, the electrochemical reactivity of luminiscent NPs has been investigated in this work on a platinum microelectrode (ME) surface using fluorescence correlation spectroscopy (FCS). Single CdSe/CdS QDs with negative surface charge and Ag-Au NPs with cytidine shell were used as examples for semiconductor and fluorescent metallic NPs, respectively. The results show that QDs are irreversibly oxidized in aqueous solution. However, the correlation time and average number of particles retrieved from FCS suggest that the QDs do not lose their emissive properties in a single collision and desorb from the electrode surface without being decomposed significantly. FCS also showed that half of accumulated Ag-Au NPs at the electrode surface are completely oxidized. So far, the direct single NP collision experiments with direct NP transformation produces Faradaic current very close to the background current, defining number of sequences that NPs need to disappear completely was not succeeded. Furthermore, this method was restricted to the fluorescent NPs. The events of NPs at the electrode surface were studied further indirectly via another readout. For this purpose, the conventional electrochemistry that was coupled with fluorescence spectroscopy was replaced by bipolar electrochemistry.The ability of this method to detect very small concentrations and overcome the fluorescence background was checked before going further to study single NPs collision. The detection limit of FcMeOH was found to be 10 µM which is not more sensitive than the electrochemical method.

Zusammenfassung

Nanopartikel (NPs) haben sich als aktive Materialien für verschiedene technisch relevante Prozesse wie Photochemie, Elektrochemie und Katalyse herausgestellt. Obwohl zahlreiche Studien zur Redoxchemie und Elektrochemie von NPs veröffentlicht wurden, sind die Dynamik und Kinetik einzelner NPs an Elektrodenoberflächen bislang noch wenig bekannt. Die Elektrochemie der NPs wird bei nanoskaligen Größen komplizierter. Es ist bis jetzt nicht klar, ob die Oxidation der Partikel < 10 nm zu einer vollständigen Auflösung in einer einzelnen Kollision führt oder genau wie die größeren (> 10 nm) eine Folge von Kollisionen für eine vollständige oxidative Auflösung erfordert. Um das Verhalten der extrem kleinen NPs während der Oxidation zu verstehen, sind weitere Informationen über die Adsorption und Desorption von NPs auf der Elektrodenoberfläche, die Ruhezeiten und die Kinetik der Modifikation oder des Abbauprozesses von NPs erforderlich. Um solche Informationen zu erhalten, wurde in dieser Arbeit die elektrochemische Reaktivität von leuchtenden NPs auf einer Platin-Mikroelektroden (ME) -Oberfläche unter Verwendung von fluoreszenz korrelation spektroskopie (FCS) untersucht. Einzelne CdSe / CdS-QDs mit negativer Oberflächenladung und Ag-Au-NPs mit Cytidinhülle wurden als Beispiele für Halbleiter und fluoreszierende metallische NPs verwendet. Die Ergebnisse zeigen, dass QDs in wässriger Lösung irreversibel oxidiert werden. Die Korrelationszeit und die durchschnittliche Anzahl der aus FCS Abgerufen Partikel legen jedoch nahe, dass die QDs bei einer einzigen Kollision ihre Emissionseigenschaften nicht verlieren und von der Elektrodenoberfläche desorbieren, ohne signifikant zersetzt zu werden. FCS zeigte auch, dass die Hälfte der an der Elektrodenoberfläche akkumulierten Ag-Au-NPs vollständig oxidiert ist. Bisher erzeugen die direkten Einzel-NP-Kollisionsexperimente mit direkter NP-Transformation einen Faradayschen Strom, der sehr nahe am Hintergrundstrom liegt. Es ist uns nicht gelungen, die Anzahl der Sequenzen zu definieren, die NP benötigen, um vollständig zu verschwinden. Darüber hinaus war diese Methode auf die fluoreszierenden NPs beschränkt. Die Ereignisse von NPs an der Elektrodenoberfläche wurden indirekt über eine andere Anzeige weiter untersucht. Zu diesem Zweck wurde die konventionelle Elektrochemie, die mit Fluoreszenzspektroskopie gekoppelt war, durch bipolare Elektrochemie ersetzt. Die Fähigkeit dieser Methode, sehr kleine Konzentrationen nachzuweisen und den Fluoreszenzhintergrund zu überwinden, wurde überprüft, bevor die Kollision einzelner NPs weiter untersucht wurde.

Es wurde gefunden, dass die Nachweisgrenze von FcMeOH 10 µM beträgt, was nicht empfindlicher als das elektrochemische Verfahren ist.

Acknowledgements

I would like to express the deepest appreciation to my supervisors, Prof. Dr. Gunther Wittstock and Dr. Carsten Dosche for the continuous support of my PhD study and research, for their patience, motivation, enthusiasm and immense knowledge. Their guidance helped me in all the time of research and writing of this thesis. I could not have imagined having a better advisor and mentor for my PhD study.

Beside my supervisors, I would like to thank anybody who has provided me with information either in our group or another groups. Particularly, I thank Gerd Gertjegerdes and Björn Mageney who have helped me with the adjusting my setup and the electronic connections. I thank also Deutscher Akademischer Austausch Dienst (DAAD) for funding the PhD thesis.

My sincere thanks also go to my parents in Gaza for giving birth to me at the first place and supporting me spiritually and materially throughout my life. Furthermore, my thanks for their patience of my travelling abroad.

My great regards for my wife (Heba) and my daughters (Layan, Alaa, Bayan, Hala and Zina) for patience and helpful. I have spent long times in the university and left them long times at home without me. I thank my wife from the deep of my heart where she has had took a care with five kids and made a scientific weather for me without any trouble.

Contents

1 Introduction 1
2 Theory and background 6
2.1 Fluorescence phenomena 6
2.1.1 The fundamentals of fluorescence 6
2.1.2 Fluorescence lifetime and quantum yields 7
2.1.3 Overview of luminescent NPs 8
2.1.4 Blinking and quenching phenomena 14
2.2 Single molecule spectroscopy 17
2.2.1 Single molecule detection (SMD) 17
2.2.2 Fluorescence correlation spectroscopy (FCS) 19
2.2.3 Kinetic investigations by FCS 25
2.2.4 Setup description 25
2.3 Microelectrodes 28
2.4 Single entity collision electrochemistry 32
2.4.1 The principle of single entity collision 32
2.4.2 Detection by redox cycling 33
2.4.3 Detection by catalytic amplification 34
2.4.4 Detection by partial conversion 36
2.4.5 Detection by blocking 38
2.4.6 Single entity collision recording 39
2.4.7 Optical detection strategy 40
2.5 Bipolar electrochemistry 42
2.5.1 Overview on bipolar electrochemistry 42
2.5.2 Microelectrochemical application of bipolar electrochemistry 44
2.5.3 Coupling bipolar electrochemistry and optical detection 48
3 Experimental 52
3.1 Chemicals and materials 52
3.2 Quantum dots and metallic nanoparticles 53
3.2.1 Preparation 53
3.2.2 Spectroscopic characterization 54
3.2.3 Electrochemical investigation 54
3.3 Electrochemical techniques for signal recording of charge transfer 55

3.3.1 Chronoamperometry 55
3.3.2 Stripping measurements 55
3.4 Microelectrodes 56
3.4.1 Fabrication of ME 56
3.4.2 Characterization 57
3.4.3 Platinum deposition on microelectrodes 58
3.5 Combining conventional electrochemistry with single molecule fluorescence spectroscopy 58
3.5.1 Single molecule spectro-electrochemical setup description 58
3.5.2 Data analysis and fitting parameter 59
3.5.3 Time correlated single photon counting (TCSPC) 60
3.6 Combining bipolar electrochemistry with fluorescence spectroscopy 62
3.6.1 Setups description 62
3.6.2 Cyclic voltammetry by bipolar electrode 64
3.6.3 Measurement of the oxidation of FcMeOH and commercial QDs 64
3.6.4 Preparation of Tris(bipyridine)ruthenium (III) chloride 65
3.6.5 Data processing 66
4 Results and discussion 68
4.1 Spectroscopic characterization of CdSe/CdS QDs and Ag NPs 68
4.1.1 Transmission electron microscopy (TEM) 68
4.1.2 Absorption and emission characterization 70
4.2 Electrochemical characterization of CdSe/CdS QDs and Ag NPs 73
4.2.1 Cyclic voltammetry 74
4.2.2 Differential pulse voltammetry 78
4.3 Electrochemical signal recording 80
4.4 Microelectrode improvements 84
4.5 Characterizing of CdSe-CdS QDs with single molecule fluorescence spectroscopy 86
4.5.1 FCS measurements at different *z* axis distances of the confocal volume 86
4.5.2 Diffusion coefficient for QDs and metallic NPs 88
4.5.3 The effect of the laser power on QDs inside the confocal volume 90
4.5.4 The relation between the supporting electrode and aggregation effect 91
4.6 Electrochemistry of QDs and Ag NPs studied by single molecule fluorescence spectroscopy 92
4.6.1 FCS of QDs at Pt microelectrode at open circuit potential 92
4.6.2 Photoluminescence emission decay of QDs under potentiostatically controlled Pt microelectrode 95

4.6.3 FCS of QDs under potentiostatically controlled Pt microelectrode.....98
4.6.4 FCS of Ag NPs under potentiostatically controlled Pt microelectrode 103
4.6.5 Simulation output.....104
4.7 Studying the interaction of redoxactive species at the electrode surface by bipolar electrochemistry 107
4.7.1 Motivation of coupling the bipolar electrochemistry with fluorescence spectroscopy 107
4.7.2 Observation of the limitating current by cyclic voltammetry.....108
4.7.3 Determining the detection limit of FcMeOH by using BPE.....111
4.7.4 Suitable dye used as a reporter for the oxidation of NPs.....114
4.7.5 Titration of Ru(II) by absorption and emission spectroscopy 117
5 Conclusion and outlook.....122
6 References 127

Abbreviations

AFM	Atomic force microscopy
BPE	Bipolar electrochemistry
BE	Bipolar electrode
DFM	Dark field microscopy
S_n	excited singlet state
FcMeOH	Ferrocene methanol
FCS	Fluorescence correlation spectroscopy
FCCS	Fluorescence cross correlation spectroscopy
FWHM	Full width at half maximum
S_0	Singlet ground state
LNPs	Luminescent nanoparticles
MNPs	Metallic nanoparticles
ME	Microelectrode
NPs	Nanoparticles
SECCM	Scanning electrochemical cell microscope
SECM	Scanning electrochemical microscopy
STM	Scanning tunneling microscopy
QDs	Semiconductor quantum dots
SNR	Signal-to-noise-ratio
SEC	Single entity collision
SMD	Single molecule detection
SCL	Super continuum laser
SPR	Surface plasmon resonance
T_n	Excited triplet state
UME	Ultra-microelectrode

Symbols

A	Absorbance
K_{ads}	Adsorption constant
E_{tot}	Applied external potential
$\sigma\ (\lambda)$	Absorption cross-section
a	Area of the electrode surface
$G(\tau)$	Autocorrelation function
$<N>$	Average number of molecules in the observation volume
k_B	Boltzmann's constant
c_0*	Bulk concentration
r_{ME}	Center of microdisk
τ_T	Dark state lifetime
ρ	Density
D	Diffusion coefficient
D_τ	Diffusion time
x	Distance between the feeder electrodes
z_f	Distance between the glass surface and the objective
$d_{ME\text{-}CV}$	Distance between the center of the confocal volume and the electrode surface
k_{El}	Electrochemical reaction rate constant
G	Electrolyte conductivity
F	Emission intensity
V_{eff}	Effective observation volume
F_E	Integrated intensity at the electrode surface
F_A	Faraday constant
F_E(B)	Fluorescence background intensity at the electrode surface
F_g(B)	Fluorescence background intensity at the glass surface
$\delta F(t)$	Fluorescence fluctuations at a certain time
ω_0	Full width at half maximum x,y axis
$\delta F(t+\tau)$	Fluorescence fluctuations at lag time
F_g	Fluorescence intensity at the electrode surface
F_g	Fluorescence intensity at the glass surface

τ_F	Fluorescence lifetime
$Ji(x)$	Flux of species
h_{cv}	Hight of the cylinder
h	Planck's constant
k_{IC}	Internal conversion rate constant
k_{ISC}	Intersystem crossing rate constant
k_Q	Quenching rate constant
τ	Lag time
L	Length of the bipolar electrode
m	Mass of the particle
M	Molar mass
k_{nr}	Non-radiative relaxation rate constant
n	Number of electrons
$N(t)$	Number of fluorophores in the detection volume
dN_{ad}/dt	number of particles being adsorbed
dN_{des}/dt	Number of particles being desorbed from the surface
dN_{ox}/dt	Number of particles destroyed by an oxidation process
dN_{in}/dt	Number of particles entering the observation volume in a time interval dt
$<N>$	Number of particles inside the confocal volume
dN_{out}/dt	Number of particles leaving the observation volume by diffusion
N_A	Numerical aperture of the microscope lens
$S(r)$	Optical transfer function of the objective pinhole
K	Overall detection efficiency
n^*	Quantum number of the discrete energy level
Φ_N	Quantum yields
k_r	Radiative relaxation rate constant
r_{cv}	radius of the cylinder
r_0	Radius of the electrode
r	Radius of the particle
R	Refractive index
R_{el}	Resistivity of the electrode
$I_{ex}(r)$	spatial distribution of the excitation energy

i_{ss}	Steady state current
T	Temperature
$(\pi Dt)^{1/2}$	Thickness of the diffusion layer
t	Time
k_{VR}	Vibrational relaxation rate constant
λ	Wavelength

1 Introduction

In the past decades, nanoparticles (NPs) become increasing important in various branches of modern technologies, such as biological imaging applications, therapeutics, photovoltaic devices and catalysis[1–8] because of their extraordinary physical and chemical properties. Several studies have shown that the physical (e.g., light emission and absorption) and chemical (e.g., catalytic reaction) properties of a NPs don't only depend on its chemical composition but also on its size and shape[9]. So, there is a need for better characterization of (NPs) in the sense of quality control during production and understanding their properties with respect to a certain application. Moreover, understanding the behaviour of their interaction with various surfaces is of the fundamental importance to understand and to predict their potential impact.

So far, NPs produced in bulk reactions are rarely uniform in size, shape and reactivity[10,11,12]. It was not possible to distinguish between subpopulations of NPs and to separate electrochemically inactive NPs from active ones with conventional electrochemical methods. Here, information about single particles is required. In order to obtain such information, the stochastic transient Faradaic responses of single (NPs) on the surface of (ME) must be studied. One of the most important phenomena is charge transfer reactions of NPs because of their central role in catalysis and energy conversion. As a NPs collide with the electrode (Fig.1), they are oxidized either by one collision (Fig.1a), or multiple collision (Fig.1b), forming a current spike. The frequency of spikes are correlated with the concentration of NPs and the charges from one event inform about the size and the size distribution.

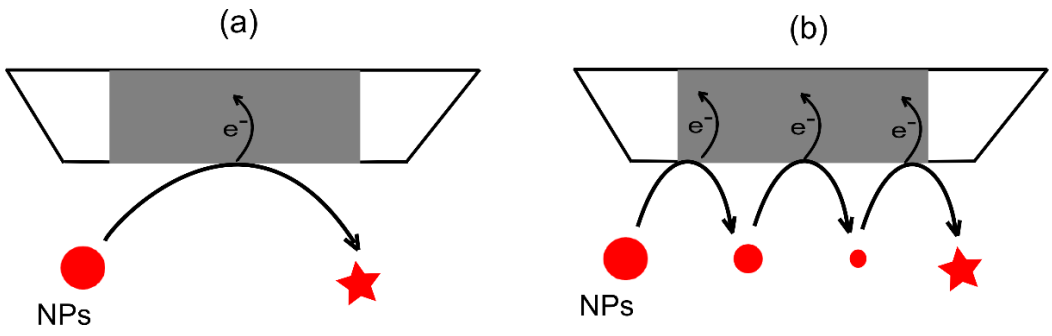

Figure 1: Dissolution of the NPs at the electrode surface in, (a) one collision, (a) sequence of collisions.

The observation of charge transfer reactions in single particle experiments provides a measured electronic response that can be related to the reaction of an individual NP thus providing a large extent of additional information about mechanistic details of NP electrochemistry.

Bard's group pioneered a single nanoparticle collision (SNC) approach which separates the individual NPs temporally by resolving their arrival times at the electrode[13,14]. Electrochemical processes of single NPs have been studied extensively. The direct single NP collision experiments with direct NP transformation produces very low Faradaic current. For the observation of single NP collision events, where the transmitted charge is caused exclusively by NP transformation, electrochemical methods suffer from the limited signal-to-noise-ratio (SNR). The charge released by complete oxidation or reduction of a single NP must produce a current spike that is large enough to be detected against the noise caused by the thermal movement of ions in the electrical double layer[15,16]. So, several approaches were introduced to amplify the current such, electrocatalytic amplification[13,17–19] and blocking effect[20–24]. However, the smallest NPs that used for direct conversion in single particle collision experiments was 10 nm[25]. More often experiments are restricted to NP sizes of 30 nm and larger[26–29]. Beside the current amplification, the single particle collision was enhanced by minimize the background current as small as possible. Reducing the electrochemical cell was one of the assumptions to achieve low background[25,30].

Coupling the optical spectroscopy with electrochemistry is other method that have very high sensitivity allowing one to detect single redox events. The changeable in the optical property of a redox particle upon oxidation and reduction at the electrode surface is more detectable than the charge transfer. Optical monitoring of the analyte provides a convenient and sensitive way to measure the electrochemical signal of the analyte. Single NP electrochemistry has been combined with several optical methods for gaining an experimental correlation between an electrochemically registered event and the localization of the NP at or near the electrode surface. So far, surface plasmon resonance[31], dark field scattering[32,33] or Raman scattering[34,35] were utilized for this purpose.

The coupling of electron transfer events to fluorescence presents new avenues for the study of particle collision with high throughput, sensitivity, and spatial resolution[36,37] The switchable of the fluorescence property between on and off upon potential modulation for some molecules was exploited to monitor the charge-transfer events[38–40]. Fluorescence spectroscopy is a good example for different reasons. There are enough optical properties

differences between the reduced and the oxidized form. Also, signal to noise ratio is enhanced by reducing the effective volume of excitation. Furthermore, oxidizing one particle produces more photon than charges. If luminescent particle was used as a redox active, photon output (Fig. 2b) can be observed instead of charge output (Fig. 2a) where the photons are more sensitive than charges[41]. So, techniques based on the fluorescence readout are potentially more sensitive than techniques based on the charge readout.

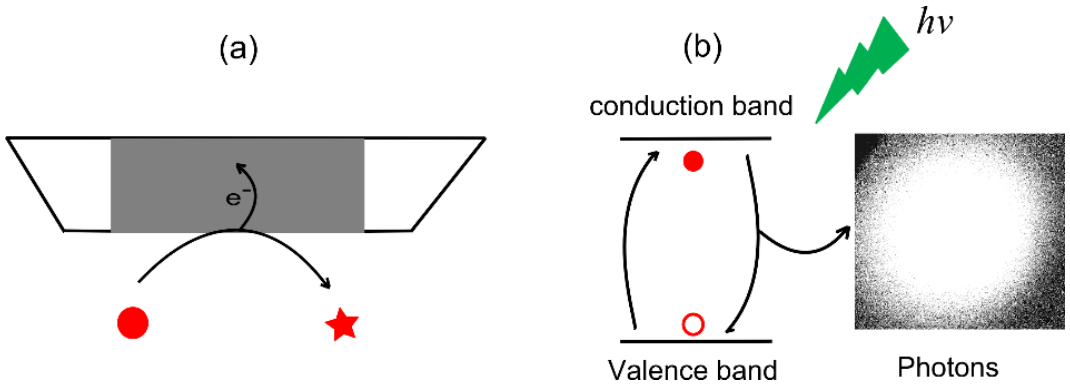

Figure 2: (a) charges and (b) photon output.

In our project, the collision of very small QDs (2-6 nm) and Ag NPs (2 nm) were studied which are considerably smaller than NPs typically used in single particle collision experiments so far. However, it is not clear yet whether this will lead to a complete dissolution of a very small single collision (Fig. 1a) or just like a bigger NPs, require a sequence of collisions for complete oxidative dissolution (Fig. 1b). Because the transferred charge from individual QDs is too low to produce an electronic response that can be separated from the thermal noise, the ultimate sensitivity method in electroanalytical chemistry is required. Furthermore, QDs show much more complex redox properties including reductive injection of electrons to the conduction band, oxidative extraction of electrons from the valence band, and filling and emptying of trap and defect sites[42–48].

The electrochemical reactivity of a single particle on the surface of a micro electrode was observed via single molecule spectroscopy (Similar approaches are also possible for NPs). This method provides information about adsorption and desorption of NPs on the electrode surface, resting times and kinetics of NPs modification or degradation process (Fig. 3). In order to enable a correlation of optically registered events and electrochemical events, the diameter of the (ME) used as working electrode is matched to the size of the optical observation volume,

typically around 1 µm. In this approach, fluorescence correlation spectroscopy (FCS) was used for optical particle detection and characterization. FCS is a very sensitive technique capable of studying single QD dynamics in various environments over a wide range of correlation time using statistical analysis of fluorescence fluctuations emitted from a small defined observation volume. Unlike most fluorescence-based techniques, the collected data is not the fluorescence intensity itself, but the small statistical fluctuations of the fluorescence signal over time. So, the instability of the fluorescence and the low quantum yield of the fluorescent do not represent significant problems. For data evaluation, cross correlation analysis is employed, providing information about adsorption and desorption of NPs on the electrode surface, resting times and dissolution of NPs.

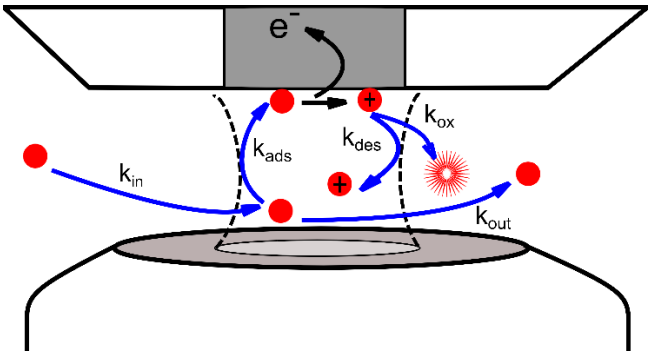

Figure 3: The different kinetics of the NPs during impact to the ME surface.

Studying the interaction of the particles at the electrode surface by fluorescence spectroscopy is restricted to study the redox active fluorophores or special fluorogenic redox reactions. In these methods, the fluorescence property of the target particle itself is changed. To broaden this method for a wide range of particles, the fluorescence spectroscopy was coupled with a bipolar electrochemistry (BPE). In this method, an indirect investigation regarding the electrochemical activity of single particle through the bipolar electrode (BE) was described. One solution compartment contains an oxidizable redox analyte, while the other contains a fluorogenic reporter.

The coupling was used to explore in detail the relationship between the electrochemical behaviour on one pole of BE and the fluorescence microscopy results on the other pole. The oxidation of the target particle was coupled to the reduction of the reporter molecule. Organic dyes with highe absorption cross section and high fluorescent yield were used to monitor the events on the other pole. Upon the reduction of the fluorescent dye on the cathodic pole, its

fluorescence property changes. Because the changes in the fluorescence intensity on the cathodic pole were triggered by the reaction of the analyte on the anodic pole, a correlation between the fluorescence change on the cathodic pole and the electrochemical process on the anodic pole can be obtained.

In our project, two different dyes were used as a reporter. Resazurin was used as an irreversible dye and tris(bipyridine)ruthenium (II) chloride as a reversible dye. To compare the output fluorescence with the corresponding charge transfer, reference measurements for known electrochemical material are required. Because FcMeOH has a well defined reversible electrochemistry and was studied abundantly, it was used as a reference. The experiments enable us to measure the photon intensity that is generated by the reduction of the fluorogenic molecule on a cathodic pole. This intensity gives us an impression on the electrochemical reactivity at constant potential on the anodic pole.

2 Theory and background

2.1 Fluorescence phenomena

2.1.1 The fundamentals of fluorescence

Fluorescence is a familiar phenomenon first described in the middle of the nineteenth century[49]. It is one form of photoluminescence and refers to the relaxation mechanism for molecules from an excited singlet state (S_n) to the singlet ground state (S_0) after the photoexcitation of a molecule. In addition to fluorescence, different concurring mechanisms occur after a molecule is excited such as vibrational relaxation (VR), internal conversion (IC) and intersystem crossing (ISC), like illustrated by the Jablonski diagram (Fig. 4). For a more detailed view, the vibrational levels in between the electronic states, the rotational states in between the vibrational states and the energy difference between the states in each molecule have to be considered. VR occurs if the excited molecules relax from one of the vibrational states in an electronic state to less energetic vibrational state by releasing some energy. IC involves the transition of the molecule from one electronic state to a lower electronic state due to the coupling between the electronic states followed by the relaxation of the molecules from a higher excited vibrational level of the target electronic state to the vibrational ground level. ISC is a process that is responsible for altering the spin state of the molecule when it moves from a singlet state S_n to an excited triplet state (T_n).

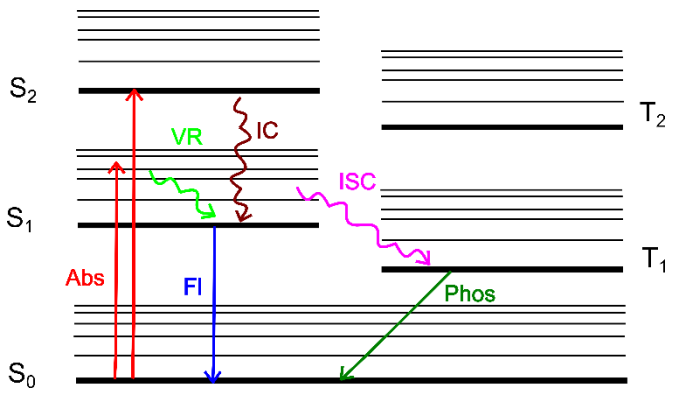

Figure 4: Jablonski diagram with absorption (Abs), vibrational relaxation (VR), internal conversion (IC) and intersystem crossing (ISC), Fluorescence (Fl), phosphorescence (phos).

If S_n is thermally equilibrated, the molecule may relax from the lowest vibrational state in S_n to S_0 accompanied by a radiative process called fluorescence. It is the fastest radiative relaxation mechanism and occurs with a rate constant of 10^8 s^{-1}. Alternatively, the electron can change the spin state by ISC, the system becomes a triplet state and subsequently phosphorescence happens[50]. Because the T_1 state is always of lower energy than the corresponding S_1 state, phosphorescence has as higher emission wavelength than fluorescence. As the relaxation from the T_1 state to the S_0 state requires another spin flip, the T_1 state is long-lived compared to the corresponding S_1 state, thus phosphorescence has also longer lifetime than fluorescence. When the molecule relaxes to S_0 and emits a photon, some energy is dissipated through the vibrational and rotational states and also by solvent reorganization. So, the emission wavelength is longer than absorption wavelength. The difference between absorption and emission wavelength is called the Stokes shift. The broadness of the absorption and emission bands depends on the distribution of the states in the molecules. Due to the solvent-dye interaction, the molecules try to reorganize and consequently the number of the rotational and vibrational states becomes larger and more distributed. Therefore, the absorption and emission bands of the molecule will be broadened in solution.

Molecules that display fluorescence are called fluorophores or fluorescent molecules. The fluorophore is used in different applications due to the intensity of the fluorescence radiation compared to the background. The intensity depends on the extinction coefficient (ε) and quantum yield (Φ_F). The extinction coefficient describes the capability of the fluorophore to absorb light of a particular wavelength. The quantum yield is the ratio of emitted to absorbed photons. In the last decades, several techniques were developed based on the fluorescence phenomena in the field of life-science like living cell identification[51], small molecules probes[52], single molecule identification[53] and imaging of electrochemical events[54,55].

2.1.2 Fluorescence lifetime and quantum yields

Fluorescence lifetime (τ_F) is the average residence time of the fluorophore in S_1 before returning to S_0. It ranges from picoseconds to some nanoseconds. Indeed, not only one fluorophore is available in the excited state after excitation, but there are several fluorophores that move back gradually to S_0. τ_F is defined as the time it takes until the fluorescence signal decays to 1/e of its original value. The relaxation from the S_1 to S_0 takes place through different

mechanisms. They can be divided into two big groups: non-radiative relaxation (k_{nr}) and radiative relaxation (k_r). The rate constant of the non-radiative decay is composed of different parallel processes such as: internal conversion (k_{IC}) and intersystem crossing (k_{ISC}). The lifetime depends on both processes as seen in Eq. (1).

$$\tau_F = \frac{1}{k_r + k_{nr}} = \frac{1}{k_r + k_{IC} + k_{ISC}} \quad (1)$$

Lifetime is more specific than absorption and emission to recognize the dye, because the emission and absorption bands for different dyes often overlap. The lifetime of a fluorophore bears a valuable information not only about the substance but also about the local environment. The influence of the external effects such as quenching, and energy transfer can be seen in lifetime measurements.

The quantum yields (Φ_F), is an important criterium that is used for choosing dyes. Fluorophores that possess higher Φ are more favoured in applications. As long as the k_{nr} is small, Φ_F become close to the unity. At a given absorption wavelength, Φ_F can be calculated by recognizing the number of emitted photons of the unknown dye compared to the reference dye as seen in Eq. (2), where R is the refractive index, F is the emission intensity and A is the absorption.

$$\Phi_F = (\Phi_F)_{ref} \frac{R^2}{R_{ref}^2} \cdot \frac{F}{A} \cdot \frac{A_{ref}}{F_{ref}} \quad (2)$$

2.1.3 Overview of luminescent NPs

Luminescence is a general terminology that is related to the spontaneous emission of light by any substance. Because fluorescence is restricted to the relaxation of molecules, it not possible to use the fluorescence terminology in case of particles. So, luminescence is used to express the spontaneous emission of light by particles. Luminescent nanoparticles (LNPs) are particles with diameters between 1 and 20 nm and composed of several to hundreds atoms[56]. They have unique optical properties compared to organic fluorophores such as high photostability, high quantum yield, broad excitation profiles and size-tuneable luminescence spectra with narrow emission bands. These advantages qualify LNPs to be a promising alternative to molecular dyes in different fields, such as biological imaging applications, therapeutics, photovoltaic

devices and catalysis[1–8]. Decreasing the size of the particles to the nanoscale changes the optical properties compared to their bulk structures of the same material. For example, metallic NPs are non-fluorescent at sizes higher than 20 nm. LNPs have relatively complicated structures because they are composed of different layers (Fig. 5)[57]:

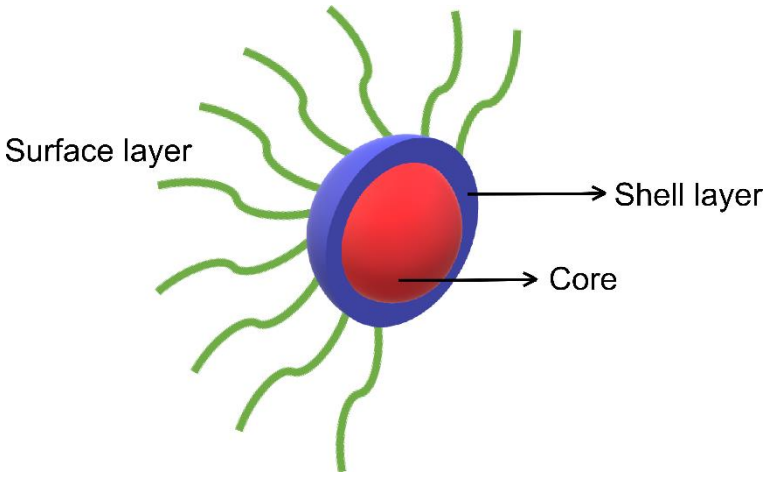

Figure 5: Luminescent NPs structure consist of core layer, shell layer and surface layer.

(*i*) At core, which is usually the NPs itself and with a structure similar to the bulk structure of the same material.

(*ii*) The shell layer is very important to protect the core from the external influences. The high surface to volume ratio for NPs makes it more prone to external influences (quenchers).

(*iii*) The surface layer promotes the solubility and prevents aggregation. In some applications like biomedical research, it is necessary to render the NPs hydrophilic ones by surface modification with various bifunctional surface ligands or caps, while most core-shell NPs are hydrophobic[58]. LNPs can be divided into different groups depending on size and chemical properties: carbon based NPs[59], metal NPs[60,61], ceramics NPs[62], semiconductor NPs[12,63], lipid-based NPs[64] and polymeric NPs[65].

Semiconductor quantum dots: QDs are semiconductors NPs that are confined in three dimensions with a diameter of 2–10 nm[66]. They possess distinct optical and electrical properties compared to the bulk materials when the exciton dimensions decrease to dimensions

smaller than the exciton Bohr radius. This is a physical constant that expresses the distance between electron and hole in an electron-hole pair[67]. When atoms are arranged in solid state, the orbital energies are splitted when molecular orbitals transform to the cluster orbitals and therefore dense bands are formed (Fig. 6). When the bulk materials are confined in at least one dimension, the band gap, band edge positions and density of state is affected. Thus, the random motion of the electrons inside the energy level becomes restricted to specific, discrete energy levels.

The size dependence of the band gap for QDs is the most important consequence of the quantum confinement. So, the emission wavelength can be tuned by changing the size of the particles. The influence of the confinement on the band gap is illustrated in Fig. 6. In the metals, the conduction and valence bands overlap, and the electrons move through the bands freely. In contrast to that, in case of semiconductors the conduction and the valence bands are separated by a band gap. QDs with smaller sizes have larger band gaps. In order to minimize the required wavelength for the excitation, the band gap must be large. Consequently, smaller QDs absorb higher energy (blue wavelength) than larger QDs (red wavelength).

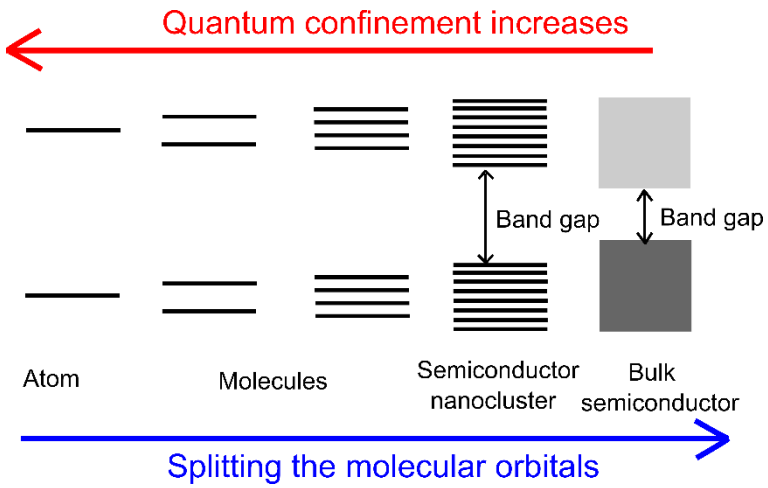

Figure 6: Confinement effect on the band gap of QDs.

QDs are mostly prepared with core-shell structure. The shell is mainly used to enhance the Φ_F of the QDs, stabilize the QDs and concentrating the charge carriers in the nanocrystal core[68]. In the absence of the shell, the wavefunction of the coupled electron-hole-pair (exciton) will extend to the nanocrystal surface where defects and quenchers are localized. So, the shell

provides an efficient confinement of electron and hole wavefunctions inside the nanocrystal. Core materials always are different than shell materials. A shell thickness in the nm scale usually large enough to saturate the defects on the surface and to supress tunnelling of electrons or holes to the surface. The type of shell material has to be adapted to the core material. To obtain QDs with less defect states, the lattice of the shell has to be matched the lattice of the core as possible. For, example CdS has less mismatch to CdSe compared to ZnS and ZnSe. So, CdS is appropriate and more popular when CdSe-based core-shell QDs are prepared [69]. In addition to that the band gap of the shell with respect to the core has to be considered. Because the band gap of CdSe is smaller than CdS, the electron and the hole are confined inside the core and therefore the quantum yields of the QDs increases. In General, for effectively confining the exciton in the core, energy levels for electrons in the shell should be lower for the VB and higher for CB. Consequently, the electron and the hole in the core are re-combined together instead of re-filled the hole with electron from the shell. Sometimes, multiple shells are required if the lattice of the shell does not match the lattice of the core well or to enhance the band alignment. For this purpose, another shell with an intermediate lattice parameter is inserted into the core-shell system.

The atoms in a semiconductor are materials from either group IV of the periodic table, or for binary QDs of combinations from group II and group VI called (II-VI semiconductors), or from a combination of group III and group V called (III-V semiconductors). Different types of QDs were reported including CdSe/CdS[70,71], CdSe/ZnS[11,46,72], CdS/ZnS[73], CdSe/CdTe[74]. Actually, these are the most interesting in research where a large number of papers deals with these QDs. The shell is selected from semiconductors that have the same crystal structure, but higher band gaps than the core. This is important not only optically but also electrochemically. For example, CdS and ZnS shells are very important to generate a higher threshold to photooxidative degradation and surface defect formation for CdSe core QDs because S^{2-} has a much lower oxidation potential than Se^{2-}[75].

Metallic nanoparticles (MNPs): Compared to bulk metal, MNPs possess unique optical, mechanical, chemical and electrical properties such as prominence of luminescence, higher surface to volume ratio and lower oxidation and reduction potentials. In a bulk metal (Fig. 7a), the energy levels of the electrons are continuous because the conduction and valence bands overlap. So, the electrons move through the bands freely. When the size of the metal approaches the Fermi wavelength of electrons[76], the free-conducting electrons in the metal are confined to discrete energy levels (Fig. 7a). Because the electronic wave functions of the

conduction electrons in the metal are delocalized over the entire particle, the movements mechanism of the electrons inside the extremely small particles can be understood on the basis of the fundamental model of electrons confined to a box[77] (Fig. 7b). It is described by the motion of the electron between two walls in one dimension. The potential energy inside the box vanishes and outside tends to infinity. The particle is restricted to move only inside the box but cannot move outside the walls of the box. This is because the particle gains limited energy which is not enough to overcome the potential energy barriers at either end of the box. The behaviour of the particle inside the box is described by Schrödinger equation. This model gives the wavefunction for the particle by Eq. (3), and the energy by Eq. (4). where n^* is the quantum number of the discrete energy level, L is the length of the box, h is Planck's constant and m is the mass of the particle.

$$\psi_{\mathrm{n}} = \sqrt{\frac{2}{L}} \sin\left(\frac{n^*\pi x}{L}\right) \tag{3}$$

$$E_{\mathrm{n}} = \frac{n^2 h^2}{8mL^2} \tag{4}$$

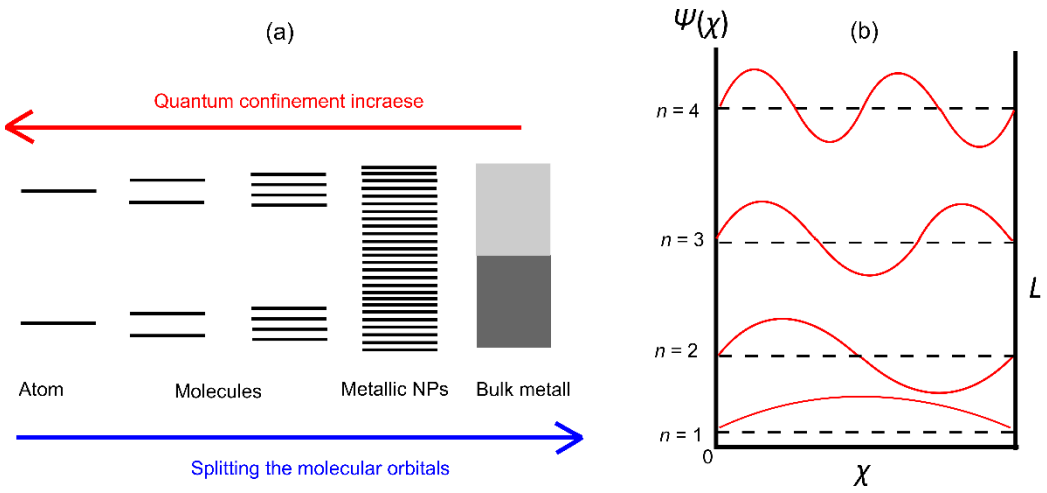

Figure 7: (a) Quantum confinement in a metal, (b) wave function for the particle in a box model.

When the states of MNPs are populated, the freedom of the electrons becomes restricted. For example, if the states are filled with electrons and one electron from the lower state has to go into the next state of higher energy, a gap is produced between the highest occupied and the lowest unoccupied states[78]. Therefore, the motion of the electrons becomes discontinuous. In

bulk metals, the electrons move freely and cause small variations in the density of the electrons. These oscillations in the volume of the metal are called bulk plasmons. At nano-scale size of NPs, such collective oscillation leads to plasmon polaritons due to the strong confinement where negative charges are accumulated in one side and positive charge in the opposite (Fig. 8)[79]. When the frequency of the illumination light matches the frequency of these plasmons, the electromagnetic field in the particles is enhanced and consequently these particles become optically active[80]. High electromagnetic field forces the conduction electrons to move toward the NP surface causing surface plasmon resonance (SPR). The surface plasmon resonance is not connected directly to quantum confinement. However, it is affected by it. The intensity of SPR depends on different factors like the electron density inside the NPs, NP size and shape, and the dielectric constant of the surrounding medium. The influence of the size on the plasmon band width was studied firstly by Kreibig in 1985[45]. The experiments showed that decreasing the size of MNPs shifts the plasmonic resonance to blue wavelength[81]. The optical properties of metal nanoparticles are mainly dependent on the collective oscillation of conduction electrons. So, noble metals, especially Ag and Au, are more popular in case of luminescence MNPs synthesis where they have high collective oscillations of conduction band electrons[82]. Nowadays, metallic NPs are more applicable especially in bioassay or medical applications than QDs because of their lower toxicity[76,83].

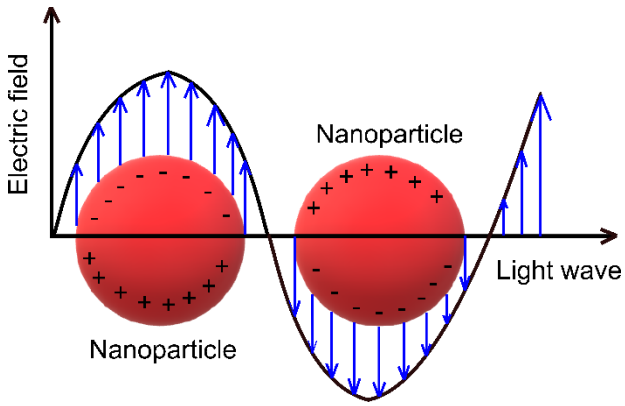

Figure 8: illustration the localized surface plasmon resonance (LSPR) on nanoparticle outer surface.

2.1.4 Blinking and quenching phenomena

Quenching is a term used to express the dropping in the luminescence intensity by interaction with a quencher. It can take place either dynamically or statically. The main difference between them is represented by the mechanism of complex formation with a quencher (Fig. 9), where $[LNP]^*$ is the excited particle and Q is the quencher.

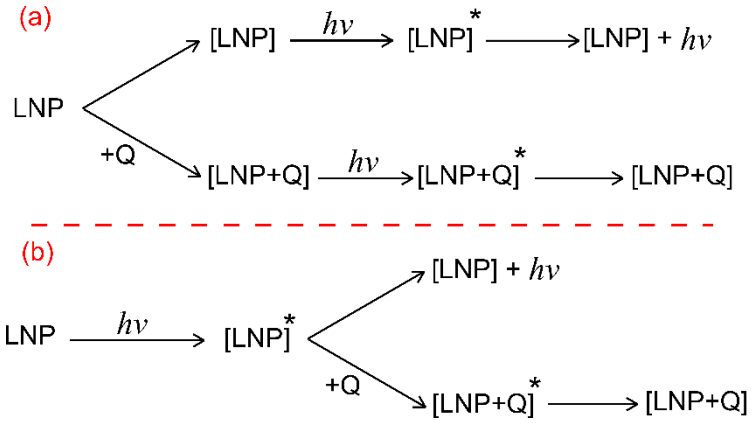

Figure 9: Schematic explanation of (a) static and (b) dynamic quenching.

In static quenching, the complex between the particle and the quencher is formed in the ground state. Two types of particles are available in QDs: complexed electrons and un-complexed ones. The particle is either excited alone or together with the quencher as a complex. Both particles absorb the same quanta of energy and attain the excited state without any changes in absorption spectra. Nevertheless, the luminescence intensity depends on the equilibrium between the complexed and un-complexed particles. So, the quantum yield is decreased where the luminescence is produced only from the relaxation of un-complexed particles. In contrast, dynamic quenching occurs after the excitation where the complexation occurs between the quencher and the excited particles. Thus, two types of excited particles exist in the excited state (complexed and un-complexed). Unlike static quenching, the equilibrium between the complexation and un-complexation occur after the excitation. So, the lifetime is reduced, and the quantum yield is less affected.

Similar to organic dyes, the lifetime of QDs is related to the radiative and non-radiative decay rate (Eq. 1). In addition to radiative and non-radiative rate (k_r, k_{nr}), the rate of quenching $k_q[Q]$ has to be considered for the emission lifetime τ_E (Eq. 5).

$$\tau_{\mathrm{F}} = \frac{1}{k_{\mathrm{r}} + k_{\mathrm{nr}} + k_{\mathrm{q}}[Q]} \tag{5}$$

Actually, photoluminescence quenching can be related to the different reasons like energy transfer, charge transfer reactions, photochemistry or formation of complexes in the valence band. However, charge transfer quenching is very important to consider, because it is used to probe the photoactivity of materials and is related also to our research. To study the lifetime of QDs in the presence of electrochemical effects, the rate of electrochemical reactions should be considered. In principle, the electrode can work as quencher. τ_{E} can be calculated according to Eq. (6), where k_{El} is the rate of an electrochemical process.

$$\tau = \frac{1}{k_{\mathrm{r}} + k_{\mathrm{nr}} + k_{\mathrm{El}}} \tag{6}$$

The electrochemical interaction between NP and electrode depends on the location of the Fermi potential of the electrode with respect to the energy of valence and conduction bands[84] Fig. (10).

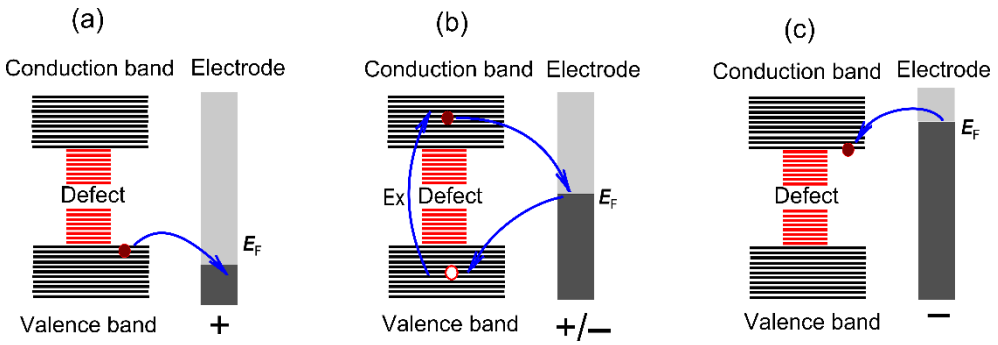

Figure 10: Dependence of photoelectrochemical effects of quantum dots on an electrode surface. (a) Oxidation potential, (b) potential in between the oxidation and reduction potential, (c) reduction potential.

At oxidation potential (Fig. 10a), the Fermi potential of the electrode is closer to the valence band and static quenching is more likely than dynamic quenching because the charge transfer could happen before absorption of the photon. On the other hand, at reduction potential, the Fermi potential of the electrode is raised up close to the conduction band[85] (Fig. 10c). In that case, static quenching is also more probable where the complexation occurs between the excited electron in the conduction band and the Fermi level of the electrode. If the Fermi

potential of the electrode is in between the valence and the conduction bands (Fig. 10b), no electron transfer between QDs and the electrode occurs because there are no available free electrons in the conduction band or holes in the valence band. In this case, no quenching occurs until the electrons inside QDs are excited with light. In that case, dynamic quenching occurs directly or indirectly through activation or deactivation at the trapping state[43,85]. Studying of quenching phenomenon is a good way to monitor the charge transfer between the electrode and fluorescent particles.

Blinking is another phenomenon accompanying QDs luminescence effects and their applicability. Unlike quenching, blinking is a random luminescence intermittency between bright and dark states. Earlier, blinking in QDs was not a substantial problem because QDs were measured in ensemble measurements[86]. Blinking started to be considered after using QDs in single entity measurements. The blinking effect can be attributed to charging the particles with high number of external charge or to the influence of the defect states.

In the ideal case, the electron recombines with the hole in the valence band radiatively after the electron is excited to the excited state (Fig. 11a). If there is an additional charge, it will promote the non-radiative recombination (Auger mechanism) between the external charges and the holes in the valence band (Fig. 11b). Thereby, both emission intensity and lifetime decrease. So, the emission swings between on (non-charged) and off (charged), states. For this reason, charge control is very important to avoid this type of blinking[87].

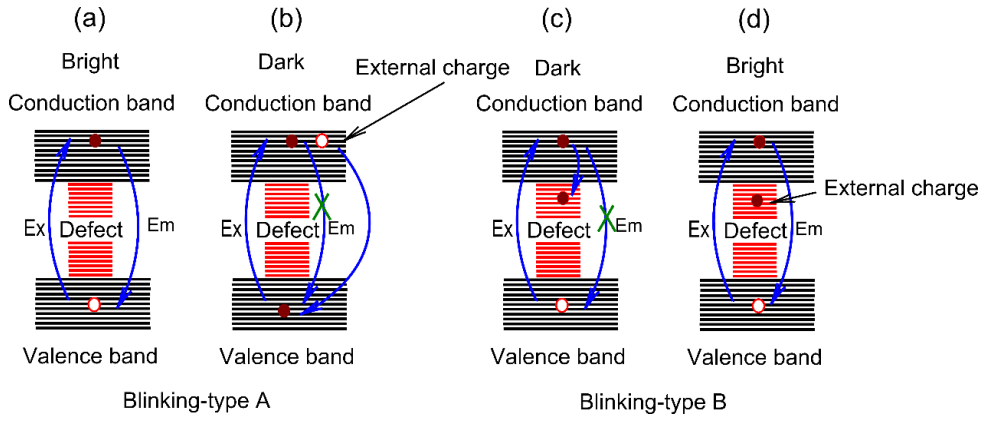

Figure 11: Types of blinking phenomena in semiconductor NPs. (a) Radiative recombination of blinking-types A, (b) non-radiative recombination of blinking-types A, (c) non-radiative recombination of blinking-types B, (d) radiative recombination of blinking-types B.

Blinking is also the consequence of charge fluctuations in the excited state due to the activation and deactivation of short-lived surface traps (Fig. 11c,d). In this case, the excited electrons are trapped before relaxing to the valence band (Fig. 11c). This deviation will change the lifetime and the luminescence intensity. The return pathway of the electron becomes longer and depends largely on the density of the trapping states. Because the blinking effect is non-familiar in single entity detection and QDs in dark state often undergo degradation, a lot of efforts were spent to suppress it. Fomenko et al.[88] illustrated the possibility to vanish the blinking in QDs by altering the chemical environment of the solution. For example, binding of QD to cysteine residues of proteins reduces the blinking effect due to filling of surface defects with the thiol groups[86].

2.2 Single molecule spectroscopy

2.2.1 Single molecule detection (SMD)

Ensemble measurements provide average properties and cannot determine the characteristics of single molecules. The sensitivity of the detection methods down to the single molecule level is an important requirement in applications, where the heterogeneity of molecules should be analyzed. The analysis of single molecule was executed with near-field approaches like atomic force microscopy (AFM) and scanning tunneling microscopy (STM)[89]. AFM was used to probe single particles and manipulate them based on the application of a mechanical force with high spatial resolution. This method is limited to surfaces. In contrast, many optical techniques were used to investigate single molecules without the restriction to surfaces. Examples include ultrasensitive fluorescence detection[90], wide-field microscopy[91], and laser scanning confocal microscopy[92].

Fluorescence can be used to observe single molecules. Dissolved fluorophores are never identical to each other due to the different solvent environment. Therefore, the brightness of individual fluorophores is different. Each molecule in solution at a given time has its own fingerprint even if they have the same size and shape. SMD is used to pass up the synchronisation between the single molecules undergoing a time-dependent process.

Most optical approaches for SMD are based on the fluorescence. Therefore, developments in the SMD field are strongly related to the emergence of fluorescence labelling.

Indeed, fluorescence delivers a high signal against a dark background, so it is a good choice for single molecule imaging. In this context, the first single molecule experiment was performed in 1961 when Rotman could detect individual molecules of the enzyme β-D-galactosidase in a fluorogenic microdroplet substrate[93]. After that Hirschfeld (1976)[94] detected large molecules labelled with multiple chromophores by using the total internal reflection technique which provided an excitation/detection volume of about 24 fL. By 1980s, correlation function measurements were developed to study individual fluorophores in a biology. From that time till 1989, a lot of promising work[53,95] was carried out in this scope but without efficient signal to noise ratio (SNR) to detect the fluorescence light from single molecules. Shera et al.[96] pioneered single molecule fluorescence spectroscopy (SMFS). In 1990, they enhanced the SNR to the single molecule level by reduction of the laser-illuminated sample region to a diffraction-limited volume. They designed the confocal setup perfectly to eliminate the noise signal and they reported the first result in that year which commenced the golden decade for SMD.

SMFS is a technique that is used to probe the fluorescent entity by combining the femtoliter-sized observation volume of a confocal microscope with low concentrations of analytes. This is reducing the background signal to a minimum and permits only a single entity inside the confocal volume (Fig. 12). The observation volume of a confocal setup is represented by an ellipsoid with Gaussian intensity distribution and short axes in *x* and *y* direction and long axis in *z* direction.

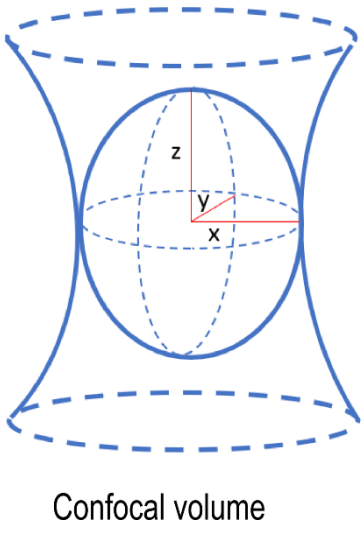

Fig 12: Ellipsoidal confocal volume.

The background signal is mainly created by Rayleigh and Raman scattering. Decreasing Raman scattering is accomplished by decreasing the detection volume, where a clear effect of the solution volume on the Raman scattering was observed[97]. On the other hand, Rayleigh scattering can be avoided by the quality of the optical components especially by a filter system. Rigler et al.[98] demonstrated a confocal set-up for determining the effective sample dimensions. This idea was developed by using a strongly focused laser beam, a small pinhole size and a sensitive avalanche photodiode detector. The responsibility of the pinhole in the focal plane is to reject all the light coming from outside the confocal volume. Single entity experiments are usually designed so that no more than one entity resides inside the confocal volume. In 1 L of 10^{-9} M solution, there are 10^{15} entities. Statistically, if the volume probed by the laser is adjusted to 1 μm^3 inside a 10^{-9} M solution, the number of fluorescent entities inside the confocal volume will decrease to $10^{15}/(10^{-5})^3 = 1$.

The name SMFS suggests that it is applied only to detect molecules, but the same principles and the same setup can be applied for the detection of single particles. The method was named with regard to molecules because the first experiments were performed for molecules. However, some new phenomena occur with single QDs luminescence spectroscopy compared to SMFS.

2.2.2 Fluorescence correlation spectroscopy (FCS)

A single entity (i.e. a molecule or a nanoparticle) can be detected either free in a solution or immobilized in a matrix. Both of options have limitations to define the real characteristics of single entities. The entity properties after immobilization are substantially different due to dynamic disorder and efficient energy transfer[99]. This means that the properties of the entity may depend on the substrate. For example, there is an influence of the matrix on the blinking behaviour of QDs[100]. The matrix may promote or suppress energy and/or electron transfer. Unlike the method discussed above, FCS can detect single entities diffusing freely in solutions and do not require immobilization of the entities on the matrix. FCS is an ultrasensitive and sophisticated technique using a statistical analysis of the fluorescence fluctuations emitted from a small observation volume of around 1 fL. Therefore, it is called a quasi-single molecule technique[101]. Processes with longer time scales than diffusion of the entities in and out the focal volume cannot be followed.

Principle of FCS: FCS was devised and introduced firstly by Magde et al.[102] but it lacked the sensitivity to the single entity level. It was not widely used until high-numerical-aperture confocal microscopy, correlation electronics and detectors tools were incorporated into FCS system[103]. Prior to that, the confocal volume was relatively large, and a long integration time was required to extract information from several fluorophores. FCS was established as a technique for the investigation of translational and rotational diffusion, active transport and flow, photophysical and photochemical transformations, chemical reactions, and molecular aggregation[104].

Unlike most fluorescence-based techniques, the collected data is not the fluorescence intensity itself, but the small statistical fluctuations of the fluorescence signal over time. When an entity enters the confocal volume at steady state (Fig. 13a), multiple excitation-emission cycles occur for the same entity and bursts of photons are emitted (Fig. 13b). The fluctuation of the fluorescence intensity is proportional to the number of molecules present within the observation volume at any given time. It can be caused by diffusion[105], which changes the number of emitters in the confocal volume and by brightness fluctuations of the fluorescent particles in time. Indeed, fluorescence fluctuations can also occur due to many photophysical processes like, chemical reaction[106], aggregation[107], rotational diffusion[108] and excited state reaction[50,109,110]. The number of cycles depends on the fluorescence lifetime and the residence time inside the confocal volume. The time interval of the bursts inside the confocal volume also depends on the residence time of the entity. Therefore, the fluorescence fluctuations of the fluorophore are time-dependent. At the shortest time scale (μs), FCS experiments are limited by photophysical processes or uncorrelated hardware noise overwhelming a small correlated signal. At long time scale (>100 μs), FCS experiments are limited by the diffusion of the free entities away from the observation volume[50,110].

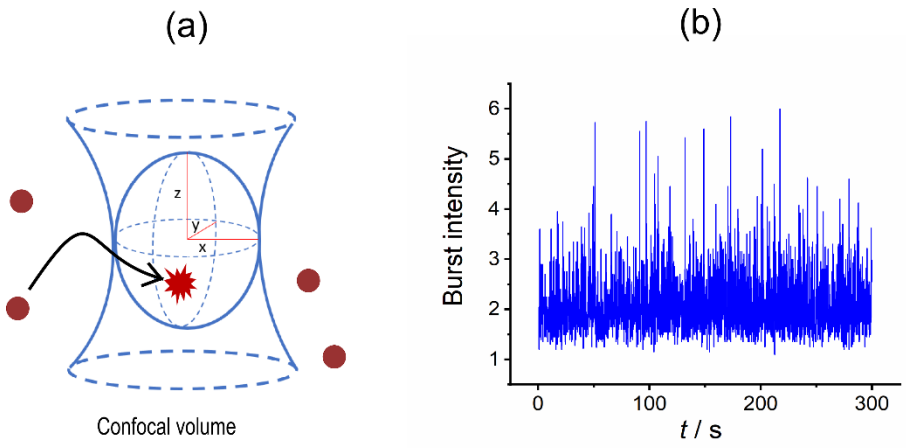

Figure 13: (a) Particles entering and leaving the confocal volume. (b) Time-varying fluorescence signal arising from single fluorophores transiting a confocal volume.

FCS provides a wealth of dynamic information about single entities. When the entities enter and leaves the confocal volume, the fluorescence intensity at a given time $F(t)$ will fluctuate. Fluorescence fluctuations can be quantified via the corresponding deviations $\delta F(t)$ in the fluorescence signal $F(t)$ around its mean value $\langle F(t) \rangle$, where $\delta F(t) = F(t) - \langle F(t) \rangle$. In the same manner if the intensity trace is shifted by a lag time τ: $\delta F(t + \tau) = F(t + \tau) - \langle F(t + \tau) \rangle$. The normalized autocorrelation function $G(\tau)$ expressed by using the fluorescent light intensity fluctuations $\delta F(t)$ is[50,111]:

$$G(\tau) = \frac{< F(t) \cdot F(t + \tau) >}{< F(t) >^2} \qquad (7)$$

In autocorrelation, the collected signal is copied and correlated against itself. In the correlation process the copied signal is moved against the collected signal by the lag time τ. Both signals are overlapped as illustrated in Fig. 14. The overlap integral $\langle F(t)F(t+\tau) \rangle$, marked by the filled areas in Fig. 14, becomes smaller by increasing the lag time τ[112].

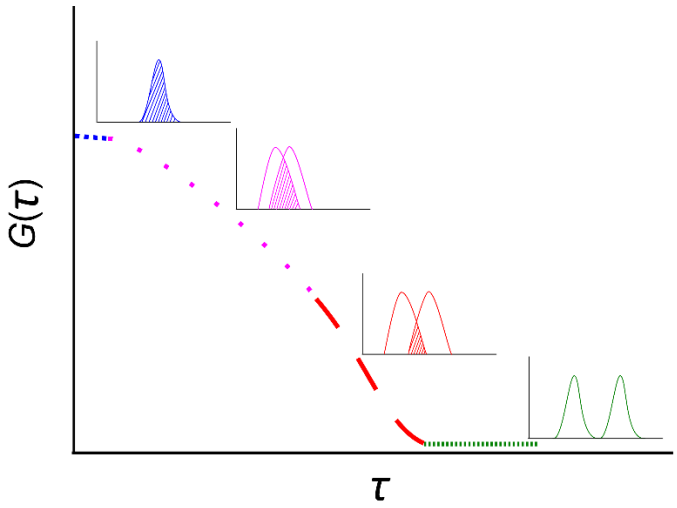

Figure 14: Effect of τ on the intensity of the correlation amplitude.

When fluorescent entities diffuse in a three-dimensional Gaussian volume element, the autocorrelation function is given by Eq.(8).[109,113–115]

$$G_{\mathrm{D}}(\tau) = \frac{1}{< N >} \cdot \left(1 + \frac{4D\tau}{\omega_0^2}\right)^{-1} \cdot \left(1 + \frac{4D\tau}{z_0^2}\right)^{-1/2} \qquad (8)$$

Where τ is the lag time, $<N>$ is the average number of entities in the observation volume and is the reciprocal of $G(\tau \rightarrow 0)$, ω_0 is the full width at half maximum (FWHM) of the intensity distribution in the observation volume in x and y directions, z_0 is the FWHM in z direction and D is the diffusion coefficient. The shape of the resulting correlation curve depends on the behaviour of the entity and geometry of the detection volume. Although this equation gives valuable information about each process related to diffusion, it is not able to explain photophysical phenomena. Additional fluorescence fluctuations grow from populations of triplet or dark states and Eq. (9) is valid for the formation of triplet states in molecules and provides information about the triplet yield and the triplet time, but can be used for the formation of dark states of other entities as well[116].

$$G_T(\tau) = \left[1 + \frac{T}{1-T} \exp\left(-\frac{\tau}{\tau_T}\right)\right] \qquad (9)$$

where T is the yield of non-emitting (dark) states, τ_{T} is the dark state lifetime. Diffusion and photophysics occur simultaneously, but at different time scales. It is not possible to ignore the diffusion effect (slower kinetic process) if the photophysical effect was studied (faster kinetic process). So, both processes must to be merged in one equation (Eq. 10).

$$G(\tau) = G_{\mathrm{D}}(\tau) \cdot G_{\mathrm{T}}(\tau) \tag{10}$$

$G_{\mathrm{D}}(\tau)$ is the autocorrelation function, which is limited by diffusion, while $G_{\mathrm{T}}(\tau)$ is the autocorrelation function attributed to photophysical effect. Merging Eq.(8) and Eq.(9) in Eq. (10) yields Eq.(11).

$$G(\tau) = \frac{1}{< N >} \cdot \left(1 + \frac{4D\tau}{\omega_0^2}\right)^{-1} \cdot \left(1 + \frac{4D\tau}{z_0^2}\right)^{-1/2} \cdot \left[1 + \frac{T}{1-T} \exp\left(-\frac{\tau}{\tau_{\mathrm{T}}}\right)\right] \tag{11}$$

By analyzing the fluctuating signal $\delta F(t)$ over a time period that is much longer than the time scale of the fluctuations (Fig. 13b), the autocorrelation function G(τ) is obtained (Fig. 15). The reciprocal of the correlation amplitude at zero lag time (τ) equals the number of the entities inside the confocal volume. The diffusion time (D_τ) can directly be estimated from the graphs by reading the width of the correlation function at half its amplitude $G(0)$. Triplet dynamics lead to an additional factor in the correlation function if it is described by simple on-off dynamics. The triplet lifetime (τ_{T}) can also be derived from the half height of the highest plateau which corresponds here to 5 µs. Mostly, the value of the τ_{T} equals 1/100 the value of D_τ. Moreover, the average fraction of molecules in the effective volume that are in the triplet state can be calculated. The amplitude of the second plateau value compared to the first plateau is the fraction of the particles in the dark state.

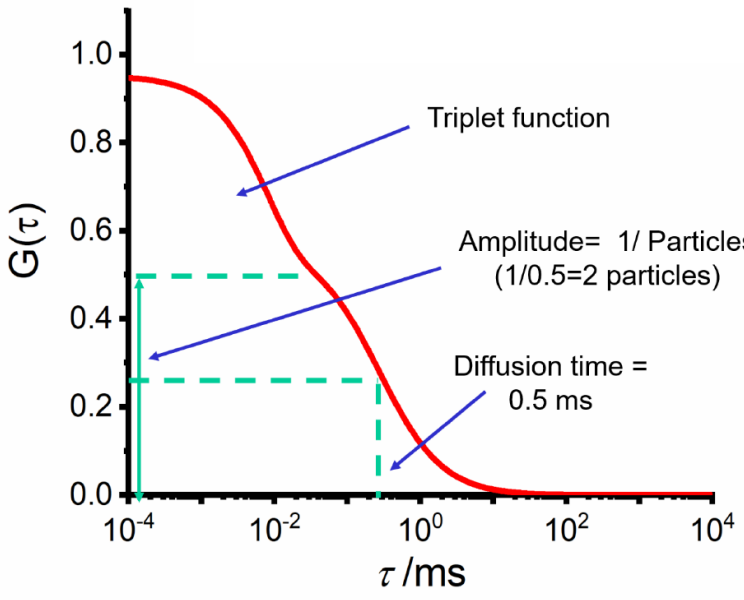

Figure 15: Correlation of statistical fluctuations of the fluorescence signal as function of lag time.

Fluorescence cross correlation spectroscopy (FCCS): In addition to FCS, the fluorescence fluctuations can be analyzed by FCCS. It is a derivative technique of FCS introduced by Eigen and Rigler[78]. It reduces the noise by improving the autocorrelation processing technique that is used in FCS. In the autocorrelation process, the collected signal is copied and correlated against itself. Instead of making a copy signal, FCCS uses two signals from two different detectors and correlates them to each other.

This idea was applied in different ways: The first option is the use of two differentially colored entities inside the confocal volume and excitation with different laser sources[117]. Two signals are separated by a dichroic mirror and recorded separately by two detectors. Secondly, the emitted light can be split by beam splitter into a 50:50 ratio and detected with two statistically independent detectors[50]. The signals of the two different detectors are correlated with each other by moving the signals against each other by a time interval τ. The improvement of the signal by cross correlation is illustrated in Fig. 16. Each detector records discrete events with different distances due to the dead time of the detector. If the signals of one detector are moved by τ, some signals correlate each other, and some signals are missed. The signals that are overlapped produce signals with higher signal to noise ratio.

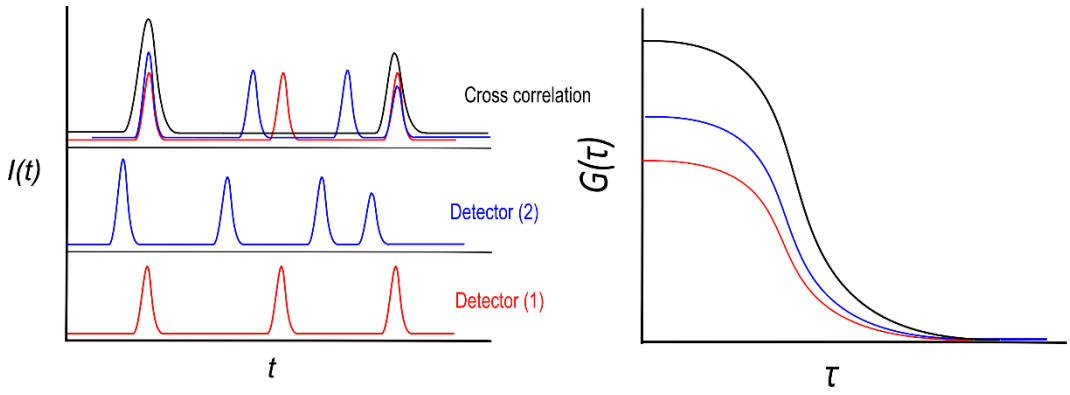

Figure 16: Principle of fluorescence cross correlation spectroscopy.

The cross correlation function $G(\tau)$ is calculated from the normalized overlap integral of the emission intensity $F(t)$ recorded by detector 1 with the corresponding intensity measured by detector 2 plus a lag time τ according to Eq. (12)[50,114,115,118].

$$G(\tau) = \frac{< F_1(t) \cdot F_2(t+\tau) >}{< F_1(t) \cdot F_2(t) >} \qquad (12)$$

2.2.3 Kinetic investigations by FCS

Studying of reaction kinetics was improved by the development of single entity detection. The progress of the reaction is very difficult to follow by ensemble measurements, where intermediates can only be seen under special conditions. On the other hand, the appearance of intermediates is detectable through single entity detection. The time intervals when the emission intensities are high or low can be used to determine the rate constants for the reaction. In the case of the single entity; it is not necessary to consider the starting time for the reaction. The reaction can be studied in a stationary experiment, assuming the substrate concentration is not changing[50].

FCS is a method that provides a wealth of kinetic information of molecular systems compared to other methods that study the kinetics because the entities do not need to be immobilized on a substrate. Furthermore, FCS is applicable for measuring over a wide range of correlation times from picoseconds for photon anti-bunching[119] to tens of seconds for the diffusion of macromolecules[98,120] which is useful for kinetic measurements. Due to the broad range of the correlation time, no overlap between the chemical reaction and diffusion information is expected. Since the internal macromolecule dynamics is considered one of the process that can result in intensity fluctuations, the conformational dynamics of macromolecules can be detected by FCS[113,121,122]. FCS can be used to study protein dynamics or conformational events in the microsecond time scale[122]and is a more suitable technique to study the kinetics compared to other techniques that are related to fluorescence. By fluorescence intensity, it is possible to study the concentration transients until the reaction reaches the equilibrium. In contrast, FCS can measure the reaction kinetics under equilibrium conditions. If a small number of molecules are observed, the intensity will fluctuate as the fluorophore binds to and dissociates from the macromolecules. The rate of intensity fluctuations contains information on the sum of the forward and reverse reaction rates[50].

2.2.4 Setup description

A typical experimental FCS setup (Fig. 17) consists of a modified confocal microscope. The excitation light of a laser excitation source is collected by a dichroic mirror and reflected into

a high numerical aperture oil-immersion objective. Higher numerical aperture and oil refractive index are used to achieve a smaller confocal volume as it is clear from Abbe's law (Eq. 13)

$$d = \frac{\lambda}{2 \cdot R \cdot N_A} \tag{13}$$

where λ is the wavelength of the light, R is the refractive index of the oil and N_A is the numerical aperture of the microscope lens. The emitted light is collected by the same objective and passed through the dichroic mirror to separate the incident and emitted light. After that the emitted light is passed through a clean-up filter. The precise spatial detection is accomplished after passing a pinhole, where most light coming from outside of the confocal volume can be filtered out. The filtered light is devided by a 50 % beam splitter and afterward detected by two detectors for noise reduction. The detectors generate an electrical pulse for each single photon reaching the detector which is further processed by the single photon counting system (TCSPC).

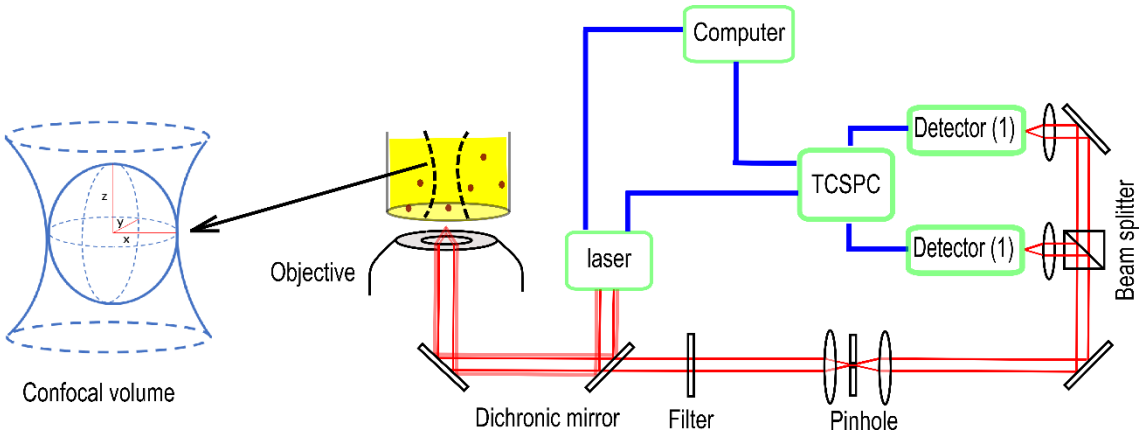

Figure 17: Single molecule fluorescence spectroscopy setup for cross correlation FCS.

Super continuum laser (SCL): This type of laser was integrated to our setup because it is used to produce a wide range of wavelength that can be suitable to excited different types of fluorophores or luminescent particle. SCL emits a very broad spectral bandwidth that is generated by converting laser radiation from one frequency to another through nonlinear optics. In general, transferring light with very high intensity through different media produces tuneable spectra with a large wavelength range. Supercontinuum generation was firstly introduced by

Alfano and Shapiro[123]. They have produced SCL by focusing fs or ps pulses into glass and crystals. Russell[124] has invented a new type of fibre called photonic crystal fibre (PCF). It is used to generate a white light source using relatively simpler lasers and lower intensities compared to other fibres.

The generation of a white light by PCF is illustrated in Fig. 18. A Nd^{3+} glass laser is pumped by a laser diode at a wavelength of 810 nm and a power of 10 mW. The laser emission generated in the ring resonator leaves the resonator via the in/out coupler with longer wavelength (1064 nm) and lower power (1 mW). Inside the resonator, pulses are generated by phase modulation. The modulator is adjusted to approximately 80 MHz repetition rate that needs fitted to the length of the resonator. An average laser power of 1 mW is not enough to pump the non-linear crystal fibre. So, it has to be amplified. The amplification is achieved by pumping a line amplifier with higher power (10 W) from a laser diode at a wavelength of 810 nm. Both light trains (1064 nm seed) and (810 nm pump) cross the Nd^{3+} glass amplifier and need to be separated at the end of the amplification fibre by coupler and clean up filter. The output laser pulse is used to pump the non-linear crystal fibre to produce a broad spectrum between 410 nm – 700 nm. To control the repetition rate of the pulses, a pulse picker is used. It has to be located after the amplification stage. Otherwise the energy of the individual pulses will be increased due to continuous pumping and the increased peak power would crash the crystal fibre. The pulse picker is a tool that is used to control the picking rate of the pulse compared to the original rate. The original rate is always constant, defined by the length of the resonator (typically 80 MHz). Depending on the fraction that is used by a pulse picker, the average power of the output can be defined. For example, 1:1 fraction means that the picking rate of the pulses is 80 MHz (4 W). Finally, the white light (410 nm – 700 nm) is separated by a monochromator to obtain the required wavelength.

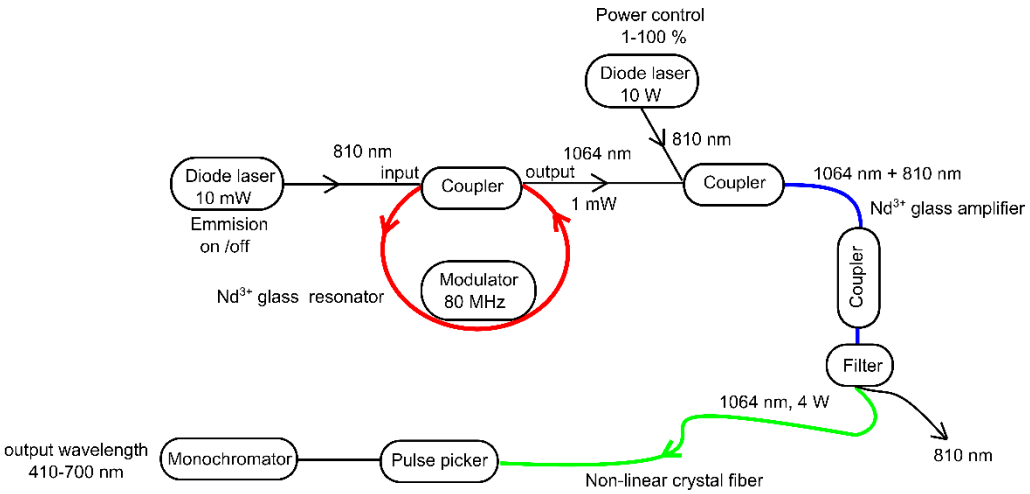

Figure 18: The principle of super continuum laser generation by using photonic crystal fibre.

2.3 Microelectrodes

A microelectrode (ME) is an electrode with dimensions of tens of µm or less, down to sub-micrometer range[125]. It is considered as a promising progress in the field of electroanalytical chemistry over large electrodes due to some features such as, higher signal to noise ratio, lower ohmic drops, low time constant, enhanced rate of mass transport and less sensitive to external convective transport[126]. MEs are used for different purposes: current and potential recording, responding to electrochemical simulation, detection of products of electrochemical reactions, scanning the (ME) with high spatial resolution while detecting compounds, electrochemical reaction in solution of high resistance, measuring important compounds *in vivo*. Several shapes of MEs are used in analytical and molecular electrochemistry such as: linear, spherical, cylindrical, disk and band. Disk geometry MEs are the most commonly used due to some features: the facility of the production, size controllable, easiness of polishing and exhibiting a free diffusion with three dimensions toward the electrode surface[127]. So this type of the electrode satisfies the requirement of FCS measurements.

When a MEs shall be coupled to FCS measurements, the kinetics of the single particle is studied by the statistical correlation of the fluorescence fluctuations emitted from the observation volume. The fluorescence fluctuations are influenced by the mass exchange between the observation volume and the bulk, but also by the mass exchange between the observation volume and the electrode.

To study the reactivity of single particles on electrodes by FCS, the electrode surface should match the diameter of the optical observation volume (1 μm^3). Thus, an electrode with1 µm diameter is very important to minimize bulk contributions. When the electrode potential is switched from a value at which no electrode reaction occurs to the value where the electrode reaction starts, the concentration of the electroactive species at the electrode surface becomes zero and the species diffuse from the bulk solution towards the electrode surface. So mass transport is an essential process in interfacial electrochemical reactions and must be taken into account[128]. In liquids, mass transport is affected by three factors: Diffusion, migration and convection[128]. Mass transport in *x* dimension is expressed by Nernst-Plank equation (Eq. 14) where $J_i(x)$ is the flux of species *i* (mol s^{-1} cm^{-2}) at distance *x* from the surface, D_i is the diffusion coefficient (cm^2/s). The first term on the right-hand side clarifies the concentration gradient by diffusion effect (Fick's first law), the second term represents the potential gradient causing migration and the last one indicates the convection impact.

$$J_{\mathrm{i}}(x) = -D_{\mathrm{i}}\frac{\partial C_{\mathrm{i}}(x)}{\partial x} - \frac{z_{\mathrm{i}}F}{RT}D_{\mathrm{i}}C_{\mathrm{i}}\frac{\partial \emptyset(x)}{\partial x} + C_{\mathrm{i}}v(x) \qquad (14)$$

The contribution of migration and diffusion to the flux of electroactive species from the bulk solution to the electrode surface depends on the proximity to the electrode surface. In bulk solution, the flux of the species occurs mostly by migration where the concentration gradients are not effective. Close to the electrode surface, both migration and diffusion contribute to the mass transport. The advantages of a small electrode were clearly discovered when the mass transport is studied in the vicinity of the electrode. It was found that the mass transport to MEs is more effective compared to macroelectrodes.

Because the diffusion is the main kinetic process causing the fluctuation of the fluorescence (Eq. 8)[50], the mass transport in the solution should be purely under diffusion control. At higher concentration of inert salt or supporting electrolyte, migration of the redox active species can be suppressed to a large extent. To study the dynamic and steady state at the electrode surface, the experimental circumstances should be free from convection effects as well. These can be neglected by preventing stirring and vibrations in the electrochemical cell. For coupling fluorescence experiments one concern is the convection induced by heating the cell by light irradiation. This thermally induced convection sets in after a few seconds that define a window in which idealized conditions prevail. The linear diffusion is apart of the calculation of the diffusion-limited current, i_d and the concentration profile (Eq. 15)[128], where *n* is the number of electron transfer, F_A is Faradays constant, *a* is the area of the electrode

surface, D is the diffusion constant, c_0^* is the bulk concentration, r_0 is the radius of the electrode and $(\pi Dt)^{1/2}$ is the thickness of the diffusion layer.

$$i_{\mathrm{d}}(t) = nF_{\mathrm{A}}aDc_0^*\left[\frac{1}{(\pi Dt)^{\frac{1}{2}}} + \frac{1}{r_0}\right] \tag{15}$$

This expression can be written as

$$i_{\mathrm{d}}(\mathrm{spherical}) = i_{\mathrm{d}}(\mathrm{linear}) + \frac{nF_{\mathrm{A}}aDc_0^*}{r_0} \tag{16}$$

Thus, the diffusion current for the spherical geomery is similar to the linear situation plus a constant term[128]. For a planar electrode,

$$lim_{t\to\infty}\, i_{\mathrm{d}} = 0 \tag{17}$$

but for spherical case, it is

$$lim_{t\to\infty}\, i_{\mathrm{d}} = \frac{nF_{\mathrm{A}}aDc_0^*}{r_0} \tag{18}$$

The progress in ME production involves minimizing the electrode dimension to the scale close to the diffusion layer or even smaller. This results in transforming the planar diffusion field to a hemispherical one. If the dimension of the electrode is minimized to scales smaller than the diffusion layer, the mass transport process becomes dominated by hemispherical diffusion and the current reaches a steady state[129]. In this case, the Faradaic current becomes stationary. Besides the electrode dimension, the duration of measurements is important in case of an expanding diffusion layer. At short time, the diffusion layer is thin compared to r_0 and the electroactive species diffuse to the electrode surface with planar diffusion. The thickness of the diffusion layer increases with time. At longer times, the diffusion layer grows to a size larger than r_0, then the planar diffusion changes to hemispherical diffusion and subsequently the current reaches a steady state (i_{ss}) [Eq. (19)].

$$i_{ss} = 4nFDc_0^*r_0 \tag{19}$$

The smaller the ME, the faster it reaches the steady state, because the formation time of the diffusion layer is directly proportional to r_0^2[128]. Because the diffusion-controlled current depends on the electrode dimension, the obtained current becomes smaller when the size of the electrode decreases. However, the current density $j=i/a$ is increased with decreasing r_0.

The effect of the electrode on the surrounding electrolyte depends on the energy levels of the electrode and the oxidation state of the material.[98]. At negative potential, the energy levels of the electrode raise to position close to empty electronic states of the redox active substance and therefore the electrons flow from the electrode to the substance. In that case, the reduction current is obtained. In contrast to that, the oxidation current is formed at positive potentials when the energy levels drop to the level close to the electronic states occupied with electrons where the electrons transfer from the substance to the electrode. These processes are called Faradaic process where the amount of converted material is governed by Faraday's law (Eq. 20).

$$\frac{dN}{dt} = \frac{i}{nF} \tag{20}$$

In between the oxidation and reduction there is a defined potential where no net current flows. This potential called open circuit potential. The current at an electrode can also be capacitive in nature. In this case, a charge excess at the metal side of the electrode leads to ionic current and finally an excess of negative or positive ions in the electrical double layer without causing a chemical conversion. In the studying of an electrode reaction, both Faradaic and capacitive current always occur together.

The small ohmic drop is one of the important features for ME. This property helps the measurement in very diluted solution. Due to ability of MEs to measure in very limited solution volumes, they are considered as a tool of key importance in single-molecule detection[17] and *in vivo* measurements in biological objects[130].

Electrochemical methods suffer from the limited signal-to-noise-ratio (SNR) during the electrochemical modification of very small amount of redox active species. If the experiments are performed under steady state condition, the noise is mostly attributed to the thermal noise. Minimizing the size of the double layer is very important to decrease the noise caused by the thermal movement of ions in the electrical double layer[15,16]. Thermal noise which is called also Johnson-Nyquist noise is generated as a result of thermal movement of the charge carriers. It is not possible to completely suppress the noise because it is inherent to the permanent charging and discharging process. The thermal noise (S_R) of the electrode can be estimated by the Johnson–Nyquist equation (Eq. 21), where k_B is Boltzmann's constant, T is the absolute temperature and R_{el} is the resistivity of the electrode. $R_{el} = 1/(4\,r\,G)$, where G is the electrolyte conductivity and r is the radius of the elcrtcode.

$$S_R = \frac{4k_BT}{R_{el}} = 16k_BTrG \quad (21)$$

It is clear from Eq. (21) that the thermal noise can be minimized to low values by decreasing the size of the electrode. It was proven that thermal noise is directly proportional to the square root of the electrode area[16]. As the electrode becomes smaller, SNR goes up as illustrated in Eq. (22), where $i_{ss} \propto \sqrt{r}$ and $\delta_{i_{ss}} \propto \sqrt{r}$.

$$\frac{\delta_{i_{ss}}}{i_{ss}} \propto \frac{r}{\sqrt{r}} = \frac{1}{\sqrt{r}} \quad (22)$$

2.4 Single entity collision electrochemistry

2.4.1 The principle of single entity collision

Charge transfer is ubiquitous in all the branches of chemistry. It is created by the interaction between the materials. In electrochemistry, one of the materials is a conducting substrate called electrode which can donate or absorb an unlimited number of electrons. Nowadays these phenomena are well understood with respect to the bulk or large scales[131]. In ensemble measurements of NPs, if the particles flux with Brownian motion diffusion, the particles have different sizes, shapes and are located at different positions. Consequently, the flux rate of the electroactive species towards the electrode surface is not equal and therefore they interact with the electrode surface with different collision rates. The challenge is how to ensure that the current recorded is caused by one particle and not by an average from different particles. In contrast, single entity collision (SEC) is an electrochemical process[20,21,23,24,26–30,132–140] that is used to study electrochemical reactions at the single NP level. It provides key information on the charge associated with random individual events at nanoscale interfaces as a function of time[141]. SEC is a fast technique in the millisecond time regime[142] where a many of particle collision can be recorded in very short time. So, it is a powerful approach that can study very fast electrochemical processes.

SEC experiments are very complex because the background current could interfere with the Faradaic current especially at nanoscale collision. So, most of the efforts in this field were related to the possibility to enhance SNR and confining only one redox active particle at the electrode surface. This was achieved either by decreasing of the dimension as discussed in

section (2.3) or by decreasing the reaction area. For this reason, UMEs are used in SEC experiments. It was studied as a first time by Bard and co-workers by using scanning electrochemical microscopy (SECM)[13]. They have measured the transient current obtained by colliding Pt NPs with a carbon UME. Decreasing the dimension of the electrode not only decreases the noise baseline, but also decreases the landing frequency of the particles at the electrode surface which helps in the spatial resolution improvement. Zhang et al.[30] have decreased the electrode to a dimension close to that of the NP of interest. This approach provides very small effective area that decreases the frequency of collision.

Unwin introduced the scanning electrochemical cell microscope (SECCM)[25,132,143,144] as alternative approach to reduce the background signal. His co-workers could reduce the background current level by isolation of interesting particles from the surrounding in a meniscus and by reducing the reaction area. This approach also is distinct from all processes that used ME by affording the opportunity to use electrode materials that cannot be fabricated as ME. Different approaches were used to investigate dynamic charge transfer during single collision processes at electrode surfaces such as NPs collision via electrocatalytic amplification[116,121,124,125], single NP collision experiments with direct NP transformation[25–27,30,54,145,146] and blocking effect[20–24].

2.4.2 Detection by redox cycling

Amplifying the current is a good option to monitor the electrochemical responses of single entities. Bard and co-workers pioneered the task of the current amplification by redox cycling[17]. The molecule is oxidized and reduced several times between an UME tip and a conductive substrate (Fig. 19).

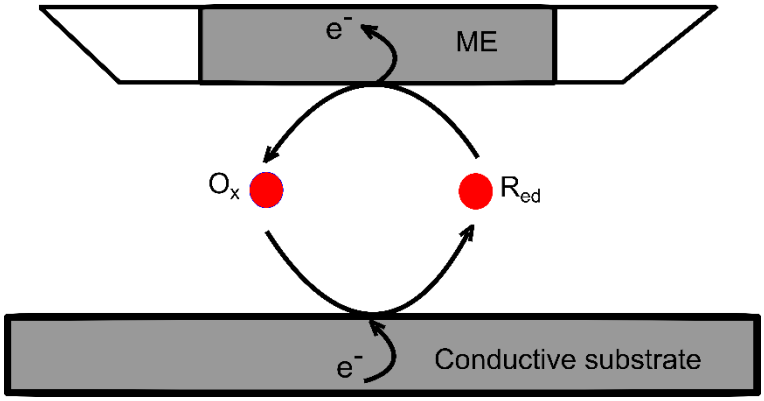

Figure 19: redox cycling of the redox active specie between the surface of ME and conductive substrate.

The molecule transfers much more charge when the oxidation is repeated several times compared to the charge transfer that is produced from one oxidation cycle. In redox cycling, the precisely controlled electrode-electrode distance is a critical parameter. Lemay et al.[147] have succeeded to produce a nanogap transducers with gaps as small as 40 nm. Using nanoscale recessed ring-disk electrode arrays was another idea to obtain the effective redox cycling. For this reason, an array of zero-dimensional nanocavities with each containing a ring electrode and a recessed disk electrode were created[148]. As extension for this method, dual-ring electrode arrays were used to allow optical access to the cycling redox species[149]. In the same manner, Byers et al.[150] have suggested a new idea to amplify the current via redox cycling with lower noise level. They have decreased the noise background by confining the volume of electrochemical process in a droplet which decreases the reaction volume. A micropipet with four channels was used in this approach. Two channels were filled with pyrolyzed carbon (working electrode) and the others were filled with electrolyte solution for Ag/AgCl quasi-reference and counter electrodes (QRCEs). One of the working electrodes was held at a reducing potential and the other at the oxidation potential. The particle undergoes several oxidations and reductions in redox cycles, so the current response is associated with the oxidation and/or the reduction of the NP itself.

2.4.3 Detection by catalytic amplification

At nanoscale collision, the current output only slightly exceeds the steady state current by value that cannot be distinguished. To study a single oxidation events, catalytic NPs such as Pt, Au,

IrO_x were studied via SEC[13,18,19,21,135,139,140,143,151–153] by promoting the oxidation of electroactive species after these NPs collide with the surface of ME (Fig. 20a). Thus, the current amplification is related to the electrochemical process that is catalyzed by the NPs not to NPs-electrode interaction.

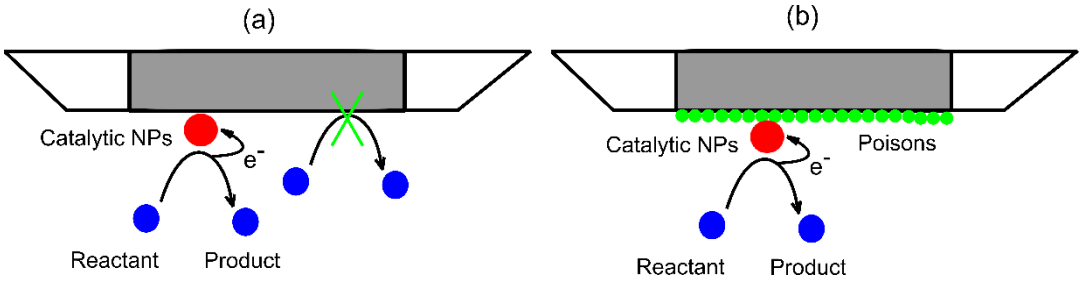

Figure 20: Electrochemical amplification process, (a) catalytic nanoparticle, (b) no catalytic conversion at a passivated ME.

Bard et al.[139] have used Pt NPs to catalyze the oxidation of the hydrazine (N_2H_4) on an Au electrode and IrO_x NPs on a Pt electrode for water oxidation. Also, the individual impact of RuO_x NPs at the electrode surface was inspected by H_2O_2 oxidation[143]. The quantity of the transferred charge depends on the residence time of the particles at the electrode surface and the catalytic activity of the particles[60]. So, the recognition of NPs activity is realized from the corresponding electrochemical reaction. In these experiments, the working electrode behaves only as an electrical conductor. However, studying the electrocatalytic activity is restricted to electrodes, at which the substrate of the catalytic reaction does not react by itself[154]. For example, it is not possible to study Pt NPs with all types of ME. So, Macpherson has introduced Boron doped diamond as a disk UME that can be used to study a wide range of catalytic NPs types[155].

The output current can be related to the deactivation of NPs itself at the electrode surface. To exclude this effect, Stevenson et al.[152] have used Pt NPs to oxidize hydrazine (N_2H_4) at a Pt UME after poisoning the electrode surface (Fig. 20b). They have poisoned the working electrode at a potential where as small as possible Faradaic current flows in the presence of redoxactive species. Upon the inject of the catalytic NPs into the solution, *i-t* trace was formed. The number of events corresponds to a collision between the inert working electrode and the

catalytic particles. Modifying the electrode surface[151,153] is another way that was used to avoid the effect of the electrode on the transient current of the electroactive species. Crooks and co-workers[151] have passivated Au MEs with polyelectrolyte multilayer films to study the electrooxidation of hydrazine (N_2H_4) at Pt NPs surface. The modifying film at the electrode surface was polarized opposite to the particle surface. Subsequently, the collision frequency of NPs could be electrostatically controlled. Bard's group[156] also modified a Pt ME with a thin TiO_2 layer to study the collision of NPs. The benefit of the modifying layer is to prevent the electron transfer between the electroactive species in the solution and the bare electrode and permit the electron tunneling after Pt NPs landing on the surface. Unwin's group[132] has checked the efficiency of the modifying effect on the collision of NPs by using SECCM where a small electrochemical cell is provided compared the size of ME. They have passivated the Au substrate with self-assembled monolayers to study the oxidation of ferrocyanide.

With more progress to amplify the current, Zhang et al.[157] have used fast-scan cyclic voltammetry instead of constant-potential techniques to study SEC of NPs by catalyzing an electrochemical process. In this technique, the Faradic current was enhanced further by using high scan and repetition rates. Therefore, the current response was recorded at higher time resolution and the interfacial kinetics of NPs is better understood. Although the catalytic amplification is a desired method, it is restricted to the particles that are electrocatalytically active. So, it is not possible to study SEC for NPs that are not electrocatalytically active.

2.4.4 Detection by partial conversion

Beside electrocatalysis, SEC can be detected by direct electroanalysis[158]. Unlike the amplification method, the particle is not used as mediator to promote an electrochemical process but the particle itself is modified at the electrode surface and the current response is recorded. The electrode firstly is potentiostated to a potential high enough to modify the particle. If articles contact the electrode, they are modified. In a multiple impact scheme, a particle can be modified partially and could be pushed away and return to the electrode to start a new modification and the process repeats until the particle is completely dissolved (Fig.1b). The measured current–time transient reflects the quantity of charge transfer by the collision. The number of registered events was used to define NPs concentration[159], size of the particles[160] and the activity of the particles[161].

Several important questions were mentioned in this respect. Are NPs destroyed in one step or with multiple collision? Are NPs dissolved totally or partially? And how much time is needed for the NP to disappear or to be converted to a product. To answer these questions, extensive work was completed in this scope[25,27,29,30,134,136,138,144,145,158,162,163–165]. Compton's group has recorded single events of the direct oxidation of Ag NPs at the electrode surface for the first time[145]. Each effective collision produces a current–time transient. The number of these transients indicates the concentration of the NPs and the charge that is consumed during an individual collision allows the determination of the NP size using Faraday's law. Based on these results, dissolution of the NPs at the electrode surface leads to an effective method for particle size and particle size distribution analysis [164]. This allows to examine the agglomeration and/or aggregation of NPs[134]. The particles may aggregate during the collision as found by Koper et al.[135], when they studied the oxidation of hydrazine (N_2H_4). They recorded a long tail of large current steps which was attributed to the aggregation effect. However, the concentration of nickel and silver NPs was determined through the direct collision with the electrode surface for aggregating and non-aggregating NPs[159,166].

Indeed, size of NPs is the important limitation factor in this method. The upper limiting size of NPs for the direct SEC was checked[163]. In this study, 100 nm Ag NPs were used as the maximum size of the NPs. They have found that these particles do not undergo complete dissolution in one event. The trials to find out the smallest NPs in SEC are more popular and more complex because the corresponding current that is produced during the collision is very limited. Bartlett et al.[163] have used a lot of precautions during the measurements and the analysis of the collision spikes. They used a cut-off filter to a cut the electronic noise and a Bessel filter[167] to filter the large noise at higher frequencies. At some point, the filter dissipates some Faradaic spikes during the processing. For example, if the particle is oxidized with multiple events, subpeaks will be formed in between the sharp anodic dissolution. These small peaks may overlap with the background current. So, selection of the frequency should be very precise to avoid missing of the spikes[165]. However, Ustarroz et al.[25] could study the electrochemical dissolution of single Ag NPs with diameter ranging from 10 to 100 nm upon impact on glassy carbon. The result proved that 10 nm Ag NPs dissolve electrochemically in a single event and NPs > 10 nm dissolve with several steps. They have deduced that the collision current is more significant on large particles than on small ones. This observation was useful for the interpretation of the subpeaks that are found in case of multiple collision. A large anodic current spike is produced in case of a single event, but several subpeaks will follow the first

peak if the collision is composed of multiple events. This means that the oxidation with multiple steps produces shrinking NPs until complete dissolution. To characterize the NPs, the oxidation of the NPs should go to the complete dissolution in a single event because the average charges transferred in a single peak are found to be about 50% lower than that of the first sub peak of multi-peak events[30]. Zhang et al.[30] have introduced a new idea to reduce the chance for a second impact of the same particle and therefore the frequency is decreased. They have decreased the dimeter of the electrode to the dimension close to the NPs size. The choice of electrolyte can affect the reliability of the sizing obtained for large NPs. It was found that at supporting electrolyte concentrations in excess of 0.1 M, the large particles can be completely dissolved where the electrolyte enhances the oxidation of Ag NPs.

Temperature control was used to ensure the total oxidation for the small NPs and the partial oxidation for large ones. At higher temperature, the probability to leave the electrode surface is higher. Temperature control was used[29] to prove that particles with diameters larger than 50 nm undergo partial oxidation and that small ones are completely dissolved. It is found that the charge passed per single event changed at higher temperature for large NPs. In case of smaller than 50 nm in diameter, the charge passed per single event did not change with temperature because particles remained at the electrode surface.

2.4.5 Detection by blocking

If the NPs are not redox active, it is not possible to study these NPs with the previous methods (electrocatalytic or particle conversion). The blocking technique was suggested as alternative to study SEC for these particles[20–24]. The report of Lemay et al.[168] opened up the possibility to use a blocking method as a new technique to study SEC. They have monitored the adsorption events for 25 nm CdSe nanospheres on UMEs by blocking the electron transfer between an electroactive species and the electrode surface. They found that the current decreases when the NPs landing on the ME active area. In a blocking approach, NPs are stuck at the electrode surface by diffusion-limited flux and/or electrophoretic migration and are irreversibly adsorbed (Fig. 21)[13,20–24,133]. In that aspect, two assumptions can be argued. The electrode surface is covered completely with the particles and the flux of a probe compound (mediators) to the electrode surface is prevented temporarily or permanently. The other possibility is that the particles stick to the electrode surface and blocks a portion of the electrode active area.

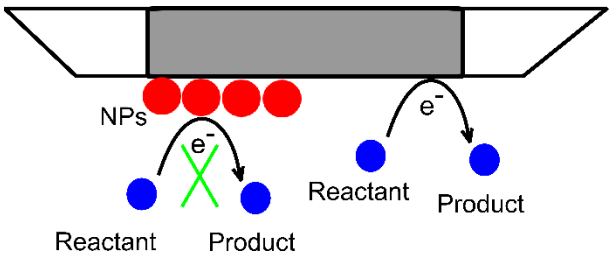

Figure 21: Single entity collision studying under the blocking effect.

In absence of NPs, the redox active species diffuse to the electrode surface and produce an anodic steady state current. When NPs stick at the electrode surface, the redox active species cannot be reach to the electrode surface. Therefore, the electron transfer between the redox active species and the electrode could be effectively blocked. Subsequently, a staircase-shaped decrease in steady-state current is recorded. The edge effect has to be considered when evaluating the current measured by blocking effect especially in case of the disk electrode. Because radial diffusion on a disk UMEs is largest at the edges, there is a non-uniform distribution of Faradaic current density on the electrode surface. Thus, if a particle lands on the edge of an UME, it will block more current than a particle of the same size and dimensions landing at the center of the electrode[24]. Based on the ability to discrete the adsorption events temporally[168], the adsorption events of individual sub-µm silica and polystyrene NPs at UMEs were observed by blocking the diffusion of ferrocene methanol (FcMeOH) to the electrode surface[21]. This technique was also been used to observe single molecules that are electrochemically inactive such as DNA and glucose oxidase[24].

2.4.6 Single entity collision recording

When a suitable potential is applied at the ME, random collision occurs between NPs and the electrode surface. The observation of these collisions was achieved through the corresponding transient current or spike output[139]. To record single events by electrochemical measurements, the events should be separated spatially or temporally[169]. If a single NP in solution hits the electrode surface, the charge transfer starts, and a discrete Faradaic current is produced. The Faradaic current can be monitored as a staircase signal[135,170] (Fig. 22a) for catalytic amplification or spike responses[139] for particle dissolution (Fig. 22b). If the particles interact

with the electrode surface continuously and a second particle sticks to the electrode surface before the first one leaves a staircase signal is formed with several plateaus where each plateau indicates arrival of a single particle. On the other hand, spikes are produced in case of the instantaneous sticking or dissolution. The number of spikes denotes the number of particles modified at the electrode surface.

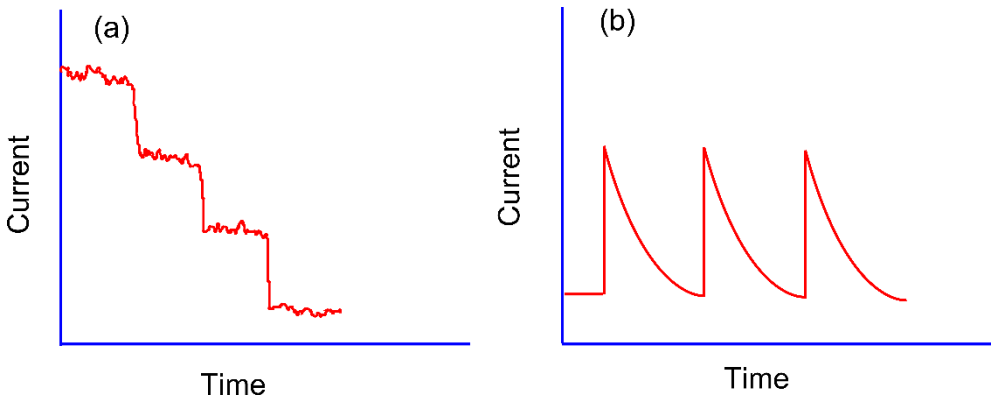

Figure 22: Current signal recording, (a) staircase signal, (b) spike response.

2.4.7 Optical detection strategy

Optical methods are appropriate to study the collision electrochemistry with the opportunity to resolve quantitatively the electrochemical current associated with individual NPs spatially and temporally [171]. The optical methods are favoured here over electrochemical detection in SEC because they are readily accessible and the signal does not need amplification[172]. Several optical imaging techniques were used to measure the interfacial charge transfer rates of single NPs including SPR techniques[31,146,173–176], fluorescence spectroscopy[34,38,172,177], dark field microscopy (DFM)[32] and Raman spectroscopy[34,172,178]. To record the electron transfer through the collision with more spatial resolution and higher throughput, the optical methods were used complementary to the electrochemical methods[174,179], where the optical methods can also be used to confirm that the electrochemical spike belongs to the collision or other effect, especially in case of the multiple collision. Additional information is needed regarding the movement of the particle towards the electrode surface. In that case, Kanoufi et al.[175] found that the collision of the Ag NPs and the shrinking event occur at a slightly different time scales and cannot be completely synchronized. The shrinking of Ag NPs was observed optically in a

ms time scale after the electrochemical signal has appeared. The optical imaging of the single $LiCoO_2$ NPs during the electrochemical cycling[180] is another example that shows the importance of the combination between the optical and electrochemical methods. The variation of the refractive index during the oxidation of $LiCoO_2$ NPs was observed by surface plasmon resonance microscopy (SPRM). The refractive index of single $LiCoO_2$ NPs was significantly decreased with the gradual extraction of Li-ions. Due to the correlation between the size of NPs and the degree of the scattering, (DFM) was used to monitor the growth[32] and dissolution[173] processes of individual Ag NPs. Thus, the current response for single NPs can be derived.

Fluorescence are broadly used in applications where the fluorescent entity can be either the target entity itself or is used to label the target entity. Therefore, it was used abundantly in the field of SEC. Most fluorescence applications used to detect SEC involve the switching of a fluorophore between fluorescent (on) and non-fluorescent (off) or monitoring the progress of the fluorescence. Firstly, fluorescence was exploited to study a single molecule collision by Bard and Barbara[39,181], then extended to study the single particle collision[54,182]. Compared to the electrochemical techniques, fluorescence-based techniques are more sensitive to study SEC[183–185]. While each effective molecule collision produces only one or two elemental charges in electrochemical methods, several photons are produced in optical methods by repeated absorption/emission or scattering events. The fluorescence recording is based on detecting a change in the fluorescence property of the particle upon oxidation/reduction at the electrode surface. Zhang et al.[54] have imaged the collision process of Ag NPs by single-particle fluorescence microscopy. It was seen that the fluorescence intensity was increased and decreased upon the oxidation of Ag NPs and formation of Ag_2O. Although Ag_2O itself is not significantly fluorescent, under intensive light illumination, Ag_2O can undergo photoreduction and photodissociation and generates small Ag clusters which are strongly fluorescent.

For nanoscale particles, it was difficult to hunt the single particles by optical-based methods because of their fast-diffusion. So, insufficient spatial and temporal resolution is provided by these methods. Most of the optical methods resolve this problem by immobilizing the particles at the electrode surface[186]. In our project, FCS was used and preferred for different reasons. Firstly, FCS studies the kinetics of the particles inside the confocal volume without requirement of immobilization, where the diffusion and number of particles are the main output information that are deduced from FCS. Secondly, fluorescence-based techniques have some drawbacks such as photostability. Enough emission intensity and thus sufficient excitation power is required to produce enough signal to overcome the optical background with

freely moving particles, photobleached particles can continuously be replaced. Furthermore, in FCS the analysis is not related to the fluorescence itself but to the fluctuation of the fluorescence. Thirdly, FCS is applicable of measuring over a wide range of correlation times from picoseconds to tens of seconds with sub-millisecond time resolution which is useful for kinetic and dynamics measurements[50]. The presence of the electrode surface inside the confocal volume will affect the dynamics and kinetics because the steady state of the movement inside and outside the confocal volume could be affected. Thus, the diffusion of the particles towards the confocal volume will change compared to a section of composable size in the solution bulk. The information about the direct collision of the particles at the electrode surface will be obtained by analyzing the corresponding fluctuation data. The intensity of the photon bursts can also be an indication to study the collision. Lei et al.[38] have coupled a single molecule fluorescence spectroscopy with cyclic voltammetry to study the single oxidation/reduction events of cresyl violet. They found the oxidized state of cresyl violet emits strong fluorescence and its reduced state yields very weak or no fluorescence. On the same principle, the photon bursts and the current spikes will be synchronized to study the collision of very small luminescence NPs at the electrode surface. This study will occur either directly using conventional electrochemistry or indirectly using (BPE).

2.5 Bipolar electrochemistry

2.5.1 Overview on bipolar electrochemistry

Bipolar electrochemistry (BPE) is a technique that is used to generate oxidation and reduction reactions simultaneously on two ends of the same electrode, called bipolar electrode (BE). Unlike the conventional electrochemistry, no physical connection between the working electrode and the power supply is required. According to the polarization induced by an external electric field, one pole works as anode and the other works as cathode. In conventional electrochemistry, the driving force of the redox reaction is controlled by tuning the potential of the working electrode but in BPE the electrochemical process is induced by the electric field generated in the solution. Based on the location of the BE in the solution, BPE can be divided into open BPE and closed BPE as illustrated in Fig. 23.

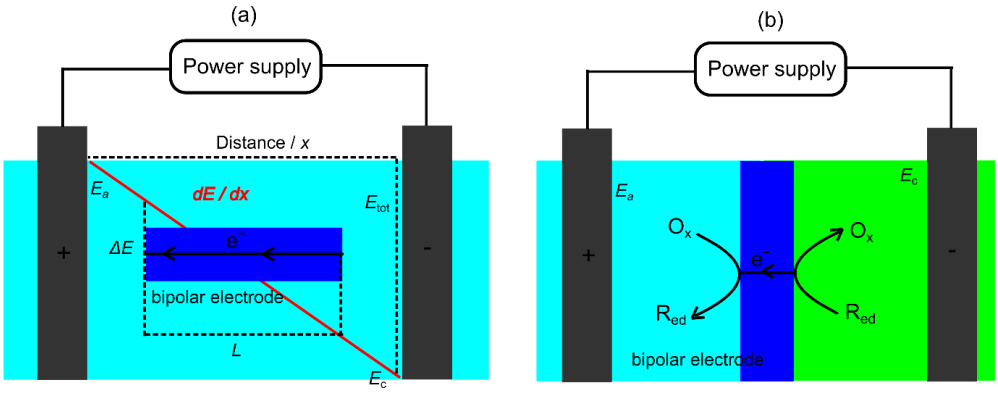

Figure 23: The principle of bipolar electrochemistry, (a) closed and (b) open BPE configuration.

Open BPE configuration is a method where the electrode is immersed in a homogeneous electrolyte solution (Fig. 23a). When an external potential is applied between two feeder electrodes and electric field distortions due to reactions at the feeder electrodes are neglected, a potential gradient is created in the electrolyte solution. The potential difference between the poles of BE is a fraction of the total potential that is dropped to the solution through the feeder electrodes. At enough potential difference between the poles (above the threshold value), charge can be exchanged between solution and BE and move from one pole to the other pole. Consequently, the anodic and cathodic reactions will occur simultaneously. The maximum potential difference across a (BE) is calculated by Eq. (23)[187], where E_{tot} is the applied external potential, L is the length of the (BE) and x is the distance between the feeder electrodes.

$$\Delta E = E_{\text{tot}} \left(\frac{L}{x}\right) \tag{23}$$

The total current that flows through the cell is equal the current passing through the BE plus the current flowing through the solution via migration of charged species. The passing current through the BE is called the Faradaic current. In that case, the resistance of the solution and the conductance of the electrode are very important to increase the Faradaic current. At high resistance of the electrolyte, the migration effect will be suppressed. Also, the conductance of the BE must be as high as possible to to avoid potential drop in electrode.

Closed BPE configuration is the construction of a BE as conductive connection of two independent compartments where the electrolyte is physically separated (Fig. 23b). Unlike the open configuration, the potential across the electrode is not a fraction of the total driving force that is provided from the power supply, but it is the same. The voltage is dropped almost

entirely at the solution interface adjacent to both ends of the bipolar electrode[188]. So, less driving force is required in this method compared to open BPE. Furthermore, no by-pass current flows through the electrolyte and subsequently the electrochemical current is measured directly through the BE. In a closed BPE there is a flexibility to control the parameters such as the BE materials, geometry of the electrode, the threshold of potential difference between the poles and the driving force created at the feeder electrodes. Because the oxidation medium is separated from the reduction medium, different electrolytes and electroactive species can be used. These features increase the probability to use this type of BPE in the applications. In electroanalysis, one pole works as a sensing part while the other works as the reporting part. This separation is very useful also in case of studying thermodynamically unstable mixtures of redox such as using $(Ru(bpy)_3)^{2+}$/TPA as an electrochemiluminescence reporter for the electrochemical detection for $(Fe(CN)_6)^{3-}$[189]. In such context, the driving force is applied into two compartments. Consequently, the huge background signal that comes from the proximity between the feeder electrode and the BE can be avoided[190].

Due to the physical separation between the sensing part and reporting part, the limitation of the volumetric response must be considered. The volumetric response is described by determining the diffusion-limited steady-state current, i_{ss}, for each pole of a BE separately. The limiting current of the BPE depends on the chemical composition of each compartment as well as the size of the BE and the feeder electrodes. The pole that has less i_{ss} is called the limiting pole while the other is called the excess pole. The pole with a smaller limiting current, or the limiting pole, can be studied from the overall voltammetric response. However, a large Faradic current on the excess coupling pole is important. It facilitates the observation of a fast voltammetric response[191].

2.5.2 Microelectrochemical application of bipolar electrochemistry

When an external potential is applied between two feeder electrodes, a potential gradient is created in the electrolyte solution. In the presence of a conductive materials, negative and positive poles are created simultaneously. So, the BE works as wireless because no physical cable is required to connect the (BE) to the external power supply. These features of BPE increase their application in various fields such as sensing[192–194], catalysis[195], analyte separation[196,197], electrochemical synthesis[198,199], batteries[200], electroactive species studying[188,194] and nanoscience studying[185,201,202].

The anodic dissolution of a metallic BE by an oxidation reaction has been adapted for several applications The corrosion of the metals and the resistivity of the metals towards corrosion were easily studied[193]. Water reduction at the cathodic pole enhances the dissolution of metals at the anodic pole. Catalyzing the oxygen reduction reaction is other application based on the electro dissolution principle. When Ag microband electrodes are dissolved further, it was found that the efficiency of the oxygen reduction reaction increases[195]. The deposition of the materials by BPE also provides a simple procedure that simplifies some of the complications associated with micro and nanofabrication. The electrodeposition and the electrodissolution processes were used together to create directional growth of copper deposits between copper particles that are not connected to an external circuit[198]. On the same way, gradient polymer surfaces also were performed by generating two poles on the surface of the monomer between two feeder electrodes[199]. Asymmetric particles called Janus particles also were prepared by BPE which display an efficient and distinctive capabilities for example to target complex self-assembled materials. These particles refer to particles that are composed of at least two components of different nature. BPE is used also as alternative to electrophoresis. Instead of the influence of an electric field, the concentration enrichment inside the capillary was achieved by a BE that existed inside the capillary[197,203]. Simultaneous dissolution of a BPE at its anodic pole and subsequent deposition of the same metal at the cathodic pole was used for the directed linear motion of metallic objects by a process called self-regeneration. Thus, BPE provides the suitable environment for generating such gradient based on the potential gradient alongside the BE[204]. Breaking the symmetry[196] of the chemical system is another way to induce the motion of the small objects either directly or indirectly. BPE is an efficient method that can break the symmetry of chemical systems in a straightforward way.

Recently, BPE has been demonstrated to be a powerful tool for the electrochemical detection of the electroactive species with high throughput. The BPE dissolution was used as a reporter for a recognition event where the decrease in the length of the BPE can be directly correlated to the number of electrons passing through the BPE and hence to the sensing reaction at the cathode. The reduction of p-benzoquinone and DNA[194]were studied by monitoring the corresponding dissolution of Ag at the other pole. On the other hand, the oxidation of the target material can be studied by the coupling with other reduced material. The oxidation of redox species, e.g., dopamine, on the carbon disk was coupled with the reduction of soluble oxygen on the inner carbon fibre[188]. For more spatial and temporal resolution, a BEs arrays were built

up in parallel[205,206]. The existence of a large microelectrode array (MEA) plays an important door in the recording the electrochemical process. It was much advantageous and convenient for many practical purposes[207]. A closed configuration array of (BEs) was designed for multiplexed cancer biomarker analysis[208]. The design of devices with several channels allows controlling the spatial resolution and throughput. Moreover, avoiding the extra cost of driving force where a several BEs are operated with just one driving force. At very low scan rate, the voltammetric response of MEAs becomes similar to the macroelectrode with the same electrode area but with lower background charging current. The reason behind that is the more planar diffusion that is produced by the overlapping of the diffusion layers of the MEs. To obtain a rapid steady-state response and higher electrode density, the MEA system was extended to MEAs-based double electrode system[209].

More recently, the principle of BPE was used to analyze single entities. To study single entities electrochemically, the single entity should be confined either near to or inside the electroactive interface. Furthermore, the requirement to the bipolar electrodes with nanoscale dimension is very essential to synchronize with reduction/oxidation events on the other pole precisely according to Kostiuchenko's et al.[210] theoretical analysis,. They introduced that is not possible to observe one-to-one correspondence in coupled bipolar redox events when the overall dimension of the bipolar electrode is above 10 nm. They approved that the number of electrons residing on the BE fluctuates as a result of the random faradaic processes and the potential fluctuations become vanishingly small for macroscopic electrodes. For these reasons, Hao et al.[202] have used a focused-ion beam (FIB) milling technique to fabricate BEs with nano-scale. This approach is based on the usage of a beam of focused gallium ions in a FIB microscope. A platinum organometallic compound is decomposed and platinum atoms are deposited at the orifice of a solid-state nanopore by highly focused ions . In a bipolar cell, the Pt nanoparticle acts as a closed BE. Interestingly, the most important factors in the electrochemical response of the electrode such as the shape, the size and the location can be readily controlled by the deposition depth of the deposited nanostructure. In addition to that, the attention was focused on a newly emerging nanopore sensing method that confines the bipolar electrochemistry process into the nanopore to detect singe redox molecule. Nanopores provide an electrochemically confined space in which single molecules can be captured and efficiently converted into the measurable electrochemical signatures with high temporal and current resolution[211]. Toward these goals, a confined nanopore electrode as a "wireless" nanoelectrode was proposed[212] to enhance the transient ionic current for the small redox

molecules, particles and ions and to reduce the interference signal from the driving electrode. If the nanopore was coated with nanoscale conductive layer, it could provide a highly confined electric field within which the bipolar electrochemical reactions occur. Therefore, the redox reactions at nanoscale can be measured with high throughput. Taking a silver-coated open-type wireless nanoelectrode (WNE) as an example, at sufficient potential applied across the conductive silver layer drives the bipolar redox reactions, the generating H_2 and Ag^+ tackes place at the anodic pole (δ^+) and the cathodic pole (δ^-), respectively[201]. The confinement effect amplifies the current of H_2 bubbles generation at the orifice of the nanopore which can detect the electrochemical redox reactions process of Ag ions quantitatively. Two types of WNE configurations was proposed base on the strategy of the conductive layer deposition inside the nanoelectrode. The open-type WNE is fabricated by coating a metal nanolayer on the inner wall of the nanopipette while the closed-type WNE is performed by occupying the full space at the nanopipette tip with a conductive metal. On the other way, Ma et al.[201] have developed a wireless single-electrode electrochemical (WSEE) system for ECL detection based on the potential difference induced by the resistance of electrode. BPE induces a gradient of electrochemical driving force along the polarized conducting object. This intrinsic characteristic has been exploited here to spatially address electrochemiluminophores with differing oxidation potentials in a wireless manner[213]. The effect of the morphology on confinements in the nanopore was inspected by Seo et al.[214]. They have found that the electroluminescence intensity is enhanced when the thickness of the nanopore is increased. In electrochemistry, microdroplet system is used to isolate the analyte from the surrounding for high throughput. For this purpose, a microdroplet was integrated with a closed bipolar cell[215].

Beside to the confinement effect for the nanopipette, it was used to minimize the applying potential. Previously, large voltages were required to initiate bipolar reactions over the particle length which causes some undesirable noises. The ability of nanopipettes to reduce the applied potential by focusing it on the orifice of the pipette was exploited by Han et al[185] to generate BPE reaction on the surface of very small NPs. Beside to the nanopipettes, they used resistive pulse sensing to observe the translocation of silver nanoparticles. When the conductive particles such as Ag NPs move from the bulk solution close to the orifice of the nanopipette, two redox reactions can be coupled on the two poles of the nanoparticle. These reactions are dependent on the voltage drop across the orifice being equal to or greater than the voltage requirement for the coupled reactions. They detected large current blockages that they attributed to the translocation of single Ag NPs through a quartz pipette pore. The reduction of

water inside the pipette and the oxidation of silver in the bulk solution, produces H_2 molecules, which may nucleate and form a H_2 nanobubble. Consequently, these nanobubble increasing the apparent volume of the Ag nanoparticle and causing a current blockage with a much greater magnitude than a bare particle.

Since the charge transfer transferred through the BE is related to the concentration of the analyte, determining the minimum concentration of the analyte is very important issue in the sensing field especially in in case of single molecule detection. Reporting very dilute redox active species requires high sensitivity technique, thus allowing significant SNR gains by accumulating the reporting signals. Different methods were established for this purpose. The detection limit of the phosphate buffer solution[216], hydrogen peroxide (H_2O_2)[201,217,218], human serum samples[192] and DNA were checked checked[219]. To increase the sensitivity of the detection, Yu et al.[219] have integrated the square wave technique with a BPE. The square-wave technique allows an electroactive analyte to be regenerated by applying a reverse potential Consequently, ECL signal was reinforced and high SNR obtained.

2.5.3 Coupling bipolar electrochemistry and optical detection

The center idea of coupling electrochemistry and spectroscopy is the amplification of the electrochemical signal and the good temporal and spatial resolution of the optical output[220]. The requirement for this coupling becomes very important at single molecule or particle measurements levels because the output current is extremely low. Since anodic and cathodic currents at the BE have to be equal[191], the optical signal at the reporting pole serves to derive the bipolar current. The electrochemical reaction of interest takes place at one pole of the BE, whereas the optical signal is generated by a couple electrochemical reaction such as electrochemiluminescence[201,213,214,216,218,219,221,222], electrochromism[223,224], Raman spectroscopy[225,226] and electrofluorescence[37,40,183,185,227,228] on the other pole. In case of coupling of conventional electrochemistry and spectroscopy, the electroactive species to be studied has to be optically active. For example, if fluorescence detection is coupled with electrochemical detection, the electroactive species must be a fluorophore or luminescent particle, or at least a fluorophore precursor. In contrast to that this condition is not important in case of coupling BPE with spectroscopy because the electrochemical part (sensing part) is separated from the optical (reporting part). So, coupling the BPE with spectroscopy is a good chance to study a wide range of electroactive materials. Interestingly, applications related to

the oxidation and the reduction of the electroactive species can be studied by this method. The type of the reaction depends on the polarization which is controlled easily by changing the polarization on the feeder electrodes and the type of the dye as well. If the target entity has to be oxidized, the dye must be fluorescent in reduced state and non-emitting in oxidized state. On the other hand, the dye must be fluorescent in oxidized state and non-emitting in reduced state in case of studying the reduction.

To transform the Faradaic current at the two poles of the BPE to the recognized optical signal, electrochemiluminescence (ECL) was first introduced to the BPE. In chemiluminescence (ECL), the reporting part contains luminophore and the co-reactant. The electrons generated at the sensing pole initiate the luminophore to react with the co-reactant at the reporting pole, therefore the excited state of the luminophore is populated. Consequently, the ECL is created without requirement to the excitation light source. However, ECL is not able to emit more than one photon per transferred electron. The two most popular ECL systems used in that context are either tris(2,2-bipyridine)ruthenium $(Ru(bpy)_3)^{2+}$[221] and tri-n-propylamine (TPA) or 3-aminophthalhydrazide (luminol) and hydrogen peroxide (H_2O_2) couples[229]. For example, $(Ru(bpy)_3)^{2+}$ /TPA system was used as indicator to detect c-Myc mRNA in Breast Cancer Cells was detected[230] and luminol/H_2O_2 to study the deposition of an electroactive inorganic layer[231].

In electrochromism based methods, the electrochemical reactions occurring in the analytical cell are coupled to an electrochromic reaction. When the charge transfer through the BE, the color of the chromatic material changes. A methyl viologen is an example that is used to study the corresponding electrochemical reaction[224]. The solution of methyl viologen changes from colourless to purple solution after the reduction. Raman spectroscopy[225,226] also was used to monitor the synthesized gradients of CdS and Ag-Au alloys using (BE) position.

Notably, most of the C-BPE based analysis including reporting is mainly carried out with the ECL as the readout to record the Faradaic reaction at the two poles. Fluorescence is another phenomenon that was used as optical signal to record the electrochemical reaction. The fluorescence analysis using BPE is relatively rare compared to the ECL-based analysis. Fluorescence-based analysis has high background compared to the ECL-based analysis. However, it is more sensitive than ECL-based reporter because of the possibility to emit more than one photon per transferred electron. In the fluorescence-based techniques, the oxdiation state of the fluorophore itself changes. So, using the fluorescence as a reporter is more sensitive

than the other reporters. Spatially resolved data regarding the electrochemical reactivity can be provided in a real time by coupling fluorescence microscopy to electrochemical methods[36,37,232].

The fluorescence-based reporter based on switching the fluorophore between on-state and off- state that is induced by bipolar reaction. Under conditions where the Faradic current is not limited by the reporter. The electrochemical events on the sensing pole can be monitored via fluorescence microscopy. Towards this goal, very strongly fluorescent molecules are required to report the events on the other side. The advantage of the generated pH gradients in combination with a pH-sensitive fluorescent dye such as fluorescein was exploited to study the redox activity of the molecules[228].

Resazurin[37,183,202,206] is a dye widely used to report the oxidation of the redox pieces on the other pole. It is reduced irreversibly to a strongly fluorescent molecule called resorufin[233]. At more reductive potential, resazurin is reduced further producing a new non-fluorescent material called dihydroresorufin. It is oxidized reversibly to resorufin and used to report the reduction of the redox spices[205]. However, the measurement using irreversible dye reporter is not accurate because the fluorescence decay is achieved solely by diffusion, the removal is slow and incomplete upon the electrochemical circuit is switched off. Therefore, a significant temporal and spatial resolution will be lost. To record single fluorescent particles on an electrode, the diffusion of fluorogenic molecules must be taken into account. Fan et al.[183] demonstrated a new method to restrict the diffusion in one dimension. The requirement was satisfied by confining the fluorogenic molecules inside the nanopipette. The oxidation of FcMeOH was done at the anodic pole of a Pt BE outside the capillary and the reduction of resazurin was done at the cathodic pole of the electrode inside the capillary. By confining the reporting fluorogenic part inside the Pt nanopipette in one dimension, signal-to-noise ratio was enhanced, and irrelevant fluorescent molecules was excluded. The small reporting volume was essential to isolate the individual molecules and provide an effective optical confinement[234]. Oja et al.[206] have suggested a fluorescence enabled electrochemical microscopy (FEEM) as a new technique to detect the electrochemical events precisely. The key concept of FEEM includes visualizing the electrochemical signals at several parallel BEs by fluorescence microscopy simultaneously. They have built up 2- and 3-D images of the diffusion layer using a large array of parallel bipolar electrodes[206]. The existence of a large electrochemical array plays an important role in the recording the electrochemical process with more spatial and temporal resolution. Furthermore, the difference of the resolution quality between the

reversible and non-reversible was checked out using resazurin[37] and dihydroresorufin[205,206] by FEEM method. Dihydroresorufin imaged the redox reaction with more resolution compared to resazurin due to the reversibility of dihydroresorufin dye.

The accuracy and sensitivity in our project are more important because very small concentration of the redox species have to be measured. These measurements will be used as a reference for the studying of single NP interactions at the electrode surface. So, a reversible fluorescent reporter is required. The reversibility of the redox dye that switch between fluorescent and non-fluorescent upon potential modulation is very important to monitor the charge transfer event precisely[38,39,235]. Consequently, the rate of single redox detection can be correlated precisely to the rate of molecular generation.

3 Experimental

3.1 Chemicals and materials

Chemicals	Source
Se powder (99.99 %)	Sigma Aldrich, Taufkirchen, Germany
Na_2SO_3 (98 %)	Sigma Aldrich, Taufkirchen, Germany
$CdCl_2.5/2\ H_2O$ (99%)	Acros Organic, Geel, Belgium
Na_2S (60-64 %)	Acros Organic, Geel, Belgium
Mercaptoacetic acid (97 %)	Alfa Aesar, Karlsruhe, Germany
Carboxylate-capped CdSe/CdS QDs	Sigma Aldrich, Schnelldorf, Germany
Cytidine	Carl Roth GmbH & Co. KG, Karlsruhe, Germany
$HAuCl_4$	Sigma Aldrich Chemie GmbH, Steinheim, Germany
$AgNO_3$	Carl Roth GmbH & Co. KG, Karlsruhe, Germany
Rhodamine B	Sigma Aldrich Chemie GmbH, Steinheim, Germany
Fluorescein	Sigma Aldrich Chemie GmbH, Steinheim, Germany
Ag NPs (100 nm)	NanoComposix, Sandiego, California, USA
FcMeOH	Strem Chemicals, Newburyport, Massachusetts, USA
KNO_3	Carl Roth GmbH & Co. KG, Karlsruhe, Germany
$K_2[PtCl_6]$	Sigma Aldrich Chemie GmbH, Steinheim, Germany
Resazurin	Sigma Aldrich Chemie GmbH, Schnelldorf, Germany
Tris(bipyridine) ruthenium(II) chloride	Sigma Aldrich Chemie GmbH, Steinheim, Germany
N,N-bis(2,5-di-tetra-butylphenyl)-3,4:9,10-perylenebis(dicarboximide) (DBPI) (97 %)	Sigma Aldrich Chemie GmbH, Darmstadt, Germany)
Ammonium cerium (IV) nitrate solution	Sigma Aldrich Chemie GmbH, Schnelldorf, Germany

3.2 Quantum dots and metallic nanoparticles

3.2.1 Preparation

Quantum dots with negative shell: QDs were prepared according to the synthesis described by Bao et al.[236] Na_2SeSO_3 was prepared by refluxing 79 mg (1.0 mmol) from selenium powder and excess of Na_2SO_3 (252 mg, 2.0 mmol) in 50 mL water. The solution was refluxed for 10 h at 100°C until all selenium powder had reacted. 20 mL (0.02 mol L^{-1}) fresh solution of Na_2SeSO_3 was added to 50 mL N_2-saturated basic solution (pH 10) of 137 mg $CdCl_2 \cdot 2.5H_2O$ (0.6 mmol) and 80 mL mercaptoacetic acid (MAA) (1.1 mmol). After injection to the Na_2SeSO_3 solution, the mixture was further stirred for 60 min and a clear yellow CdSe suspension was obtained. From this suspension, CdSe/CdS was prepared by adding 100 mL solution containing 360 mg $CdCl_2 \cdot 2.5H_2O$ (1.6 mmol) and 150 mL MAA (14×10^{-3} mol L^{-1}), followed by adding Na_2S (100 mL) (1.6×10^{-3} mol L^{-1}) dropwise. The final yellow CdSe/CdS suspension was refluxed at 80 °C for 3 h.

Quantum dots with positive shell: To prepare positive QDs, MAA was replaced by cysteamine. 1.5 mL (0.02 mol L^{-1}) fresh solution of Na_2SeSO_3 was added carefully and dropwise to 25 mL N_2-saturated neutral solution (pH 7) containing 137 mg $CdCl_2 \cdot 2.5H_2O$ (0.6 mmol) and 80 mL cysteamine (1.1 mmol). The solution was stirred during the addition of the selenium solution. Green luminescence appeared when the pH of final solution reached a value between 5.5 and 5.9. In that case, the amount of selenium is very critical because it alters the value of pH and therefore affects the luminescence property.

Ag-Au metallic NPs: The synthesis of Ag-Au NPs was done according to Thang et al[237]. In this method, cytidine was used as a template to promote the solubility of NPs in water. 40 µL of 50 mM cytidine (0.002 mmol) was added to 1.56 mL of water. During the stirring, 100 µL of 5 mM $HAuCl_4$ (5.0×10^{-4} mmol) was added stepwise followed by adding 200 µL of 0.5 M citrate buffer (0.1 mmol) (pH = 6). At this pH, citrate is working as reducing agent. Thence, the mixture was heated by water bath to 80 °C for 20 minutes, followed by addition of 100 µL of 5 mM $AgNO_3$ (5.0×10^{-4} mmol). Finally, the luminescent AuAg nanoclusters were formed with negative cytidine shell.

3.2.2 Spectroscopic characterization

TEM measurements: TEM images of synthesized CdSe, CdSe/CdS QDs and Ag-Au NPs were taken using a JEOL JEM2100F TEM microscope (JEOL GmbH, Freising, Germany) operated at an acceleration voltage of 200 kV. The QDs were deposited onto a carbon coated Cu TEM grid (400 ECF300-Cu-50, Science Services GmbH, Munich, Germany). For the calculation of particle size distribution, the program ImageJ was used. Particle size distribution was calculated for 100 particles.

UV-Vis absorption spectroscopy and spectrofluorimetry: The absorption spectra of Ag-Au NPs and QDs were recorded in the UV-visible region with a spectrophotometer (SPEKOL 2000, Analytik Jena, Germany). The parameters were set to 2 nm slit width, 1 nm steps and scanned at wavelength range from 400 nm to 700 nm. The emission was characterized by emission spectroscopy (Spectrofluorometer FS5, Edinburgh Instruments, U. K.) in 1-cm quartz cells. The emitted light was collected by using 1nm steps and 1s dwell times. It was scanned one times between 450 nm and 800 nm. The ratio of photons emitted for QDs was measured relatively to Rhodamine B (Rh B). QDs (unknown Φ_F) and Rh B (known Φ_F= 0.31)[238,239] were excited at a wavelength where both have the same absorption. 500 nm was chosen to excite CdSe and 491 nm in case of CdSe-CdS. Integrated fluorescence intensity was measured under the same instrumental conditions and range from 530nm to 800 nm. The quantum yield was calculated by Eq. (2).

3.2.3 Electrochemical investigation

Electrochemical characterization of ($4.1 \cdot 10^{15}$ particles/L) commercial CdSe/CdS QDs (Sigma Aldrich, Schnelldorf, Germany), synthesized CdSe/CdS QDs and synthesized Ag-Au NPs by cyclic voltammetry (CV) and differential pulse voltammetry (DPV) were performed in 0.1 M phosphate buffer solution (pH 7.4) as supporting electrolyte by using a three electrode setup with a Pt working electrode, a Pt wire as auxiliary electrode and an Ag/AgCl electrode (CH Instruments, Austin, USA) as reference electrode and a potentiostat (Autolab, Metrohm, Utricht, Niederland). 50 mVs^{-1} scan rate and 0.1 mV step size were applied for CV measurements. In case of DVP, the measurement scanned with 50 mVs^{-1} and 5 mV was used as step size. The pulse height was 25 mV. CV was also done for ($4.1x10^9$ particles/L)

commercial Ag NPs (NanoComposix, Sandiego, California, USA) in 0.1M $NaNO_3$ supporting electrolyte.

3.3 Electrochemical techniques for signal recording of charge transfer

3.3.1 Chronoamperometry

Chronoamperometry is an electrochemical technique that measures current as a function of time. The chronoamperometry measurements for CdSe QDs were carried out in a Faraday cage by using a Pt ME as working electrode, a Pt sheet as auxiliary electrode and Ag/AgCl as reference electrode. All electrodes were connected to an NPI potentiostat (NPI electronic GmbH, Model VA-10X, Tamm, Germany). The potentiostat was connected to a FPGA card (Nstional instrument, Pcle-7852 R, Austin, Texas, USA) that was programmed by Björn Mageney (PhD student in the group of Prof. Gunther Wittstock, Oldenburg university, Oldenburg, Germany). The measurements were performed with electronic filtering and without filtering. The filtering was done under different ranges of frequency between 20Hz and 20kHz. The highest gain in this setup (50 mV/pA) was used. Several concentrations of CdSe in phosphate buffer solution (pH=7.4) were oxidized at +0.6 V. Origin program (2018, 64_bit,b9.5.0.193) was used to identify and integrate the impact spikes. The electrical noise was filtered by applying Fourier transform filtering between 800 Hz and 30 kHz.

3.3.2 Stripping measurements

Anodic stripping experiments were performed for CdSe QDs in phosphate buffer solution (pH = 7.4) with the NPI potentiostat using platinum working electrode (3 µm), platinum counter electrode and Ag/AgCl reference electrode. Firstly, (-1.2 V) was applied to reduce the cadmium ion and adsorb it at the electrode surface. After that the striping was done by applying the oxidation potential (+0.6 V). The reduction was applied for different times to accumulate more ions that is enough to produce observable spikes after at the oxidation potential.

3.4 Microelectrodes

3.4.1 Fabrication of ME

The pulling/sealing process for ME preparation was performed with a laser puller (Sutter instrument Co., Model P-2000, USA). The original pulling scheme[129,240]was adapted to match the alignment state of the setup. A platinum wire of 25 µm of diameter was placed in a quartz capillary with outer and inner diameters of 1 mm and 0.7 mm, respectively. The electrode preparation was done by five consecutive steps (Fig. 24). In a first step, the empty quartz capillary is pre-thinned using a single line program (Settings Heat: 560, Filament: 3, Velocity: 60, Delay: 140, Pull: 0). This step was essential to obtain symmetrical tip and facilitate insertion of the platinum wire in the middle of the capillary. Secondly, a platinum wire was cleaned with water and ethanol, dried and placed in the center of the quartz capillary. Sealing of the platinum wire into the quartz capillary was achieved by using a single line program (Heat: 470, Filament: 3, Velocity: 60, Delay: 140, Pull: 0,) repeated for five times. Number of cycles and the heat of sealing depend on the stability of the instrument. For this reason, checking the instrument from time to time is required. During the sealing, the electrode was evacuated via a vacuum pump to avoid air bubbles inside the electrode sealing. Thirdly, the pulling program was applied, using higher heating powers (Heat: 650, Filament: 3, Velocity: 100, Delay: 100, Pull: 200). Fourthly, the obtained raw MEs were grinded by a micro-grinder (EG-400, Narishige, USA) up to the conical section of the wire. When this section was reached, the polishing process was repeatedly interrupted to estimate the diameter of the ME by optical microscopy. The polishing was terminated when the electrode diameter was in the range of 1 to 2 µm. Finally, a copper wire was inserted in the open end of the glass capillary and connected to the Pt wire by silver glue (EPO-TEK® H20E-LV, Billerica, USA).

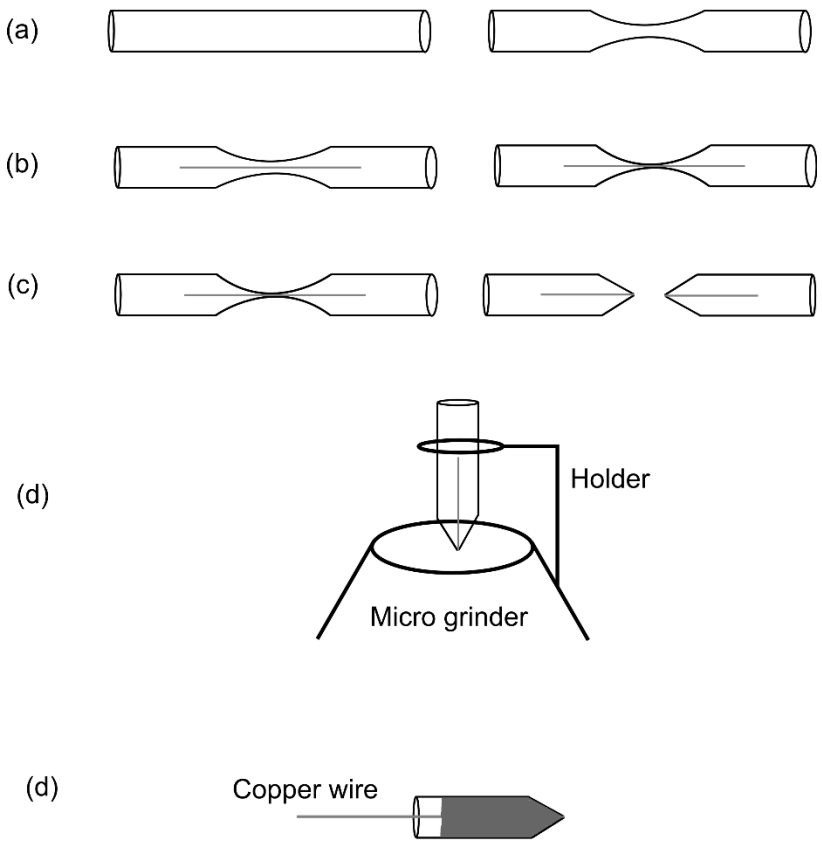

Figure 24: Microelectrode preparation steps, (a) Empty quartz capillary is pre-thinned. (b) A cleaned platinum wire is placed in the center of the quartz capillary and sealed. (c) The capillary was pulled and cut into two electrodes. (d) The obtained raw MEs were grinded by a micro-grinder. (e) A copper wire was inserted in the open end of the glass capillary and connected to the Pt wire by silver glue.

3.4.2 Characterization

Cyclic voltammetry: Cyclic voltammograms of 1 mM of ferrocene methanol (FcMeOH) in 0.1 M aqueous KNO_3 solution were used for checking the electric connection and surface quality of MEs. The measurements were performed by using a potentiostat (Metrohm Autolab, KM Utrecht, Netherlands) in a three-electrode setup with the ME as working electrode, a Pt wire as auxiliary electrode and an Ag/AgCl electrode as reference electrode.

Laser scanning microscope: The flatness and exact diameter of the ME were determined using a confocal laser scanning microscope (Leica TCS SP2, Leica microsystem GmbH, Heidelburg, Germany) equipped with a HC PL Fluotar 50x/0.8 dry lens. A series of scans in a reflection mode at a wavelength of 633 nm, gain of 400 V and amplification format of 1024X1024 were performed.

3.4.3 Platinum deposition on microelectrodes

In order to obtain a non-reflecting ME surface, Pt-black was electrodeposited in a three-electrode setup equipped with the MEs as working electrode, a Pt wire as auxiliary electrode, and an Ag/AgCl electrode as reference electrode. The electrolyte consisted of 4.8×10^{-5} M of $K_2[PtCl_6]$ and 4.5×10^{-3} M KNO3 in 50 mL of highly purified water. The deposition potential of -0.3 V vs. Ag/AgCl was applied for 10 s using a potentiostat (Autolab, Metrohm). The deposition was controlled with a CMOS camera (Andor Neo 5.5, Model DC-152Q-Fl, Ser.No SCC-0807, Oxford, England) connected to a confocal laser scanning microscope. The parameters of the camera were set as 0.5 s exposure time, 200 MHz read frequency and 16-bit resolution.

3.5 Combining conventional electrochemistry with single molecule fluorescence spectroscopy

3.5.1 Single molecule spectro-electrochemical setup description

In the setup of the (FCS) for the single particle experiments, optical and electrochemical parts were connected as depicted in Fig. 25. The optical part is a standard FCS setup[100,118,241,242] assembled in our laboratory. The filtered output of a super continuum source (2–3 mW, SuperK Extreme, NKT, Birkerød, Denmark) was operated at 470 nm, which is suitable to excite CdSe/CdS QDs emitting in the yellow color range. The bandwidth was set at 25 nm. The excitation light was collected by a dichroic mirror (DMLP505R – 25 mm×36 mm, Thorlabs, Newton, New Jersey, USA) and reflected into a high numerical aperture oil immersion objective (Nikon Plan Fluorite 100x, NA 1.3, Thorlabs). The power measured on top of the objective was adjusted to 50-100 μW. The emitted light was collected by the same objective and passed through the dichroic mirror and a clean-up filter (FELH0500, Thorlabs). Confocal detection was achieved with a 25 μm pinhole. The filtered light was divided by a 50% of beam splitter and detected by two single-photon avalanche detectors (ID 100–50 single photon detection, IDQ, Carouge, Genève, Switzerland) for noise reduction. Data readout and signal processing were performed with a single photon counting system (Simple-Tau, Becker&Hickl, Berlin, Germany). A camera (DFK31AU03; The Imaging Source, Bremen, Germany) was included to adjust the position between the laser focus and ME.

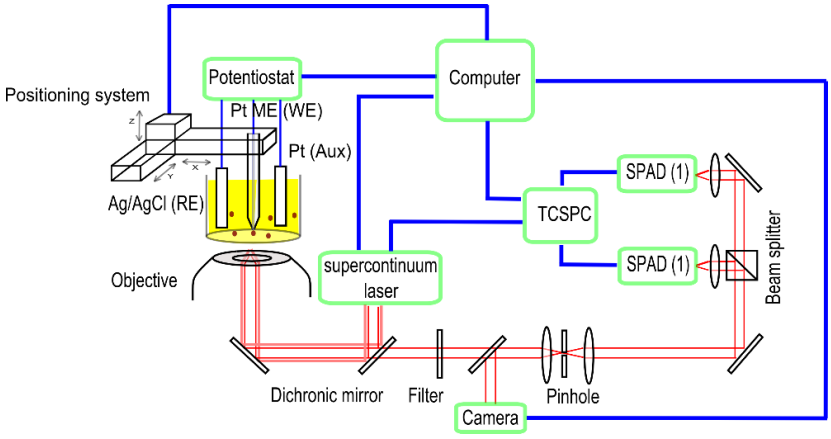

Figure 25: Single molecule spectro-electrochemical setup.

The in-house programmed SECMx program[243] was used to control the potentiostat (PalmSens4, model PSO321, Netherlands) and the positioning system (MS30 and PS30, mechOnics GmbH, Munich, Germany) for the Pt ME as working electrode. The electrochemical cell consisted of an in-house-built Teflon cell with a 5 mm opening in the middle and was tightened to an Al base plate. The solution was electrically isolated from the base plate by a 160 µm cover slide placed between Teflon cell and base plate. The cell was operated as three-electrode cell with a Pt ME as working electrode, a Pt wire as auxiliary electrode and an Ag/AgCl electrode as reference electrode, to which all potentials are referred to.

3.5.2 Data analysis and fitting parameter

The stock solution of commercial CdSe/CdS QDs, synthesized CdSe/CdS QDs and synthesized Ag-Au NPs were diluted with a phosphate buffer (pH=7.4) by a factor of approximately 1000, 500 and 50, respectively. The factor was adjusted according to the minimum dilution that can produce enough SNR. After that the solution was sonicated with a horn sonicator (Digital sonifier 250 d, Branson, USA) for 30 min to avoid aggregation. The size of the confocal volume was calibrated before each measurement with 0.5 nM fluorescein solution and was typically 1.2 fL[50,100,114,244,245]. The measurements were done at short integration time (10 min) and relatively long integration time (20 min).

The cross correlation function $G(\tau)$ was calculated from the normalized overlap integral of the emission intensity $I(t)$ recorded by detector 1 with the corresponding intensity measured

by detector 2 plus a lag time τ according to Eq. (12).[50,114,115,118]. The correlation functions obtained from the FCS measurements were fitted using Eq. (11)[50,98,118,246]. Data acquisition was performed by Becker and Hickl SPCM software (Becker&Hickl GmbH, Berlin, Germany). The operation mode was set on parameter-tag fifo (First in First Out) and was used for FCS and lifetime measurements, where a continuous stream of photon data is saved up in the memory. In this mode, full information about each photon is recorded such as: the time in the repetition period (micro time), the detector channel (1 or 2) that used to detect the photons and the running experiment time (macro time)[247]. The count signal was adjusted between 1000 and 2000 counts s^{-1} by adjusting the excitation power. This was achieved by controlling the laser power at definite wavelength (470 nm) and bandwidth (25 nm). To supress the Raman scattering, the time gate was set to 5×10^{-8} s. The Burst Analyzer data evaluation software (Burst Analyzer 2.0, Becker&Hickl GmbH, Berlin, Germany) was used to analyze peaks in time traces and perform calculations on the full traces for data analysis of FCS and TCSPC data. The start parameters were selected close to values expected from the QD characterization. In our analysis, the aspect ratio between the radii of the short and long axes of the observation volume was fixed to 0.25 because this relation is expected from the numerical aperture of the objective, while the lag time τ was set to10^{-2}-10^{3} ms. This time range covers any time-dependent effects influencing the number and the duration of emission fluctuations observed in the FCS measurements which have a rate constant in that range.

3.5.3 Time correlated single photon counting (TCSPC)

The QD emission decay time τ_F was measured by time-correlated single photon counting (TCSPC) using the single molecule spectroscopy setup described above. For TCSPC measurements, the internal pulse picker of the supercontinuum source was employed to reduce the repetition rate from 80 MHz to 3.9 MHz. At low repetition rate, full decay information is obtained for long decay components. The time range was decreased to 2×10^{-7} to suppress the Raman scattering. The trigger was done at values higher than the threshold value (-29 mV) and -5.3 V was selected as zero cross level to operate the triggers at a constant fraction of the pulse amplitude. The decay functions were fitted using a three-component exponential model by Origin (2018, 64_bit, b9.5.0.193). To compare the lifetime for two measurements, the smallest two components were fixed at definite value.

Principle of TCSPC: is a digital technique that used to detect single photon events and their time of arrival with respect to the excitation pulse. It is constructed to way that less than one photon is detected per laser pulse. If more than one photon arrives only the first one will be detected. If the number of arriving photons increase, the apparent decay time becomes shorter and the decay becomes non-exponential[50]. Because the dead time of the electronic is much longer than τ_F and only the first driving photon has to be detected, the photon counting in TCSPC is limited to 1 photon per 100 laser pulses.

While the higher repetition rates source is essential to accumulate adequate number of photon events for a required statistical data precision, it is not efficient for measuring longer-lived decay where less information about the long-component decay (Fig. 26-dashed red line), The reason for this is that excitation and emission cycles occur many time in short time. In this case the sample will be re-excited before fully decayed.

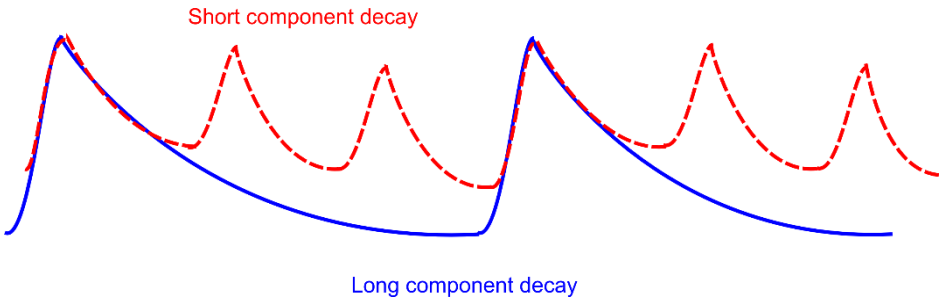

Figure 26: laser pulse with different repetition rate.

To avoid the pulse overlapping between the decays, time ranges between two pulses should be 10-20 times that of the expected lifetime to be measured (Fig 26 blue line). In this case, the new pulse starts after the excited molecules return completely to the ground state with full decay and high data acquisition times.

In the classical TCSPC, the excitation pulse is used to start a constant function discriminator (CFD) channel and the emission pulse to stop it. All the photons that reach the detector after the first photon will be missing and cannot enter the CFD, because the first photon closes the TAC channel. This effect is called pile-up. To provide the highest probability of recording one photon per cycle, TCSPC measurement was used in a reverse mode (Fig. 27).The setup was constructed for measuring the time delay between the excitation and emission.

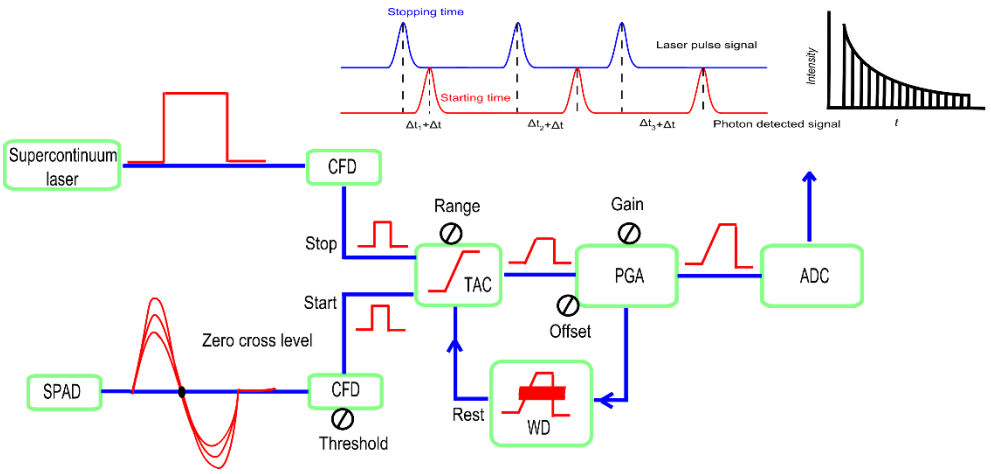

Figure 27: start-stop configuration of TCSPC.

In this method, CFD is started by the detector pulse and stopped by the laser pulse. The width of the time bins for starting-stopping time converts to a voltage ramp by TAC. The voltage signal in TAC channel is directly proportional with the time. These signal passes through the amplifier (PAG) and leaves as bigger signal. To obtain output with a readable result, an analog-to-digital converter (ADC) is employed to convert the voltage signal to the numerical value. The difference in time between last laser pulse and the detection of a photon, called time bin (t) plus fixed time with (Δt) is outputted regard to the single events to a histogram. If the signal not in the range of the events, it is suppressed by a window discriminator (WD).

3.6 Combining bipolar electrochemistry with fluorescence spectroscopy

3.6.1 Setups description

In this setup, an inverted epi-fluorescence microscope (Leica microsystem GmbH, Heidelberg, Germany) was coupled with BPE (Fig. 28). The BPE was used as a closed configuration. It was composed of two compartments. One was used as a sensing part and the other as a reporting part.

In the reporting part, the sample was illuminated by a tungsten lamp and filtered using a cube with a (BP 450-490) excitation filter, a (510) dichroic mirror, and a (LP 515) emission filter. The excitation and emission wavelengths were chosen based on the fluorescence spectrum of the fluorogenic reporter. The fluorescence output was acquired at 20× magnification using a sensitive camera (Andor Neo 5.5, Model DC-152Q-Fl, Ser.No SCC-

0807, Oxford, England) cooled to -30 ^{0}C. Andor SOLIS software was used for video recording. Videos were recorded at a readout rate of 200 MHz, exposure time of 0.5 s and 16-bit resolution. Background images were taken before each video.

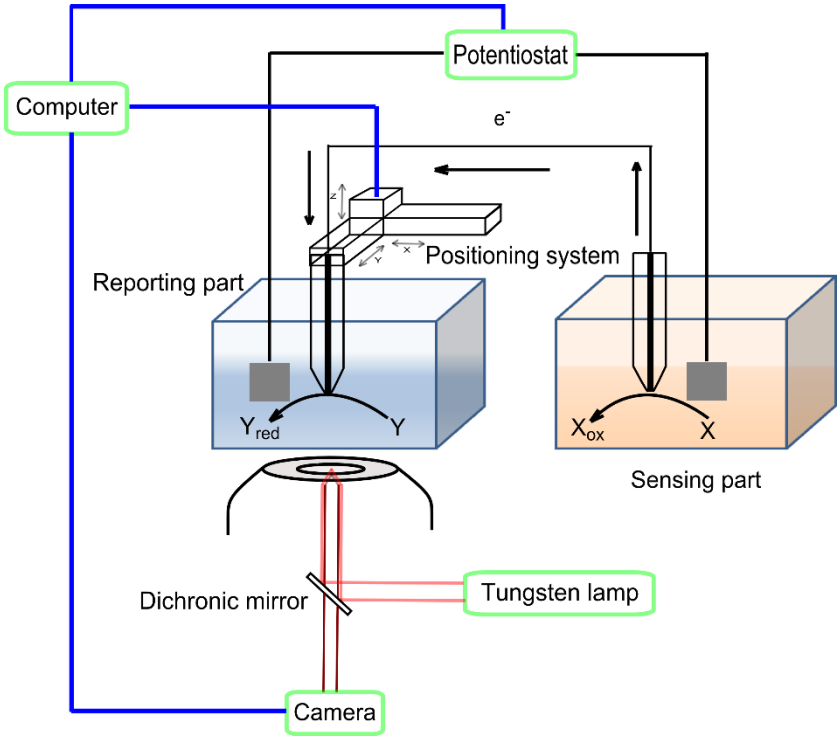

Figure 28: Bipolar spectroelectrochemistry setup.

In the sensing part, the cell contains the material of interest where the BE was used to connect the reporting and the sensing part. A closed (BE) was created by connecting two 25 µm diameter MEs in series. The pole in the reporting cell was set as cathode while the pole in the sensing cell as anode. The potential was applied across two platinum feeder electrodes. The feeder electrode in the sensing part was connected as a working electrode and in the reporting part as a counter and reference electrode. The in-house programmed SECMx program[243] was used to control the potentiostat (PalmSens4, model PSO321, Netherlands) and the positioning system (MS30 and PS30, mechOnics GmbH, Munich, Germany) for the Pt ME as working electrode. The (BE) in the reporting part was adjusted at fixed distance above the microscope for all measurements.

3.6.2 Cyclic voltammetry by bipolar electrode

Cyclic voltammetry experiments were carried out using the NPI potentiostat. The electrochemical cells were equipped with two platinum feeder electrodes and BPE of Pt were connected in series (Fig. 28). One feeder electrode was connected as a working electrode and the other was connected as reference and counter electrode. A scan rate of 0.5 V/s was used for all CV experiments. One cell contains 1 mM FcMeOH in 50 mM KCl electrolyte solution and the other contains 1 mM resazurin in 50 mM carbonate buffer (PH=10). The feeder electrode in resazurin solution was set as working electrode and the feder electrode in FcMeOH was set as a counter and a reference electrode. After that, the feeder electrodes were exchanged to be the working electrode in the FcMeOH solution while the a counter and a reference electrode in resazurin solution.

3.6.3 Measurement of the oxidation of FcMeOH and commercial QDs

The oxidation of FcMeOH and QDs was coupled with the reduction of a fluorogenic dye. Different dyes (Tab. 1) were used to report the oxidation of the interested material such as 1 mM resazurin and Tris(bipyridine)ruthenium(II) chloride, both soluble in water, and N,N-bis(2,5-di-tetra-butylphenyl)-3,4:9,10-perylenebis(dicarboximide) (DBPI) which is only soluble in organic solvents. 1 mM of the fluorogenic dyes were used to report the oxidation of different concentrations of FcMeOH (1 ml to 1pM) in 0.1 M potassium nitrate or different concentrations of CdSe-CdS QDs in phosphate buffer solution (pH 7.4) at the electrode surface.

Table 1: Fluorogenic compounds that were used to report the oxidation of the analyte.

Compound name	Structure
Resazurin sodium salt	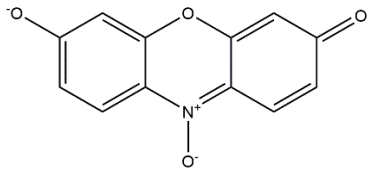
Tris(bipyridine)ruthenium(II) chloride	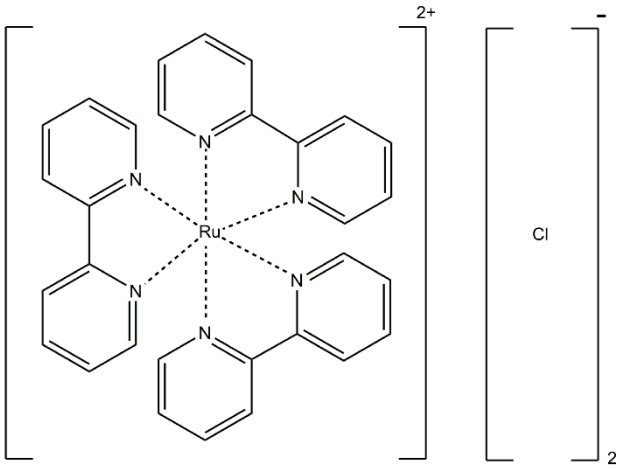
N,N-bis(2,5-di-tetra-butylphenyl)-3,4:9,10-perylenebis(dicarboximide) (DBPI)	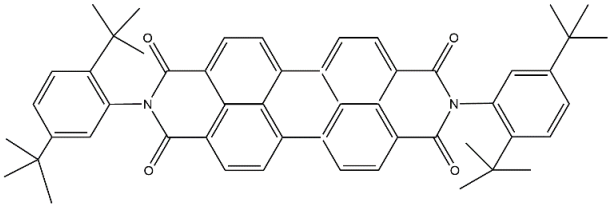

3.6.4 Preparation of Tris(bipyridine)ruthenium (III) chloride

1 mL of 0.1 M ammonium cerium(IV) nitrate solution was added to 10 mL of 1mM stepwise. The mixture was strongly stirred until a clear green ruthenium(III) complex was obtained. Blue light was used to observe the vanishing of the luminescence. The disappearance of the luminescence means that the ruthenium(II) was oxidized completely to ruthenium(III).

Monitoring ruthenium (III) preparation by UV-Vis absorption spectroscopy and spectrofluorimetry: Absorption, emission and excitation spectroscopy were used to check the

progress of the reaction. 0.1 M cerium(IV) solution was added to 10 mL of 1 mM ruthenium(II) solution gradually by 0.1 mL steps. After each addition, the solution was stirred strongly, then absorption, emission and excitation were recorded. The absorption spectra were recorded in the UV-visible region with a spectrophotometer (SPEKOL 2000, Analytik Jena, Germany). The parameters were set to 2 nm slit width, 1 nm steps and scanned at wavelength range from 350 nm to 700 nm. The emission and excitation were characterized by spectrofluorometer (Spectrofluorometer FS5, Edinburgh Instruments, U. K.) in 1-cm quartz cells. The solution was excited at 450 nm. The emitted light was collected by using 1 nm steps and 1 s dwell time. It was scanned one time between 550 nm and 800 nm. To measure the excitation spectrum, the emission wavelength was set to 607 nm and the excitation was scanned between 325 nm and 550 nm.

3.6.5 Data processing

The video was converted to images via Andor SOLIS software by batch conversion. All images were processed and analyzed using the software ImageJ (Fiji/Downloads|Fiji Downloads). A circle that is fitted to the electrode diameter was drawn around the electrode (Fig. 29). The integrated intensity of the emission at the electrode surface was measured. The same size of the circle was moved to the glass surface and the intensity inside the circle was used as background.

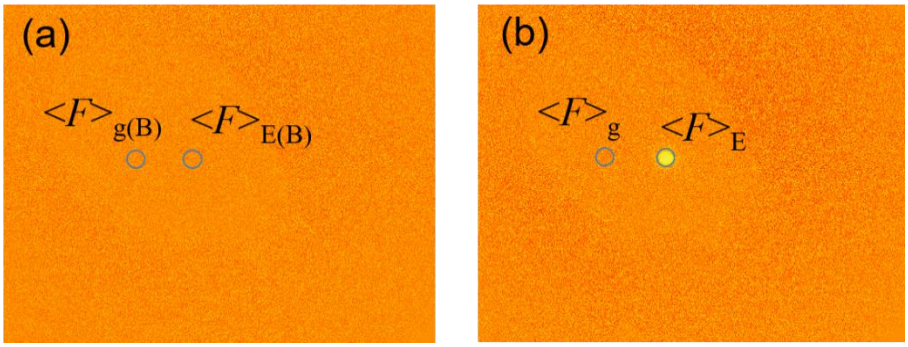

Figure 29: The processed images by image: (a) the background image where $\langle F \rangle_{g(B)}$ is the background intensity at the glass surface while $\langle F \rangle_{E(B)}$ is the background intensity at the electrode surface, (b) the higher intensity image where $\langle F \rangle_{g}$ is the photon intensity at the glass surface while $\langle F \rangle_{E}$ is the photon intensity at the electrode surface.

Two methods were used to define the emission intensity <*F*>. Firstly, it was measured by correlating the total cell fluorescence according to Eq. (24), where <*F*> $_{E}$ is the integrated intensity at the electrode surface, *a* is the area of selected cell and <*F*> $_{E(B)}$is the background intensity at the electrode surface.

$$< F >=< F >_{E} - \left(a \times < F >_{E(B)}\right) \tag{24}$$

Secondly, the intensity at the electrode surface was divided by the intensity at the glass surface for the measured image and the background image, then the background calculation was subtracted from the measured image calculation as illustrated by Eq. (25).

$$< F >= \frac{< F >_{E}}{< F >_{g}} - \frac{< F >_{E(B)}}{< F >_{g(B)}} \tag{25}$$

Where <*F*> $_{E}$ is the emission intensity at the electrode surface, <*F*> $_{g}$ is the intensity at the glass surface of the electrode, <*F*> $_{E(B)}$ is the background intensity at the electrode surface and <*F*> $_{g(B)}$is the background of intensity at the glass surface.

4 Results and discussion

4.1 Spectroscopic characterization of CdSe/CdS QDs and Ag NPs

Before studying the spectroelectrochemistry of CdSe/CdS NPs, it was essential to inspect the spectroscopic properties of QDs and Ag NPs. Spectroscopic measurements are used for different purposes combined with electrochemical measurements. However, optical and electrochemical properties are always somehow connected. For example, the electrochemical and the optical band gaps are related to each other and depend on the total coulomb interaction energy[43]. The electrochemical band gap is related to the energy required to generate a hole in the valence band by oxidation or bring an electron into the conduction band by reduction, while the optical band gap is covered by generation of an electron hole pair optically. The relation between the electron density in metallic NPs and the plasmonic excitation and emission is another example that confirms the relationship between the electrochemical and optical measurements. So, spectroscopic parameters need to be clear before changing electrochemical parameters and the optical properties must be found out before electrochemically modifying the particles.

4.1.1 Transmission electron microscopy (TEM)

Prior knowledge on the size of core is important and has an indication on the absorption and emission characterization. Size and size distribution are also important for characterizing the NPs used in our experiments because diffusion properties are closely related to the size of NPs[102]. According to the TEM micrographs (Fig. 30a, b), the mean particle diameter of synthesized QDs is around 3-4 nm as reported in literature[236]. The synthesized QDs have smaller size and a broader size distribution (Fig. 31a,b) than the commercial QDs. The size distribution also for CdSe less than CdSe-CdS which refers to the higher product density for CdSe-CdS. From the basics of TEM, the region with higher electron density is more visible in TEM image. Fig. 30a, b shows that no clear differences between the core and core shell. This is due to the presence of cadmium atom in the core as well as in the core-shell.

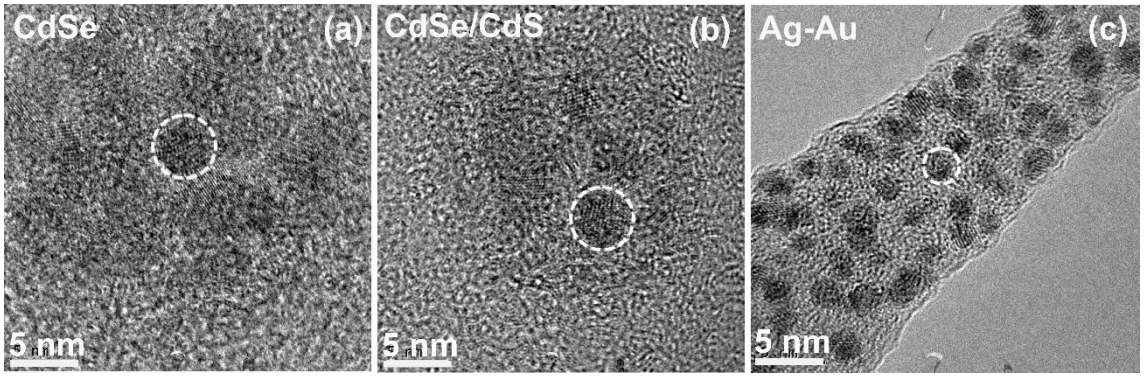

Figure 30: TEM images for (a) CdSe QDs and (b) CdSe/CdS QDs with MMA ligand in water and (c) for Ag-Au NPs with cytidine ligand. The white circles illustrate the particles size border.

In case of Ag-Au NPs (Fig. 30c), the average particle size is around 2 nm with low size distribution (Fig. 31c) which indicates to the homogeneity of the solution. Size and size distribution were similar to the results reported in literature[237,248] and supported the previously published synthetic approaches[249]. TEM images (Fig. 30) shows a clear crystal structure and crystal lattice for both QDs and Ag-Au NPs. However, the crystallinity is more prominent in case of Ag-Au NPs (Fig. 30c) caused by the metallic structure. For small nanoparticles (~2 nm or less), TEM provides a unique tool that allows direct visualization down to a single atom. So, very clear crystals for Ag-Au NPs can be seen.

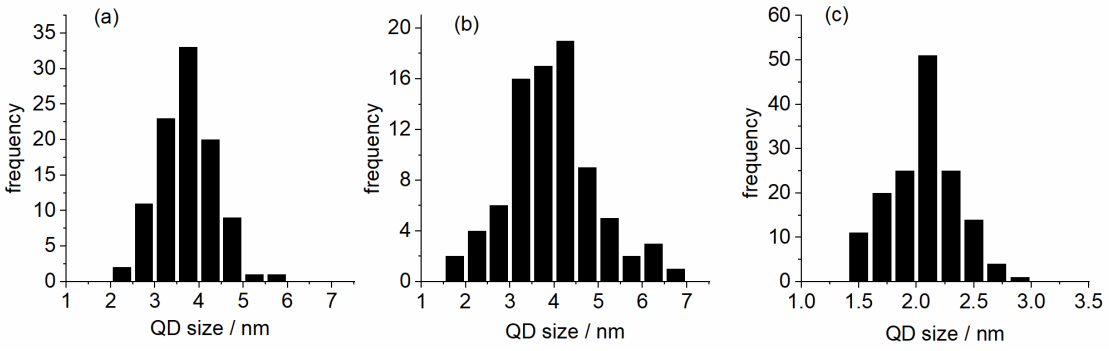

Figure 31: Size distribution of (a) CdSe and (b) CdSe/CdS QDs determined from 100 QDs, (c) Ag-Au NPs determined from 150 particles.

4.1.2 Absorption and emission characterization

Absorption coefficient, absorption wavelength and emission wavelength were necessary for correct setting of the single molecule spectroscopy setup and determining the optical properties of QDs[250]. The spectra of the commercial QDs are displayed in Fig. 32 and of synthesized QDs in Fig. 33. The onset of the absorption band with the longest wavelength was observed at 510 nm Fig. 33 as expected for synthesized QDs of this size[236].

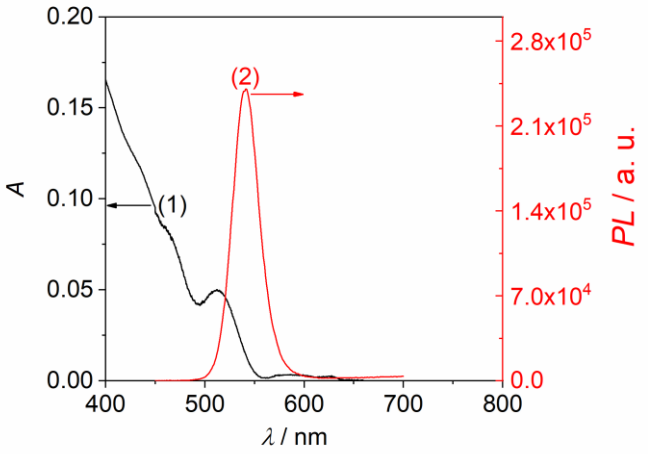

Figure 32: Absorption (1) and emission (2) spectra of commercial CdSe/CdS QDs in 0.1 M phosphate buffer solution (λex = 420 nm).

Commercial QDs have a higher absorption wavelength compared to synthesized QDs corresponding to the difference in size (3-4 nm for synthesized QDs (Fig. 30a,b) and 6 nm for commercial) which fits the quantum confinement (Fig. 6)[251], where the particles with higher surface to volume ratio (smaller size) possess higher band gaps. Compared to the commercial QDs, a broad absorption edge can be seen in the absorption spectrum for synthesized ones. The deviation on the sharpness of the absorption can be attributed to some factors such as surface defect states and size distribution[72].

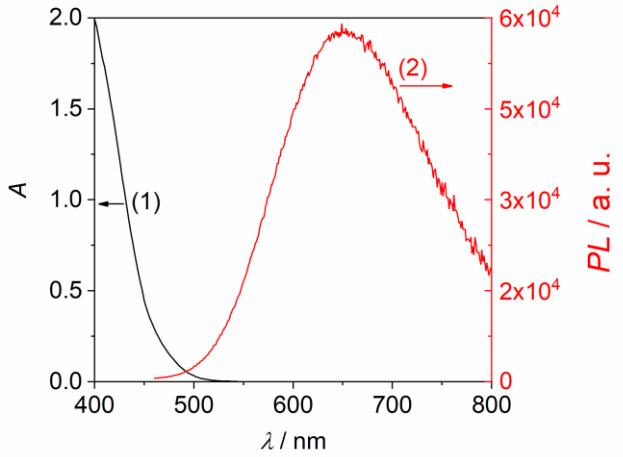

Figure 33: Absorption (1) and emission (2) spectra of synthesized CdSe/CdS QDs in 0.1 M phosphatebuffer solution (λ_{ex} = 420 nm).

The existence of defects for the synthesized QDs was also observed by the emission spectra. The broad photoluminescence spectrum at 660 nm for synthesized QDs (Fig. 33) is an a clear evidence on the distribution of the size and the existence of trap states[252]. In contrast to that the commercial QDs show a very narrow emission peak due to the thickness of the shell which completely saturates the defect states(Fig. 32).

Basically, as long as the particles are clean from defects, band gap emission is produced from the direct recombination between hot electrons in the conduction band and the holes in the valence band (Fig. 34a). As conduction and valence bands in defect free QDs are usually well defined, this will result in a narrow spectral distribution and a small Stokes shift. If there is some trapping state between the valence and conduction band, the electron will return to the valence band through these trapping state and recombines indirectly. (Fig. 34b). This journey takes longer time than the previous and called the defect emission. Because these defects are of lower energy than the conduction band and do not have a well-defined energy, defect emission shows a large Stokes shift and also large spectral distribution. This mechanism characterizes the defect emission[253] where the electron energy is dissipated through the trapping states. As apparent in Fig. 33, synthesized QDs display higher stokes shift compared to the commercial QDs (Fig. 32). The huge stoke shift for synthesized QDs agrees with the theoretical statement[254], that the stokes shift will increase as the diameter of the particles decreases. Due to the high surface to volume ratio for small QDs, the particles are more prone to the external effect such as QDs-solvent interaction. Consequently, the defect emission is

more prominent in case of synthesized QDs (smaller size). Due to the presence of defect emission, Fig. 33b shows also higher distribution of the states.

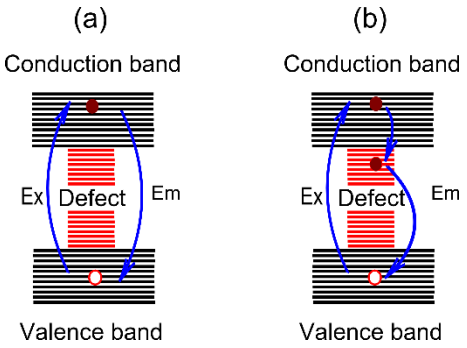

Figure 34: Band structure of QDs (a) in the absence of defect states, and (b) on the presence of defect states.

While smaller particles are very important to enhance the confinement effect and generate high band gap, a higher trap state density can be produced due to the higher surface to volume ratio. The clear effect of the shell on the quality of the QDs was studied by measuring the emission intensity as apparent in Fig. 35. It is a clear that CdSe-CdS has higher emission intensity than CdSe. Also, because the shell increases the exciton extension, the emission maximum is slightly red shifted and shows a steeper short wavelength edge than the CdSe QDs. These results agree with the conclusion that the shell saturates the defects located at the surface of the CdSe QDs well[71,252,255].

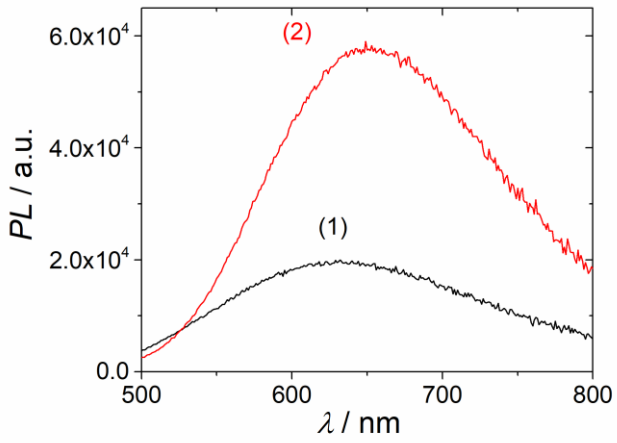

Figure 35: Emission spectra of synthesized CdSe QDs (1) and synthesized CdSe/CdS QDs (2) in 0.1 M phosphate buffer solution (λex = 420 nm).

The emission quantum yield Φ_F for QDs was measured relatively to Rhodamine B (Rh B) (Φ_F = 0.31)[238,239]. The emission quantum yields Φ_F were determined to be 0.12 (commercial CdSe/CdS), 0.07 (synthesized CdSe/CdS) and 0.03 (synthesized CdSe). The low value of synthesized QDs shows us that the particles are not clean from defects compared to commercial ones. On the other hand, the convergence between the Φ_F of CdSe-CdS and CdSe confirms that CdS shell is too thin for completely protecting the particle core from the defects. So, Φ_F value is an obvious evidence for the existence of the defects.

Absorption and emission spectra are apparent in Fig. 36 for ultra-small Ag-Au NPs (2 nm). These NPs have relatively sharp absorption edge at around 450 nm. On the other hand, the narrow emission spectrum at 595 nm confirms the low size distribution of the particles observed in TEM measurements (Fig. 31c). It can be attributed to the effect of cytidine which was used as a template to increase the stability and enhance the luminescence by changing the dielectric environment[256].

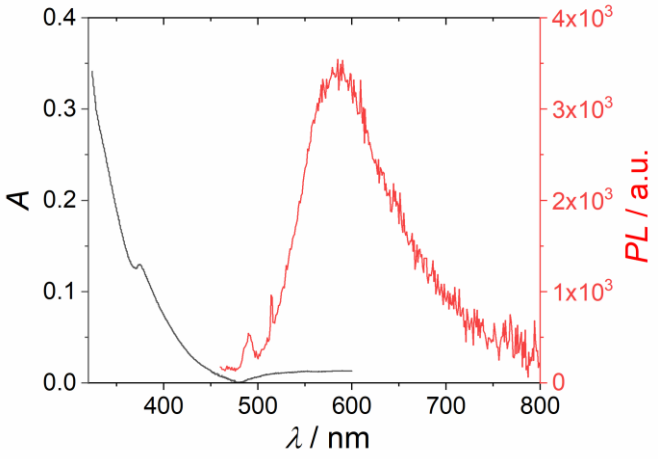

Figure 36: Absorption (1) and emission (2) spectra of synthesized Ag NPs in 0.1 M $NaNO_3$ solution (λ_{ex} = 420 nm).

4.2 Electrochemical characterization of CdSe/CdS QDs and Ag NPs

Although spectroscopic characterisation for QDs is more common than electrochemical, voltammetry was used to explain some ambiguous spectroscopic results and conclude valuable

information related to chemical composition, dimension, surface properties and redox level as well[43,257].

4.2.1 Cyclic voltammetry

CdSe-CdS: Cyclic Voltammetry (CV) is one of the electrochemical techniques which used to examine the defected surface in QDs[44,48,258–261], and give information on the valence and conduction bands of the material as well[258]. The CVs were measured for synthesized QDs over four cycles at different scan rate. The apparent CV (Fig. 37) shows only the steady state cycle (last cycle) which confirms the electrochemical expectation from literature[43,260,262]. The CV contains different peaks that belong to various events. These events depend on the location of the Fermi potential of the electrode with respect to the valence band, conduction band and the trapping states (Fig. 10)[47]. The oxidative degeneration of the QDs is evident from an irreversible oxidation at +0.6 V. The corresponding reduction wave, which would be expected in the region symbolized with an ellipse, is not observed (Fig. 37). At potentials exceeding +0.6 V, the Fermi potential of the electrode drops below the QD valence band (Fig. 10a) and electrons are irreversibly transferred from QD to electrode with subsequent oxidative degeneration of QDs[43,262,263].

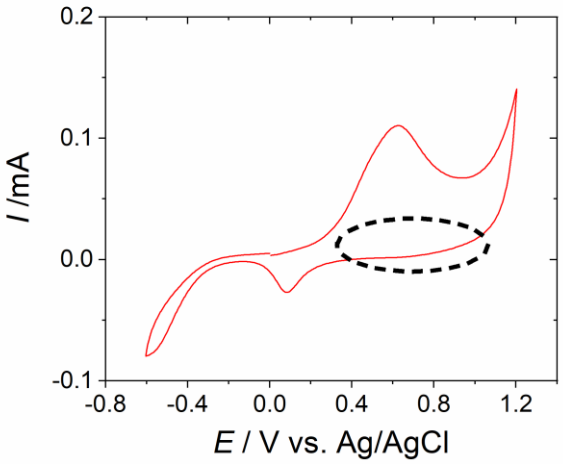

Figure 37: Cyclic voltammetry of synthesized CdSe/CdS QDs in 0.1 M phosphate buffer solution (scan rate 50 mV s-1, step size 0.1 mV).

At more negative potential, the Fermi potential of the electrode goes up close to the conduction band (Fig. 10c) and the electrons would be injected into the conduction band. However, the reduction of CdSe-CdS is not expected within the stability window of water because the bandgap of CdSe/CdS is 1.8 eV (calculated from the emission wavelength) and thus, reduction of QDs would be expected at -1.2 V while the onset of water reduction already appears at -0.4 V. At potentials in between the reductive and oxidative potential, the Fermi-level crossed the trapping state and the electrochemistry of QDs may include generation or filling of trap states (Fig. 10c)[43,45,47,48]. The small peak in Fig. 37 at +0.15 V could be as a result of the filling of trapping states with electrons. In contrast to that the broad oxidation beak at +0.6 V attributed to the existence of defect sites that were merged with the oxidation peak[264]. For this reason, the broadness of the peak is an evidence of the density of the trapping states and the energetic localization of the trapping states. In this case, the trapping states were expected to be close to the conduction band. The oxidation peak should be sharp if no defects are close to the conduction band. During the voltage ramp, the Fermi level of electrode starts to fill the trapping state with electron first before the conduction band and fill the trapping state with hole before extract electron from the valence band. So the surface defects can act as trap sites for both electrons and holes, thereby constituting oxidizing and reducing centres, respectively[258].

Commercial Ag-Au NPs: Cyclic voltammetry for 6 pM commercial Ag NPs (100 nm) was done by Pt (ME) (2 µm) to determine the current output before going further to ultra-fine synthesized Ag-Au NPs (2 nm). The cyclic voltammogram (Fig. 38a) shows that no events occurred at a freshly immersed electrode surface. The absence of the oxidation peak may be caused by different effects. The accumulation time for the particles at the electrode surface appears to be the most prominent reason as confirmed by the second cyclic voltammogram (Fig. 38b). In this case, the electrode was immersed for 10 min before the running CV and the potential was cycled four times. The oxidation of Ag NPs at the electrode surface at 0.5 V is apparent in Fig. 38b. The disappearance of the oxidation peak after the second cycle was indeed due to the oxidation and dissolution, instead of detachment of Ag NPs from the electrode surface. Furthermore, the absence of the corresponding reduction peak is an indication for the irreversible oxidation. During the immersion time, some of the Ag NPs were accumulated at the electrode surface. At oxidation potential, the particles were destroyed gradually. So, Fig. 38b shows that the oxidation peak disappears gradually.

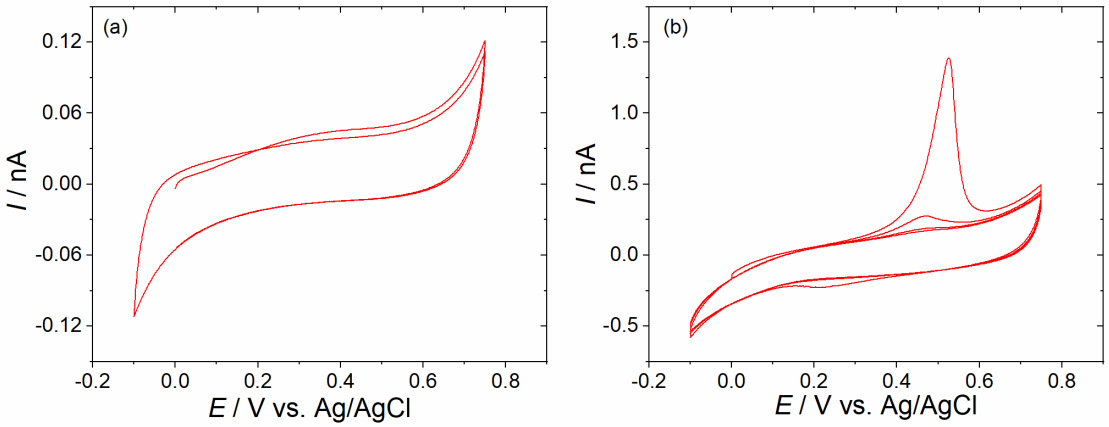

Figure 38: Cyclic voltammetry for commercial Ag NPs (100 nm) in 50mM $NaNO_3$ solution at different immersion times using 2 µm Pt working electrode, Ag/AgCl reference electrode and Pt counter electrode after (a): 1 min, (b): 10 min immersing time.

The experiment was repeated several times and the same result was obtained. If the potential is applied one times directly after finishing the cycles, a cyclic voltammogram similar to. Fig. 38a is obtained. After ten min waiting again a clear oxidation peak could be observed as in Fig. 38b.

The concentration effect on the appearance of the oxidation peak was also observed (Fig. 39). The particles were concentrated ten times compared to the solution that is used in the CV measurement (Fig. 38). At this concentration, the number of the particles was high enough to adsorb at the electrode surface without waiting time. Herein, the experiment was done directly after some seconds that is spent to connect the electrodes with the potentiostat. However, the vanishing of the oxidation peak after the first cycle is an indication that not many particles were accumulated at the electrode surface. The integrated current intensity is proportional to the charge transfer associated with the electrochemical oxidation of Ag NPs.

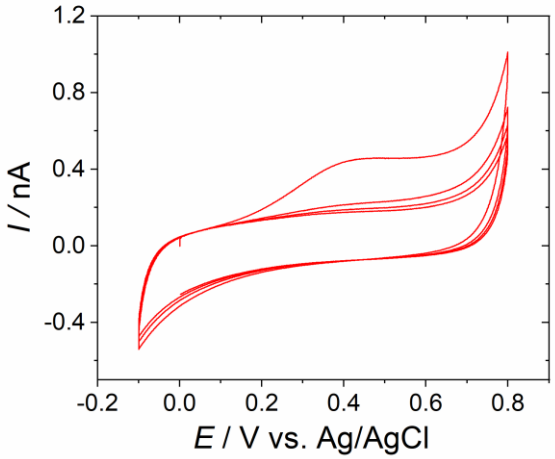

Figure 39: Cyclic voltammetry of commercial Ag NPs in (100 nm) 50mM $NaNO_3$ solution after the solution was concentrated with factor 10 to 1 using 2 µm Pt working electrode, Ag/AgCl reference electrode and Pt counter electrode.

Synthesized Ag-Au NPs: CV for synthesized Ag was done at the same condictions that are used in case of commercial ones. In this CV no any peak could be seen due to the low level of current. So, a sheet of Pt electrode was used as a working electrode to see the reaction events for synthesized Ag at the electrode surface. CVwas recorded at a scan rate of 10 mV s^{-1} in 0.1 M phosphate buffer solution (Fig. 40). Interestingly, a very clear peak emerges at -0.6 V which belongs to the reduction of the negative cytidine ligand. The shoulder that appears at +0.5 V matches the peak that emerged in Fig. 38b. So, this peak may be attributed to the oxidation of Ag atoms, but shows that the Ag atoms to be oxidized are not located in a defined chemical environment.

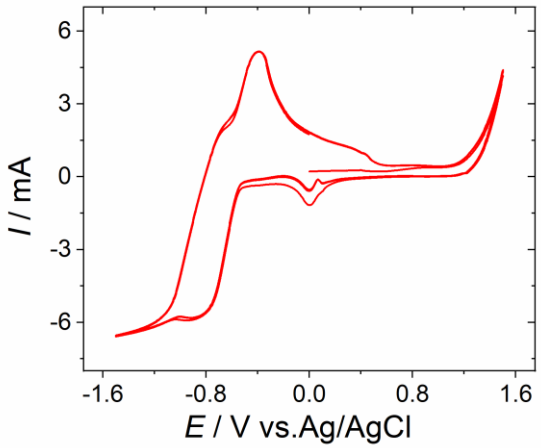

Figure 40: Cyclic voltammetry of synthesized Ag-Au NPs (2 nm) with cytidine ligand in 0.1 M Phosphate buffer solution (scan rate 10 mV s^{-1}, step size 5 mV).

4.2.2 Differential pulse voltammetry

In control experiments in buffer solution without QDs, platinum oxide formation was observed with an associated current that is approximately one order of magnitude smaller compared to the current in QD-containing solution. Additional DPV measurements (Fig. 41) were performed to ensure that the oxidation signal is not caused by other surface reactions. DPV was done at different concentration of selenium to check the effect of selenium concentration on the quality of the particles. The oxidation peak at (+0.6 V) for both DPVs (Fig. 41a,b) were similar to the oxidation value that was obtained from CV. It refers to the oxidation of selenium atoms in the QDs located in different oxidation stages of nanocrystals. The small shoulder near to the oxidation peak as seen in (Fie. 41a) confirms the relation between the concentration of Se and density of trapping state[265]. Electrostatically, a higher percentage of selenium binds with more atoms of cadmium. Because the cadmium ions are presence in the solution as cations ($CdCl_2$), excess of cadmium ions will increase the positive charge on the QDs. Thence the conduction band becomes rich resource of electrons that may be used to fill the trapping states with electrons. The shoulder disappeared (Fig. 41b) when a higher Se amount was used.

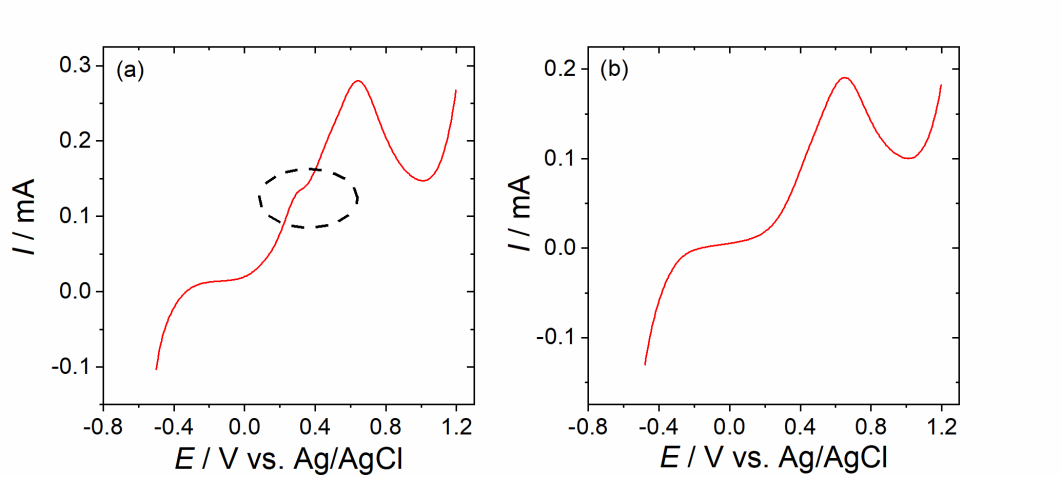

Figure 41: DVP of synthesized CdSe/CdS QDs in 0.1 M phosphate buffer solution. Scan rate 10 mV s^{-1},step size 5 mV and step height 25 mV (a) low percentage of Se (b) higher percentage of Se.

For examining the electrochemical behavior of synthezied Ag-Au NPs, DPV for synthesized Ag NPs was performed in between -0.1 V and 1.0 V. Fig. 42 shows a prominent peak at -0.6 V which matches the reduction peak in Fig. 40. This experiment is nessesary in this case because the prepared solution contains very small quantity of the material (pM concentration).

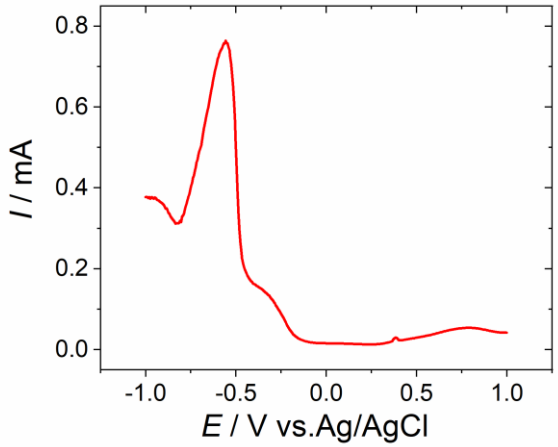

Figure 42: DVP of synthesized Ag NPs in Ag-Au NPs with cytidine ligand in 0.1 M phosphate buffer solution. Scan rate 10 mV s^{-1},step size 5 mV and step height 25 mV.

4.3 Electrochemical signal recording

Chronoamperometry: Trying to record the current–time traces of CdSe QD collision events in phosphate buffer solution at Pt electrode surfaces was done (Fig. 43). It appears that the spikes of the current transient are not high enough to be distinguishable. The disability to record the collision refers to different reasons. The main reason is that the direct observation of QD oxidation in collision experiments requires that the electronic signal generated by one QD exceeds the thermal noise floor.

The thermal noise S_R of electrodes for an electrode radius r = 1 µm and an electrolyte conductivity G = 0.1 mS cm^{-1} can be calculated from Eq. (21). Because the resistivity of the electrode $R_{el} = 1/(4\,r\,G)$, Eq. (21) can be written as:

$$S_R = 16 \cdot r \cdot G \cdot kT =$$

$$= 16 \cdot 1\,\mu m \cdot 0.1\,mScm^{-1} \cdot 1.38 \cdot 10^{-23} JK^{-1} \cdot 298\,K = 5.576 \cdot 10^{-28} A^2 s$$

Because S_R is expressed as charge (Q), the background current can be derived by Eq. (26). For the 100 µs time interval used for the current calculation above, the resulting thermal noise was found to be 5.6 pA.

$$I = \frac{\Delta Q}{\Delta t} \tag{26}$$

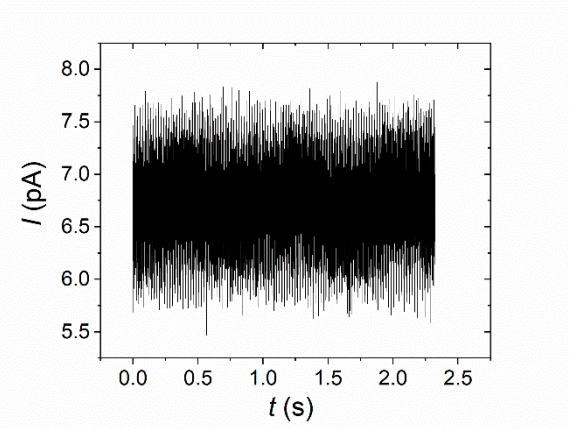

Figure 43: Current−time trace for 2·10^{13} particle of commercial QDs collisions with 1 µm pt electrode. The commercial QDs was dissolved in 10 mL of phosphate buffer solution (pH=7.4). The filtering system was set as 20 kHz. The gain of (50 mV/pA) was used.

A hindered diffusion layer that is formed near the electrode surface within the diffusion layer could be another problem in that case[266]. This layer is close to the adsorbing surface which was predicted from the concentration profile. This layer hinders the flux of particles toward electrodes. So immobilization the particles at the electrode surface maybe helpful.

Accumulation and stripping effect: Cathodic stripping voltammetry is one of the electrochemical techniques that was used to study the electrochemical oxidation of the materials and quantify the particles inside the solution. In this method, the random diffusion which hinders the monitoring of the particles can be avoided and more particles can be accumulated at the electrode surface. Consequently, the electrochemical signal is enhanced, and observable signal can be produced. The particles stick at the electrode surface either electrochemically or chemically at the electrode surface. Ag NPs were accumulated at the electrode surface by applying -0.5 V for different times. Then, the particles at the electrode surface were oxidized at 0.5 V. The integrated current under the curves was directly proportional to the accumulation time (inset of Fig. 44a). The integrated current is an indication how many particles have accumulated at the electrode surface. To ensure that the current change belongs to the oxidation of the particles, the accumulation experiments were repeated for buffer solution. Without particles in the solution, the current was similar at different accumulation times (Fig. 44b). The current in Fig. 44b is higher than the current in Fig. 44a. This is attributed to the larger electrode diameter used to measure the current in absence of QDs compared to that used to mesure the current in the presense of QDs.

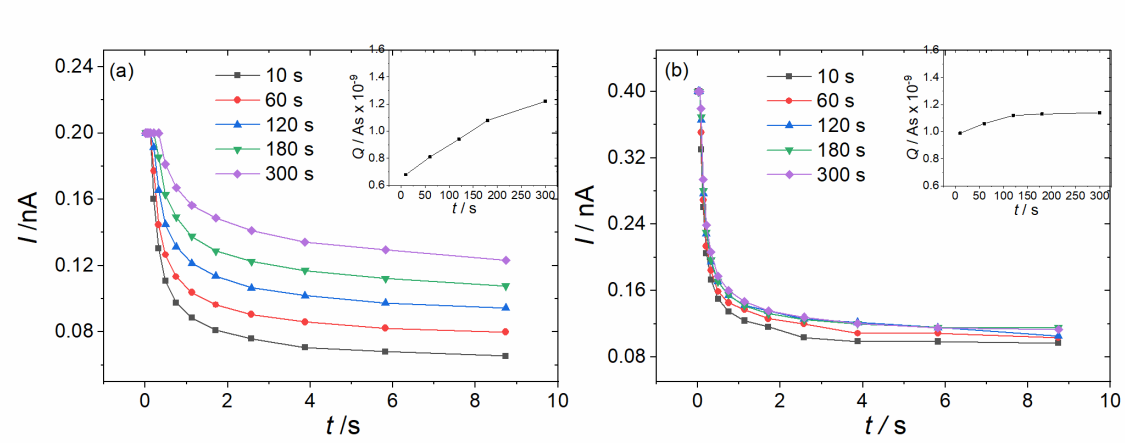

Figure 44: Time effect on the stripping peak currents for (a) Ag NPs (b) Phosphate buffer solutions (pH = 7.4) were done with the NPI potentiostat using platinum working electrode, platinum counter electrode and Ag/AgCl reference electrode. The diameter of the working electrode was 1 µm in case of Ag NPs while 2 µm in case of phosphate buffer solution. -0.5 V was used to accumulate the particles and 0.5 V to oxidize the particles.

Because the disability to collect the spikes for CdSe QDs by chronoamperometry, the stripping experiment was used to avoid the diffusion effect. The CdSe was accumulated by reducing the cadmium atoms at -1.2 V for different times and stripped by oxidation at +0.8 V. As seen in Fig. 45, the current did not change when the stripping time was changed. It could be related to the complete covering of the electrode surface with the particles after 60 s. However, the peak should be increased at 300 s because the electrode was evacuated from some of the particles. The electrode surface was evacuated from the particles by oxidization for 10 s.

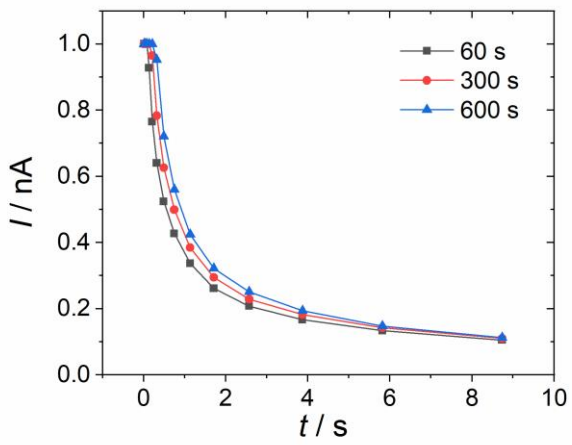

Figure 45: Time effect on the stripping peak current for QD in phosphate buffer (pH = 7.4) was done with the NPI potentiostat using platinum working electrode (3 µm), platinum counter electrode and Ag/AgCl reference electrode. -1.2 is the reduction potential and +0.6 is the oxidation potential.

Expected output current from CdSe QDs and Ag NPs: The current expected from complete oxidation of a single QD can be estimated based on Eq. (27)

$$CdSe + 3H_2O \rightarrow Cd^{2+} + SeO_3^{2-} + 6H^+ + 6e^- \qquad (27)$$

Given a QD radius r = 3 nm and CdSe density ρ = 0.66 g cm^{-3}, the charge Q generated from one QD can be calculated as illustrated in Eq. (28), where (F: Faraday constant, M: molar mass).

$$Q = \frac{24 \cdot \pi \cdot \rho \cdot n \cdot F \cdot r^3}{3 \cdot M} \qquad (28)$$

$$= \frac{24 \cdot \pi \cdot 0.66\ gcm^{-3} \cdot 6 \cdot 96485\ As\ mol^{-1} \cdot (3 \cdot 10^{-9} m)^3}{3 \cdot 191.3\ gmol^{-1}} = 5.9 \cdot 10^{-16}\ As$$

Given a time interval of 100 µs for complete oxidation of a single QD, the resulting current was calculated by Eq. (26) and found to be 5.9 pA

In the same manner, the current output for Ag NPs can be estimated. Each oxidized particle produces one electron Eq. (29)

$$Ag \rightarrow Ag^{+} + e^{-} \quad (29)$$

By applying Eq. (28), the charge Q generated from one Ag particle can be calculated

$$= \frac{24 \cdot \pi \cdot 0.998\ gcm^{-3} \cdot 1 \cdot 96485\ As\ mol^{-1} \cdot (2 \cdot 10^{-9} m)^3}{3 \cdot 107.87\ gmol^{-1}} = 17.9 \cdot 10^{-16}\ As$$

The complete oxidation for one Ag NPs at time interval of 100 µs produces 17.9 pA. Thus, under the best experimental conditions close to the theoretical limit, the current generated from a single QD and Ag NPs is only slightly above the thermal noise level.

4.4 Microelectrode improvements

To check the surface quality of MEs, CV was done by using ferrocene methanol FcMeOH as mediator. The voltammogram (Fig. 46) that is acquired at this electrode behaves sigmoidal at a scan rate of 500 mV/s. There is no flat plateau in the voltammogram, which is attributed to the relatively high scan rate[129]. The CV (Fig. 46) involves the oxidation of FcMeOH without significant contribution from double layer charging current. The very low current at the electrode surface indicates that the true dimension of the electrode in nm scale. However, the current in the voltammogram at 0.5 V is less than the expectation. According to Eq. 19, oxidation of 1 mM FcMeOH at the surface of 2 µm Pt electrode produces current of 60 pA. For some reasons such the surface of the electrode is not well polished or the elerctode has an ohmic contribution due to the bad sealing, the interaction of the redox materials at the electrode surface produces a current less than what is calculated. As a result to that reaching the steady state was very slow. The geometry identification is very important with regard to diffusion constant. So, before studying the steady state for the reaction, the uniformity of the electrode should be accessed. This indicates to the size of the effective area which is the portion of the electrode where the reaction occurs effectively.

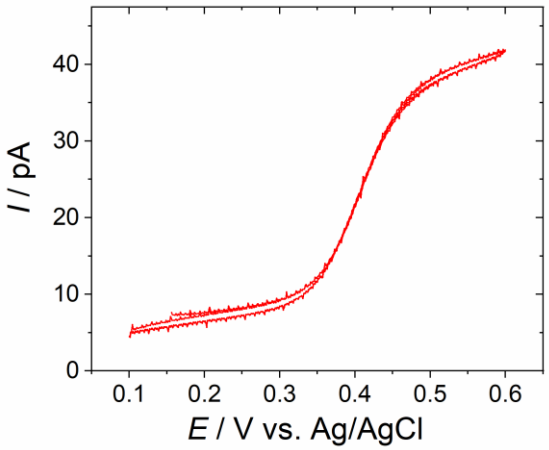

Figure 46: CV of 1 mM FcMeOH in 0.1 M aqueous KNO_3 solution by using 2 µm Pt electrode as working electrode, a Pt wire as auxiliary electrode and Ag/AgCl electrode as reference electrode. Scan rate of 500 mV/s.

At some points, the effective area does not match the geometric area due to the holes and the leakage in addition to the protrusion of the metal outside the glass. So, prior knowledge about the quality of the electrode surface before the electrochemical measurements is required. Confocal laser microscope was used for this task. The diameter was found to be around 2 µm (Fig. 47). The minimum diameter that can be determined by this setup is 0.5 µm because the laser wavelength that used in this setup around 530 nm. The CLSM image shows the leakage in the electrode which finally influences the effective area of the electrode surface. The ratio between the radius of conducting tip and the insulating sheath (RG value) around it should be considered in determining the effective size by cyclic voltammetry. While RG value is essential in most of electrochemical measurements, no exact RG is required in our approach due the limitation of our measurements to very small volume (fL).

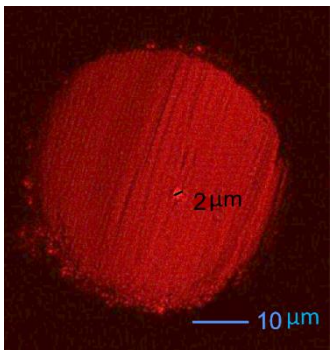

Figure 47: electrode surface imaging done with CLSM.

Rough platinum surface was obtained after depositing Pt-black at the surface of the electrode (Eq. 30). Pt-black was deposited at the electrode surface by reduction of Pt (IV) to metallic Pt.

$$Pt^{IV}Cl_6^{2-} + 4e^- \leftrightarrow Pt + 6Cl^- \quad (30)$$

In addition to the avoiding light reflection on a smooth Pt surface, the electrode impedance will be decrease by depositing Pt black on the Pt disk electrode. As mentioned above, increasing surface to noise ratio is very important demand regarding in analyzing very small entities precisely. One of the important factors that helps in high S/N ratio accomplishment is decreasing the electrode impedance. This factor can be achieved by increasing the surface area. Increasing the roughness of the surface is a desirable alternative for increasing the surface area without changing the geometry.

4.5 Characterizing of CdSe-CdS QDs with single molecule fluorescence spectroscopy

4.5.1 FCS measurements at different *z* axis distances of the confocal volume

The observation volume of the confocal setup is represented by an ellipsoid with Gaussian intensity distribution and short axes in *x* and *y* direction and long axis in *z* direction as depicted in Fig. 12. The horizontal axes (*x*, *y*) depend on the laser power and numerical aperture (N_A) for the objective (Eq. 13). At fixed excitation power and wavelength, the effect of the *z* extension on the size of the confocal volume was checked. *z* extension of the confocal volume depends on depth of focus in the sample solution which equals the distance between the glass surface and the objective (z_f) as illustrated in Fig. 48. As mentioned above that, FCS is a technique for exploring the kinetic properties of the molecules inside the confocal volume. Therefore, minimising the size of the confocal volume is very essential for getting as few as possible particles inside the confocal volume.

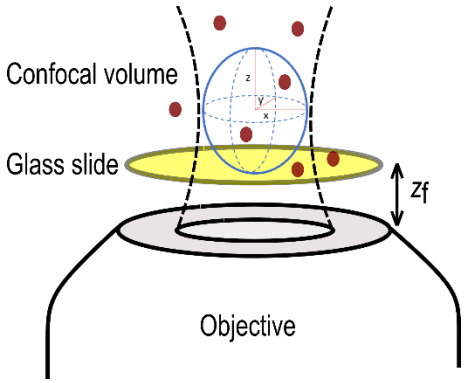

Figure 48 A sketch of the relation between glass surface an confocal voume. z_f is the distance between the glass surface and the objective.

To check the effect of the *z* position on the correlation function, FCS was done for fluorescein as a reference at different z_f in the sample solution. Fig. 49 shows the change in the correlation corresponds to the z_f . The amplitude of the correlation increased when the z_f distance was minimised, whereby the confocal volume was decreased. The focus enters firstly the glass surface then the interface between the cover slide and the solution. The focus must be not in the glass surface, to avoid the Raman scattering effect of the glass which influences the correlation function. Based on Eq. (11) and Fig. 49, one molecule of fluorescein is inside the confocal volume at *z*-axis of 2 µm. When z_f was increased to 10 µm, the number of the molecules was increased to 1.5. Furthermore, the focus must be very close to the glass surface to get very small confocal volume. Consequently, less than one particle can be obtained. This experiment was very essential as a prior knowldege because the electrode must be adjusted in the confocal volume to the z_f position that not more than one particle is existing inside the confocal volume.

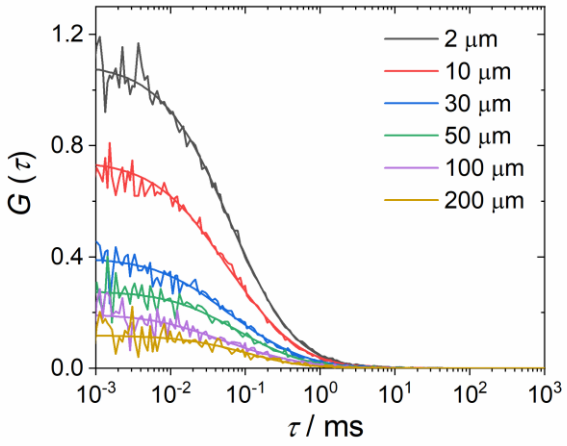

Figure 49: FCS for 0.5 nMfluorescein at different distance between the glass surface and the center of the confocal volume.

4.5.2 Diffusion coefficient for QDs and metallic NPs

Before studying the kinetic events of QDs at the electrode surface, it is essential to identify the behaviour of QDs inside the confocal volume and test the diffusion coefficient (*D*). In order to test the diffusion of QDs, a dye with known diffusion coefficient was used as a reference. Rhodamine B was suggested in the preliminary measurements. It has a high count rate per molecule (high signal to noise ratio) but it was prone to stick to the cover slide surface. This problem was solved by dissolving the rhodamine solution in borate solution (pH 5.5). At this pH, the attractive interaction between the silica material in the cover slide and rhodamine was minimized. For this reason, fluorescein was selected as a reference to measure QDs.

In order to calculate *D* for QDs, the confocal volume was calibrated firstly by fluorescein (with a known $D = 4.2\ 10^{-6}$ cm^2 s^{-1})[244], then the diffusion coefficient of QDs was measured. The correlation function for fluorescein and commercial QDs is displayed in Fig. 50. By fitting the correlation function with burst analyser for fluorescein according to Eq (11), τ_D for fluorescein was obtained. With the known *D* of fluorescein and τ_D of 0.08 ms for QDs which was obtained from fitting the correlation function, the horizontal axis r_x or r_y can be calculated using Eq. (31). The value of $r_{x,y}$ was found to be 0.33 µm, where r_x equals r_y.

$$D = \frac{r_{x,y}^2}{4\tau_D} \tag{31}$$

The correlation fitting provides also the ratio between the radii of the horizontal and vertical axes of the observation volume (ω). From this value, the vertical axis was derived ($r_z = r_{x,y}/\omega$). Confocal volume calibration is very important in case of comparison between two fluoresecence emitters. Because the diffusion time is the time that the molecule needs to leave the confocal volume, the confocal volume should be equal.

At fixed confocal volume with dimension (0.33 µm × 1.32 µm), D for QDs was calculated. To fix the confocal volume at these dimensions, the wavelength and the power of the excitation light was fixed as discussed before in Eq. (13). Moreover, the distance between the focus and the glass surface did not change. Now, the horizontal axis is known (0.33 µm) and the τ_D for QDs was obtained from fitting the correlation function (0.7 ms). By applying Eq. (31), D for QDs was found to be 3.9×10^{-7} cm^2 s^{-1}.

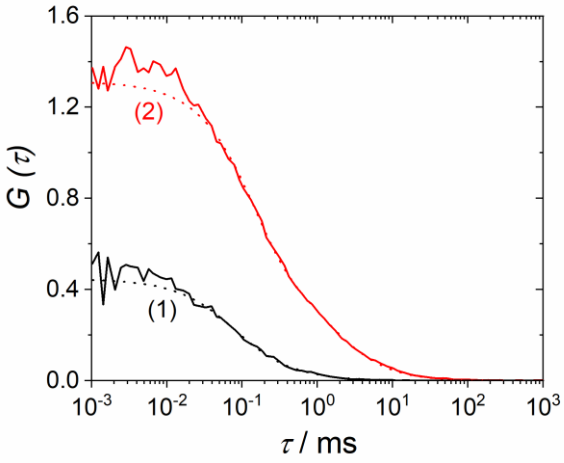

Figure 50: FCS for (1) 0.5 nM fluorescein and (2) very diluted commercial QDs.

In the case of QDs (Fig. 50, curve 2), the correlation curve is broader than for fluorescein (Fig. 50, curve 1). This is caused by the broader size distribution inside the QDs solution. It was approved that QDs are more prone to the agglomeration effect than organic dyes[267]. QDs were dispersed by using horn sonication to avoid the agglomeration effect. When the solution of QDs was used directly without using horn sonicator, the correlation function was wiggled, and the correlation became unstable. Figure 50 also shows that QDs diffuse to the confocal volume slower than fluorescein particles which is expected theoretically because QDs are larger than small organic dyes[268].

In the same way, *D* for Ag NPs was measured. The confocal volume was calibrated by fluorescein. As obvious in Fig. 51, τ_D for Ag NPs is close to τ_D of fluorescein. After the correlation function was fitted according to Eq. (11), τ_D for Ag NPs was obtained (0.07 ms). From the τ_D that was obtained from the correlation function (Fig. 51) and the horizontal axis that was deduced from the reference measurement, the *D* of Ag NPs was calculated by Eq (31). It was found to be 3.9×10^{-10} m^2 s^{-1}.

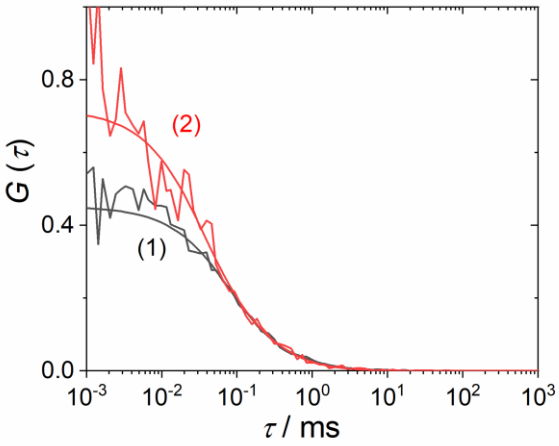

Figure 51: FCS measurement for fluorescein (1) and synthesized Ag NPs (2).

4.5.3 The effect of the laser power on QDs inside the confocal volume

As known, dark states are altered by photophysical or (electro)chemical reactions (represented by the *T* term in Eq. (11))[50]. To examine the photophysical effect, blinking characteristics of the commercial CdSe/CdS QDs were investigated by varying the excitation power of the laser source (Fig. 52). No deviation was found at excitation powers up to 500 µW as expected from literatures[269]. τ_D is expected to decrease when saturation of dark states becomes effective[270]. As seen from Fig. 52, τ_D for commercial QDs is very similar at different power. This means that there is no effective dark state population in the commercial QDs, even if there is dark state population possible. At excitation powers above 500 µW, a slight increase of dark state yield was observed.

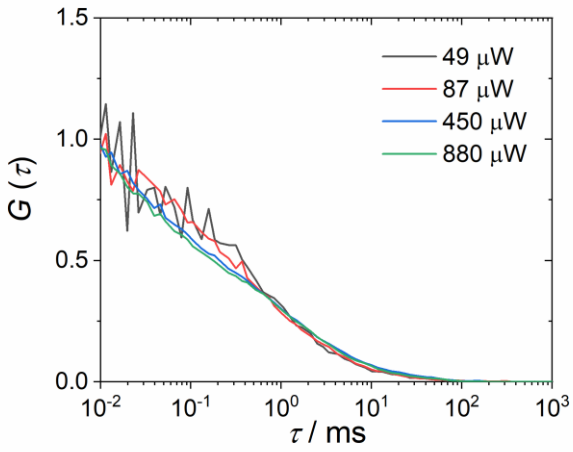

Figure 52: Normalized correlation functions of commercial CdSe/CdS QDs in 0.1 M phosphate buffer solutions at excitation powers from 49 to 880 µW.

4.5.4 The relation between the supporting electrode and aggregation effect

Because FCS is a highly sensitive analytical technique for single molecules, aggregation is a very critical process. Thus, the aggregation can be analyzed quantitatively by measuring the number of the particles inside the confocal volume[271]. More significantly, a change of τ_D is a clear indication for the aggregation effect where the aggregated particles behave as a large particle. From the basics of FCS[50], small particles leave the confocal volume faster than the large particles. FCS for QDs was done at different concentrations of buffer solution to define the smallest buffer concentration that can be used before the aggregation starts and define the tendency to aggregation or adsorption upon discharging. QDs used in our experiments start to aggregate or adsorb on the surfaces when the buffer concentration is below 0.01 M as obvious in Fig. 53. For this reason, QD samples were carboxylate-capped and dissolved in a 0.1 M phosphate buffer solution (pH 7.4) in order to maintain a negative surface charge by deprotonation of the carboxylate groups. Furthermore, before each measurement the suspension was sonicated with a horn sonicator for 30 min to avoid aggregation.

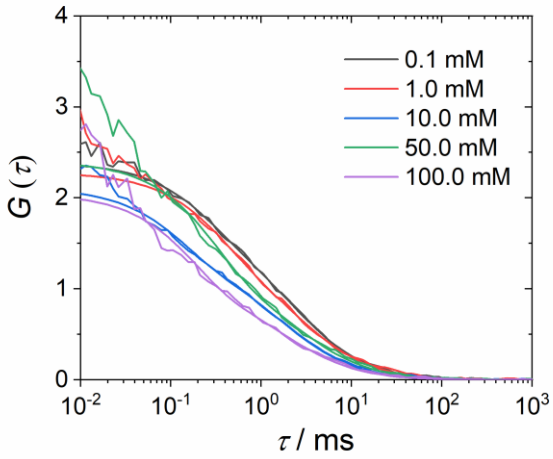

Figure 53: FCS of commercial QDs at different concentrations of phosphate buffer.

4.6 Electrochemistry of QDs and Ag NPs studied by single molecule fluorescence spectroscopy

4.6.1 FCS of QDs at Pt microelectrode at open circuit potential

As discussed above, the observation volume can be considered as a Gaussian-shaped ellipsoid with the long axis oriented in *z* direction and short axis oriented in *x*,*y* direction. To study electrochemical events at the electrode surface inside the confocal volume (Fig. 54), the *z* direction of the observation volume was set as parallel to the optical axis and perpendicular to the ME surface while *x*,*y* axis was oriented as perpendicular to the optical axis and parallel to the ME surface. Basically, small confocal volume produces high signal to noise ratio in the correlation function (higher correlation amplitude). Because the confocal volume is the interesting area in FCS measurements and the electrode surface is the substrate where the kinetics events of the particles occurs, the electrode surface should be as close to the confocal volume as possible and the diameter of the electrode should match the confocal volume.

Concerning the behaviour of the particles inside the confocal volume in the presence of the electrode, two cases was considered: (*i*) If the electrode is not close to the observation volume (distance > 3 µm; Fig. 54a), QDs enter and leave the confocal volume in six independent directions (±*x*, ±*y*, ±*z*) and the size of the confocal volume will not change if the *z*-position of the confocal volume is further increased. (*ii*) If the observation volume is intersected by the electrode surface, the observation volume will decrease and the particle cannot leave the confocal volume in the electrode direction (+*z*) (Fig. 54b). Because the

particles move inside the confocal volume by uncontrolled Brownian motion[112], the blocking effect of the electrode in (+z) direction was taken into consideration.

For QDs leaving the observation volume, τ_D is defined not only by the size of the observation volume but also by the degree of freedom for translational movement. When the confocal volume is intersected by the electrode, the confocal volume is reduced. Thereby, the average τ_D of QDs in the observation volume should decrease when taking into account a constant D. Indeed, an opposite effect could be happened due to decrease of the degree of freedom. Blocking spatial dimension of the observation volume in +z direction by the electrode, decreases the degree of freedom by 1 (Fig. 54b). Because of the degree of freedom and the size of the confocal volume are two contradictory factors, a change of τ_D is difficult to observe experimentally.

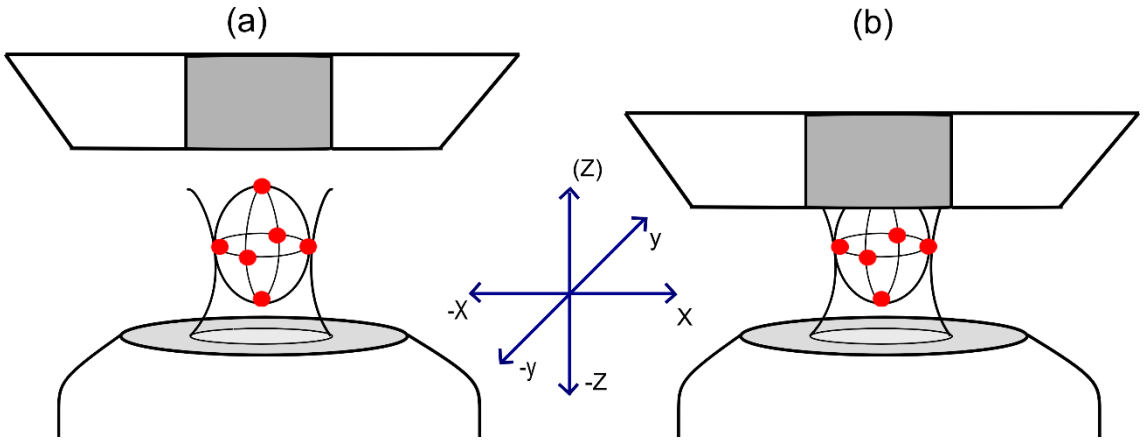

Figure 54: Behaviour of the QDs inside the observation volume (a) in the absence of the Pt ME and (b) presence of the Pt ME.

FCS measurements were performed first at open circuit potential (OCP) of the ME to check the aggregation and unspecific adsorption of QDs on the metallic surface. For these experiments, the correlation function was measured at different distances d between the focal plane and the ME surface. The correlation amplitude $G(\tau \rightarrow 0)$ was expected to increase for $d_{ME\text{-}CV} < z_0$ because the ME surface intersects the observation volume and number of particles inside the confocal volume decreases. As displayed in Fig. 55a, the cross correlation amplitude for CdSe/CdS QDs at $d_{ME\text{-}CV}$ = 4 µm was decreased by a factor of approximately 2 compared to the cross correlation amplitude at $d_{ME\text{-}CV}$ = 1 µm. The decrease of the correlation amplitude

could be attributed to the QD adsorption or aggregation processes. However, the aggregation effect can be excluded because the correlation amplitude for the same solution increased again when the electrode was returned to $d_{ME\text{-}CV}$ = 4 µm. The increase of <*N*> in the observation volume might be caused by adsorption of QDs to the electrode surface also. However, an additional time component for $G(\tau)$ between 10 and 1000 ms is not present in Fig. 55a. It would indicate a prolonged residence time of QDs in the observation volume due to adsorption processes.

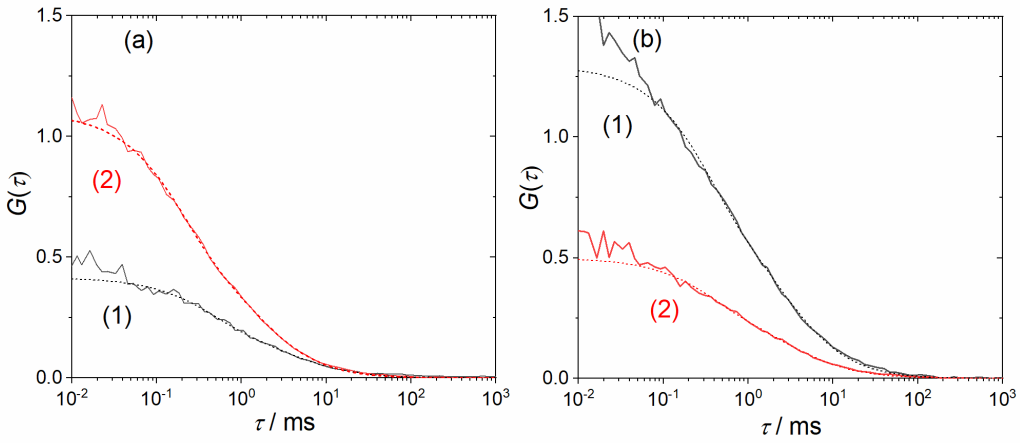

Figure 55: FCS measurements for CdSe/CdS QDs in phosphate buffer (pH 7.4) excited at 470 nm; a) before deposition, b) after deposition of Pt black on the ME surface. Data shown are $d_{ME\text{-}CV}$ = 1 µm (1) and $d_{ME\text{-}CV}$ = 4 µm (2) between focal plane and electrode surface. Dashed lines denote the best fit of the experimental data to Eq. (11).

On microscopic inspection, the polished surface of the Pt ME was highly reflective (Fig. 56a). The bright area in the middle of the image represents the Pt surface surrounded by the glass sheath (grey). At $d_{ME\text{-}CV}$ < 3 µm, the observation volume is reflected at the Pt ME, which drastically increases the effective observation volume. This makes quantitative measurements very difficult. For this reason, the reflectivity of the ME was decreased by a platinization process. Fig. 56b shows that the electrode surface was converted from reflective surface to black spot with no reflection, scattering or photoluminescence emission. FCS measurements with the platinized MEs (Fig. 55b) exhibit an increased correlation amplitude at $d_{ME\text{-}CV}$ = 1 µm (compared to the measurements at polished Pt MEs). This illustrates that the non-reflecting,

platinized ME has decreased the observation volume effectively by intersecting the observation volume (Fig. 55b). These results prove that QDs residing at the ME surface do not contribute to the optical signal because they are either not adsorbed at all, or if adsorbed, their luminescence emission is completely quenched by the Pt ME.

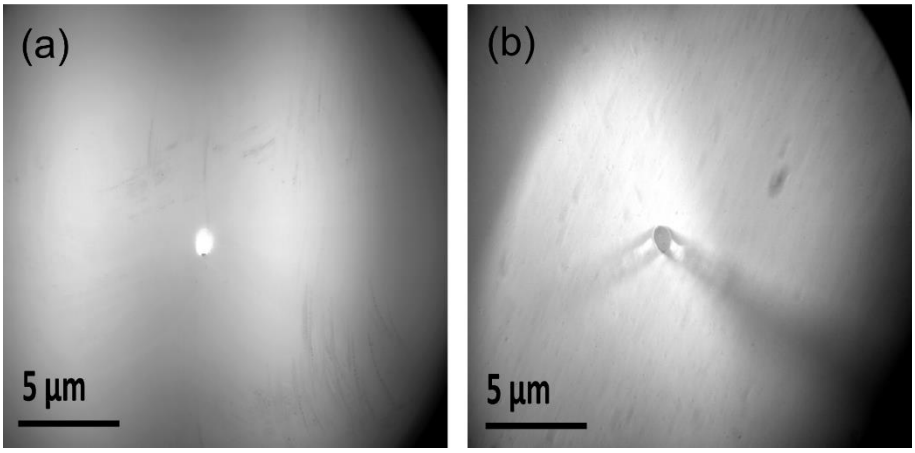

Figure 56: Microscopic images for 1 µm pt electrode; a) before deposition, b) after deposition of Pt black on the ME surface.

4.6.2 Photoluminescence emission decay of QDs under potentiostatically controlled Pt microelectrode

For QDs, fluorescence lifetime τ_F is related to the time that an electron stays in the conduction band before relaxing to the valence band. In the semiconductor material, there are undesirable trapping states slightly underneath the conduction band and above the valence band. τ_F is affected substantially by the density of these states and their location[43]. QDs stay inside the confocal volume in the range of (ms). This time is longer than the residence time in the excited state. For this reason, the excited state lifetime τ_F of the QDs was determined by time resolved fluorescence spectroscopy in the ns range. By this method, the changes in photophysics of QDs are analyzed more precisely[50]. The effect of the potential on the emission decay for commercial QDs (Fig. 57a) and synthesized QDs (Fig. 57b) was studied. The repetition frequency was decreased to 3.9 MHz to detect the full decay and therefore precise information about τ_F could be obtained. The multi-exponential decay as displayed in Fig. 57 is related either to presence of different emitting photon modes[46,272] or the heterogeneity of QDs[273].

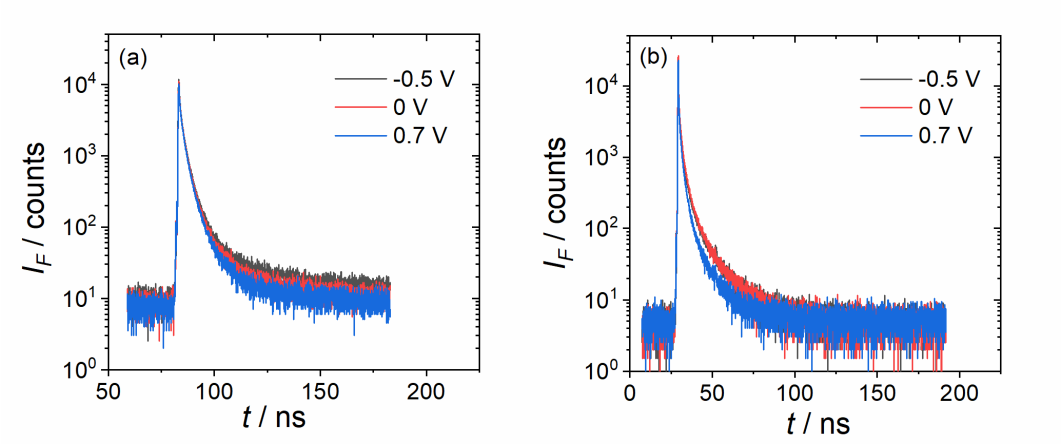

Figure 57: Photoluminescence decay functions of (a) synthesized QDs and (b) commercial QDs in 0.1 M buffer solution at different potentials.

Because of the typicality of this phenomena in QDs, the decay functions were fitted using a three-component exponential model ($I_F(t) = \Sigma[a_i \cdot \exp(\tau_i \cdot t)]$; i = 1-3). The influence of oxidation potential on the decay behaviour was studied and compared for potentials lower and higher than the oxidation potential.

If the first (τ_1) and the second (τ_2) component were fixed, it was be possible to see the difference of the third (τ_3) component at different potentials. The obtained fitting parameters for experimental decay curves at -0.5 V, 0.0 V and +0.7 V for both synthesized and commercial QDs are summarized in Tab. (2). It was found that τ_F of the commercial QDs is smaller than synthesized QDs. This result was expected because small QDs are more prone to the external effect. So, density of trapping states in small QDs increases which enforces depopulation of the excited state. Furthermore, they are influenced by the confinement more and consequently the oscillator strength of the exciton becomes higher which inversely proportional to the lifetime. τ_F was dropped slightly at E = +0.7 V compared to 0.0 V for both commercial and synthesized QDs. Exact quantitative analysis for these results is difficult because the observation volume not only contains QDs which have just entered the observation volume from the surrounding bulk solution but also QDs which are desorbed from the ME surface. However, the reduction of τ_3 suggests that the τ_F of QDs leaving the ME surface is shorter compared to an ensemble of completely fresh QDs. This indicates that QDs, which are oxidized at the ME surface, exhibit a slightly higher trapping site density than the original QDs. The

slightly reduction of τ_F indicates that the particles are still fluorescent, although they are electrochemically modified.

It is obvious also that the decline of τ_3 in case of commercial QDs was smaller than the decline of τ_3 for synthesized NPs. This is related to the electrochemical modification of the particles. Regenerating the trapping state in case of commercial NPs is much more difficult because it was protected with a thicker shell (relatively pure QDs). It is clear from the lifetime at +0.7 V that the particles still live after short chemical modification and leave the electrode surface. However, the slightly dropping in the τ_F for both types are an obvious evidence for partial oxidation of QDs.

Table 2: Lifetime components for emission decays for commercial and synthesized QDs measured at potentials -0.5, 0.0 and +0.7 V vs. Ag/AgCl.

Lifetime component	Commercial QDs			synthesized QDs		
	-0.5 V	0 V	0.7 V	-0.5 V	0 V	0.7 V
τ_1	0.3 ns	0.3 ns	0.3 ns	0.4 ns	0.4 ns	0.4 ns
τ_2	1.3 ns	1.3 ns	1.3 ns	2.2 ns	2.2 ns	2.2 ns
τ_3	6.9 ns	6.8 ns	5.1 ns	13.2 ns	10.5 ns	7.5 ns

From Fig. 57 and Tab (2) no significant difference exists between τ_F of commercial QDs at 0.0 V and -0.5 V compared to the synthesized QDs. This is attributed to the presence of enough dark states in synthesized QDs compared to pure commercial QDs. These dark states can be filled with electrons if external charges are available. The requirements to the negative charge depend on the density of dark state inside the core. However, τ_F was increased at -0.5 V for both types of QDs which confirms the interpretation of filling of trapping states with electrons[42] as illustrated in Fig. 58a. At negative potential below than the reduction potential, the trapping states are filled by the charges that are gained from the electrode. The occupied trapping states promote the charges in the conduction band to stay longer with higher τ_F. In contrast to that at positive potential below than the oxidation potential (Fig. 58b), the trapping states are deactivated. So the electrons in the conduction state do not recombine with the hole in the valence band but relaxe through the trapping states. Consequently, the τ_F decreases slightly.

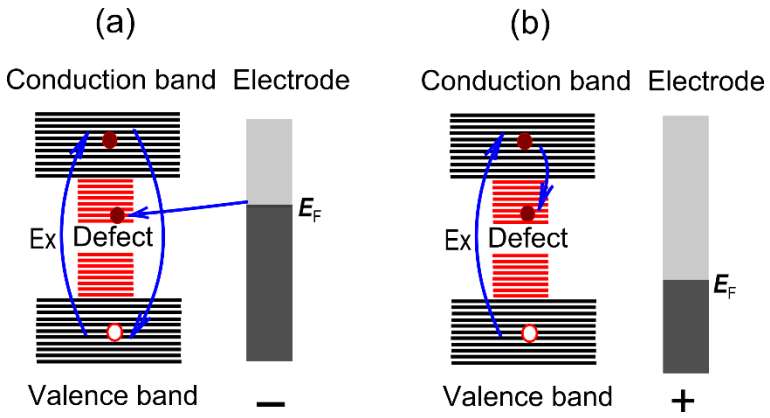

Figure 58: Mechanism of (a) filling the tapping state with electron and (b) deactivation of trapping state.

4.6.3 FCS of QDs under potentiostatically controlled Pt microelectrode

FCS measurements under potentiostatic control were carried out for commercial and synthesized CdSe-CdS QDs. Potentials *E* between 0 and +1.0 V vs. Ag/AgCl were applied. The confocal volume was placed at d = 1 µm from the platinized Pt ME surface. This potential window (i.e. the stability window of water) comprises the potential region in which the oxidative extraction of electrons from the valence band is possible (+0.6 V vs. Ag/AgCl) as discussed before in cyclic voltammetry and differential pulse voltammetry. In addition to that, FCS was performed at open circuit potential (OCP), where no current flows between QDs and the electrode (-0.3 V vs. Ag/AgCl). The recorded FCS data were fitted to Eq. (11) for obtaining $\langle N \rangle$ and τ_D (Fig. 59).

From the preliminary view, commercial QDs (Fig. 59a) were found to have a higher τ_D than synthesized type (Fig. 59b) matching the principle of FCS[241]. It says that the particles with larger hydrodynamic radius (core size with modification ligand and solvation shell) diffuse into the confocal volume slower than smaller one. Commercial QDs have larger hydrodynamic radius due to their considerably larger core diameter (6 nm for commercial QDs vs. 3–4 nm for synthesized QDs (TEM)).

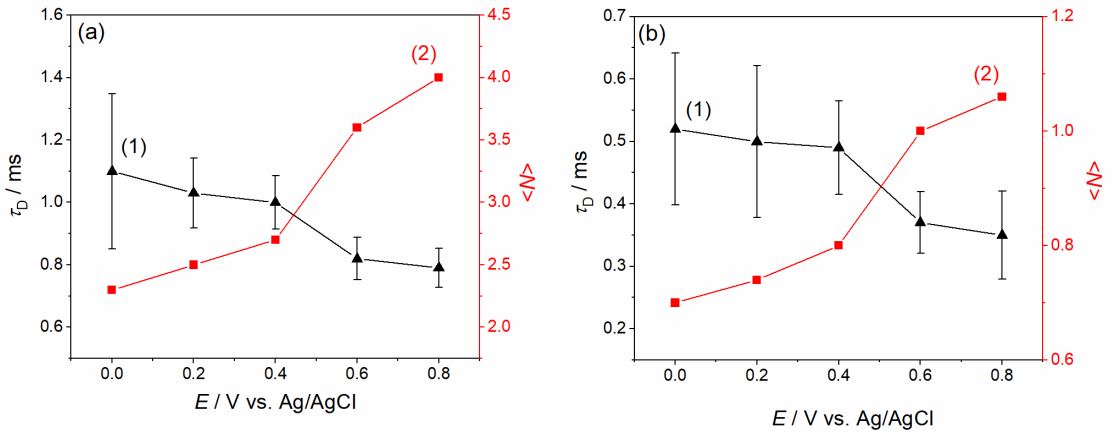

Figure 59: Derived τ_D (1) and <*N*> (2) of QDs at different potentials from the fitting of FCS data according to Eq. (11); (a) commercial QDs, (b) synthesized QDs. Errors for <*N*> are not shown as particle densities vary between different measurements.

It is obvious that τ_D of commercial QDs (Fig. 59a), decreases from values slightly above 1 ms at OCP (-0.3 V vs. Ag/AgCl) to 0.8 ms at E = +0.6 V vs Ag/AgCl (the oxidation potential) and drops from 0.5 ms at OCP to around 0.35 ms at E = +0.6 V in case of synthesized QDs (Fig. 59b). For both types of QDs, τ_D was reduced by the same factor of approximately 1.3 at E > +0.6 V compared to that at OCP. So far, the changes in τ_D are independent of the ligand shell of the QDs. The specific adsorption processes of QDs at the surface of the Pt ME can be excluded.

The oxidative quenching of QDs at the ME surface could be another argument to explain the similarities in τ_D dropping factor for both types of QDs at E > +0.6 V vs. Ag/AgCl. τ_D changes can be related to the electrochemical modification of the core (valence and conduction band) as long as the defect in the material is not existing or the localization of the defect is not close to the electrode[258]. This is explained according to the Fermi potential position relative to the conduction band and valance band in the CdSe QD core as depicted in Fig. 60. The QDs used in this investigation are negatively charged as a result of their deprotonated carboxylate capping groups. The surface of the Pt electrode is also negatively charged due to the affinity of the phosphate ions to adsorb at the Pt surface. This leads to a repulsion between the negatively charged QDs and the Pt ME surface. When the potential is applied to value below the oxidation potential, the Fermi potential of the electrode goes above the valence band and underneath the conduction band. Thereby, the electrode extracts electrons from the conduction band of the QDs. So, the emission of QDs in contact to the ME surface is quenched by electron transfer

and subsequent back transfer to the QD valence band (Fig. 60a). This mechanism was described in literature, where filling of the valence band hole by hole scavengers instead of back transfer is used for the generation of photocurrent[43,84,85,259,274]. Due to the repulsion effect, this mechanism is not very effective in our experiments where the particles stay on the surface of quencher (the electrode) for short time. Moreover, it is known for us from cyclic voltammetry that QDs are oxidized irreversibly at the electrode surface. So it is likely that extraction of the electrons from the valance band has happened as clarified in Fig. 60b.

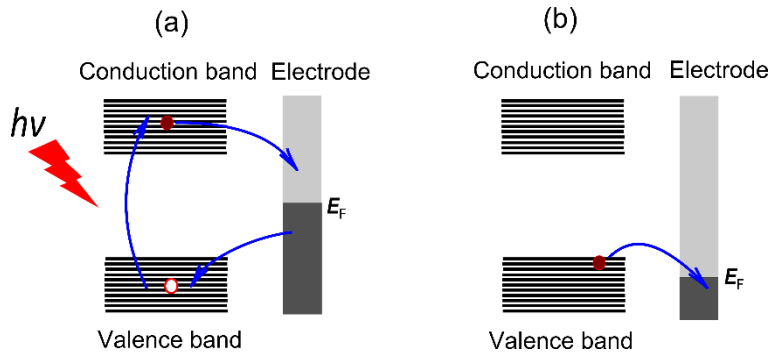

Figure 60: Band structure of QDs at a Pt surface at a) E < +0.6 V vs. Ag/AgCl and b) E > +0.6 V.

At potentials exceeding +0.6 V vs. Ag/AgCl (oxidation potential), the Fermi potential of the electrode drops below the QD valence band and extracts the electrons irreversibly. Deprotonated the anion carboxylate shell on the surface of QDs not only passivates the QDs from outside defection effect, but also boosts the charges inside the core[11,68,75,275]. Consuming the inner charges by oxidation weakens the overall negative charge and the particles adsorb to the electrode surface where they are effectively quenched by electron transfer. Due to the tendency for adsorption or aggregation upon the discharge of QDs, adjust pH to 7.4 and the concentration of supporting electrolyte to 0.1 M is very important (4.5.4).

As mentioned before, entering and leaving the confocal volume is one of the reasons that causes the fluctuations in fluorescence[50,110]. Because the adsorption of the particles at the electrode behaves the same as if the particles leave the confocal volume, the electrochemical modification was considered as diffusion effect in principle In section (4.6.1), the effect of the electrode in (z) direction on the degree of freedom was discussed in detail. It was supposed that the direction (z) was blocked by the electrode surface at potential below the oxidation potential (Fig. 61a). After applying enough potential to the electrode that is adequate to oxidize QDs at

the metal surface, leaving the confocal volume in the electrode direction becomes possible (Fig. 61b) and the degree of freedom increases from five to six. Increase the probability of a QD leaving the observation volume by 6/5 = 1.2, resulting in a decrease of τ_D by that factor. This factor that is expected from statistical considerations matches the experimentally observed reduction of τ_D by a factor of 1.3 within uncertainty margins.

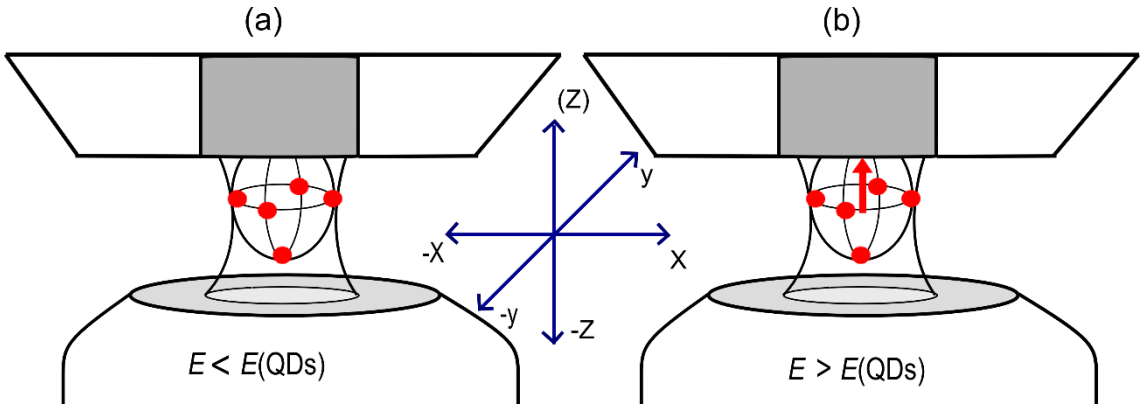

Figure 61: Behaviour of the QDs inside the observation volume in the presence of the Pt ME at potentials E below (a) and above (b) the redox potential E(QDs) of the QDs.

In view of the quite good agreement between the experimental and expected reduction factor of 1.2 for τ_D, they are not likely to play a major role. Otherwise, a much larger reduction factor should result. In principle, the existance of charged QDs in the electric field near the ME is an argument that migration effect could happen. Indisputably, this effect did not happen where τ_D was jumped to lower values at potential > +0.6 V. Migration should cause a steady change of τ_D as a function of *E*. The decrease of the diffusion time in both results at potential > +0.6 V confirms the absence of an active transport mechanism. However, higher supporting electrolyte (0.1 M) was used to suppress the migration effect. At this concentration, the ionic charge is mainly transported by the electrolyte ions. It is not possible to cancel the migration effect totally where τ_D was dropped slightly. Moreover, minimizing the repulsion between the particles and electrode keeps particles in the electric field of the ME. The change in the hydrodynamic QD size (change of core size and/or modification to ligand and thus solvation shell) could modify the diffusion coefficient and thus τ_D. Because τ_D of synthesized and commercial QDs in Fig. 59 was changed by the same factor, the alteration of the solvation shell is unlikely. The diameter of the commercial QDs is approximately two times larger than that of the synthesized QDs, therefore changes in the solvation shell are expected to have less impact on τ_D of the

commercial QDs. Here, both types of QDs were capped with the same capping agent (carboxylate group), so the mechanism of size changes is expected not to be different. A size decrease or other modification of the QDs core itself by an extent that would decrease the hydrodynamic radius sufficiently to reduce τ_D by a factor of 1.2, would certainly change the photoluminescence emission properties of the QDs considerably (e.g. much shorter emission wavelengths or changed emission lifetimes (τ_F) or even suppress it all together. However, only a minor change in τ_F was observed (4.6.3). The minor effect of the blinking and the saturation on τ_D confirms that no significant change of the optical properties was observed (4.5.3).

It is obvious in Fig. 59, that there are two different relation of $<N>$ as a function of E, (*i*) $<N>$ was increased dramatically at +0.6 V and (*ii*) steady state increase at other potentials vs. Ag/AgCl. At sequence of potential applied, it seems to be steady state increase of $<N>$. However, mechanical instabilities of the setup or the alternation of the distance between the electrode and the surface of the electrode are reasons for that. It could that the the distance between the electrode and the focus decreases by thermal expansion after 10 min exposure of the electrode surface to the laser. If the $<N>$ value of steady state is deducted from the value at +0.6 V in Fig. 59, the increasing value of $<N>$ by a factor of 1.2 will be clear and corresponds to the previous results. To check the instability effect, the measurement was done separately at potential < +0.6 V by re-adjusting the electrode after each measurement. It was found that the average fluorescence intensity remained always constant. At potential > +0.6 V, the intensity was apparently dropped due to increase of $<N>$. In order to exclude the instability effect and to ensure the effect of oxidation potential, the measurement was run at 0.0 V, then set at +0.8 V and again to 0.0 V. The time of the measurements was reduced to 5 min as well. All these precautions were established to minimise the instability of the setup and electrode position. $<N>$ and τ_D were identical for both measurements at 0.0 V. At +0.8 V, $<N>$ was increased and τ_D was dropped by factor 1.3 as expected in Fig. 61. After the instability effect was considered, no deviation of $<N>$ from the bulk value at E < +0.6 V was found because the number of particles entering the confocal volume equals the leaving particles ($dN_{in}/dt = dN_{out}/dt$) if no adsorption occurs at the electrode surface. The change of $<N>$ depends on the kinetics of the particles inside the confocal volume, therefore the variation in $<N>$ at potentials > +0.6 V can be explained by the rate. Beside the entering and leaving the confocal volume, all the kinetics events that might be expected like adsorption, desorption and oxidation were considered (Fig. 3).

At the steady-state, which is established at a constant potential and constant fluorescence intensity, the number of detectable particles in the observation volume is determined by Eq. (32).

$$< N > = < N >_0 + \frac{dN_{in}}{dt} + \frac{dN_{des}}{dt} - \frac{dN_{out}}{dt} - \frac{dN_{ad}}{dt} - \frac{dN_{ox}}{dt} \quad (32)$$

Here dN_{in}/dt is number of particles entering the observation volume in a time interval dt, dN_{des}/dt is the number of particles being desorbed from the surface, dN_{out}/dt is number of particles leaving the observation volume by diffusion, dN_{ad}/dt is number of particles being adsorbed and dN_{ox}/dt is number of particles are destroyed by an oxidation process. $<N>_0$ is the number of particles resulting from the bulk concentration of particles and is calculated from $<N>_0 = c_0 \times V_{eff}$, where c_0 is the bulk concentration of particles and V_{eff} is the effective observation volume. It must be noted that for single molecule conditions, the steady state condition only applies for $dt >> \tau_D$.

At potentials > +0.6 V, the particles start to adsorb at the electrode surface and consequently two kinetics events (desorption and oxidation) follow that during the residence time of the particles at the electrode surface. In this case, there is no steady state anymore and ($dN_{in}/dt \neq dN_{out}/dt$). The cyclic voltammogram in Fig. 37 shows the irreversible oxidation of QD, hence $<N>$ decreases as explained by simulation (4.6.5). $<N>$ was increased in FCS measurements at potentials > +0.6 V. The inconsistency related to $<N>$ have to be matched. It can be interpreted by the retention of QDs at the electrode surface for short time and their partial oxidation[276]. When QDs are oxidized partially, they are desorbed and re-enter the confocal as new particles with maintaining of their fluorescent property.

4.6.4 FCS of Ag NPs under potentiostatically controlled Pt microelectrode

In order to study FCS of Ag NPs (2 nm diameter) capped with a cytidine shell in phosphate buffer solution, potentials E between -0.6 and +0.5 V vs. Ag/AgCl were applied to the platinized Pt ME and the observation volume was placed at d = 1 µm. The potential window was selected to be consistent with the potential scanning in the cyclic voltammetry in Fig. 40. τ_D and $<N>$ were derived from the fitting of FCS data in Fig. 62 to Eq. (11). Interestingly, τ_D was increased dramatically from 0.1 ms to 0.5 ms at E = -0.6 V which matches the appearance of the reduction peak in Fig. 40. This peak is related to the reduction of cytidine ligand shell

which protects the NPs from the aggregation effect. So, the increase of τ_D at E = -0.6 V could be related to the aggregation effect. Figure 62 shows also the apparent decrease of <N> at +0.4 V to 1.2. Half of the particles that are accumulated at the electrode surface were oxidized totally and the rest of particles still live. It can be attributed to the high number of accumulated particles at the electrode surface when negative potential was applied. This interpretation was confirmed by applying positive potential only. In that case, <N> did not change.

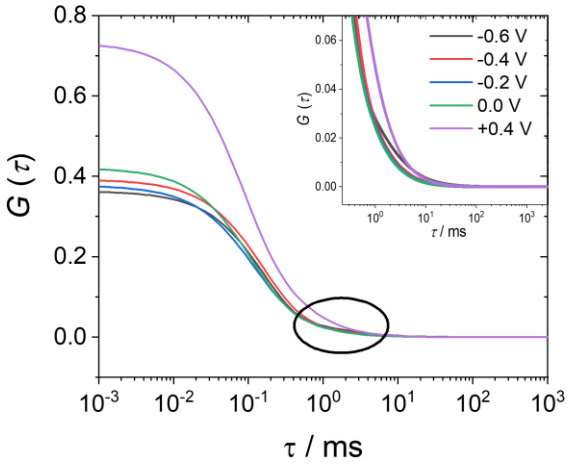

Figure 62: FCS measurements for synthesized Ag NPs at different potentials.

4.6.5 Simulation output

One of the possibilities when the particles enter the confocal volume next to a potentiostatically controlled Pt microelectrode is the complete destruction of the particles. Logically, this impact reduces the number of particles inside the confocal volume. To ensure this expectation, the behaviour of the particles inside the confocal volume was studied preliminary by simulation.

Simple Monte-Carlo simulations of NP diffusion and interaction with the electrode surface were done in a domain depicted in Fig. 63. It contained a confocal volume described as cylinder with radius r_{cv} = 0.5 µm and height $2h_{cv}$ = 3 µm. The center of this cylinder was placed with a distance $d_{ME\text{-}CV}$ = 1 µm above the center of the microdisk electrode with radius r_0 = 0.8 µm. In this case, the ME intersects the confocal volume as in the real experiment. The simulation space was divided into voxels with 0.1 µm length in each direction. In each time step of 1 µs, the particles move independently along the x, y, and z coordinates and increment

their coordinate by one voxel length, decrement it by one voxel length or keep it constant with equal probability. The dimension of the simulation space (x, y, z) was (16 µm, 16 µm, 13 µm). The outer shell of this volume with a thickness 0.4 µm (space between the outer wire frame and the grey box in Fig. 63) was used as 'equilibration domain' to adjust the nanoparticle concentration to the bulk concentration. The simulation was conducted for 5 s (5×10^6-time steps).

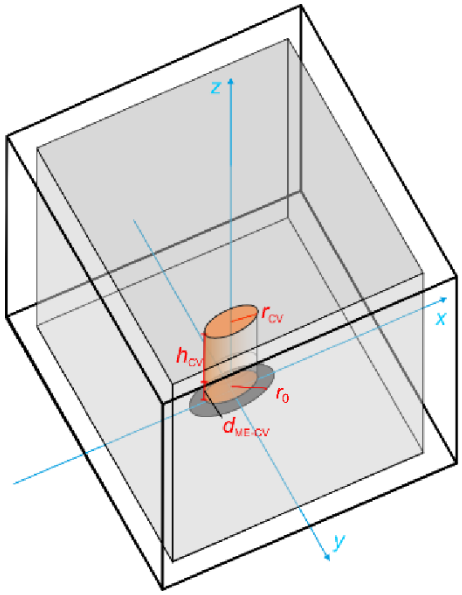

Figure 63: Simulation domain.

The NP density with a bulk concentration of 0.5 nmol L^{-1} (0.3 particles per μm^3) corresponds to 1000 NPs in the simulation domain. They were placed randomly in the domain and then allowed to diffuse with a diffusion coefficient of 3.5×10^{-7} cm^2 s^{-1}. Particles leaving the domain at the side walls were replaced by a particle entering the domain at the opposite wall. After each time step the nanoparticle concentration in the outer shell of the simulation domain was equilibrated with the bulk concentration by removing existing (NPs) or adding particles at random position within the equilibration domain. Particles arriving at the bottom of the simulation domain (corresponding to the Pt ME or glass sheath) were treated as sticking particles with an adsorption constant K_{ad}. This related to a probability of desorption $P_{ox} = (-1) + (K_{ad} + 1)/K_{ad}$ with $K_{ad} \geq 1$. When NPs are attached to the electrode surface, they are destroyed by electro-oxidation with a pre-set probability P_{ox} = [0...1] reflecting the influence of the electrode potential on the oxidation rate. Sticking and desorption form the glass sheath of the

ME were treated analogous to adsorption to the electrode surface but with a different $K_{ad,glass}$ = 1 ($P_{ox,glass}$ = 0) in all cases. After each time step, the number of (NPs) in the confocal volume was counted and displayed in a time series plot.

In the beginning, the adsorption effect was studied in the absence of the destruction effect (Fig. 64a). The average number of adsorbed QDs $<N_{ad}>$ increased with the adsorption constant K_{ad} at the electrode surface (Fig. 64a,). In the model, $<N_{ad}>$ was equilibrated with the bulk concentration of QDs and consequently the average number $<N>$ of QDs in the observation volume did not change with the adsorption constant.

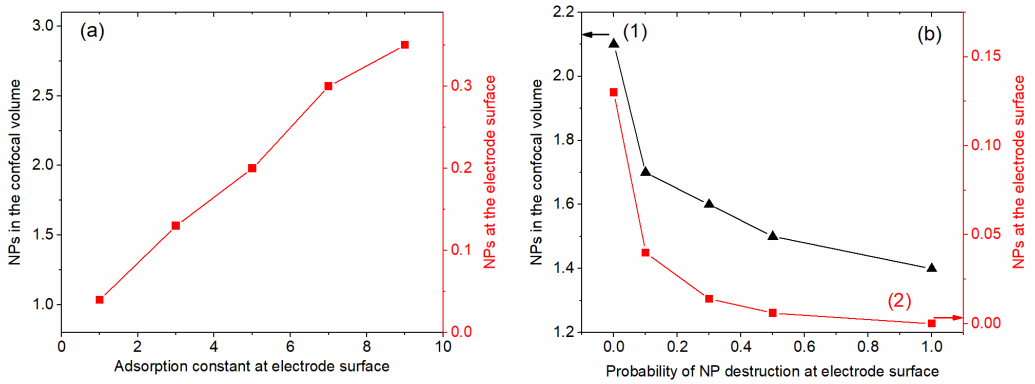

Figure 64: Simulation average particle number in the observation volume and NPs residing at the electrode surface as a function of (a) the adsorption parameter without oxidative destruction of NPs (P_{ox} = 0) and (b) the destruction probability for an adsorption constant at (K_{ad} = 7 (1), K_{ad} = 3 (2)).

When an oxidative destruction of NP at the electrode surface was simulated by setting $P_{ox} > 0$ at fixed values of K_{ad} = 7 (Fig. 64b, curve 1) and K_{ad} = 3 (Fig. 64b, curve 2), the average number $<N>$ of QDs in the observation volume as well as the number of NPs at the electrode surface $<N_{ad}>$ decreased systematically. For P_{ox} = 1 and K_{ad} = 7, $<N>$ reached 1.4 (instead of $<N>$ = 2.1 in the undisturbed case). $<N_{ad}>$ approached zero in this case. Simulations showed us what expected, where $<N>$ decreased by the destruction of the particles at the electrode surface.

4.7 Studying the interaction of redoxactive species at the electrode surface by bipolar electrochemistry

4.7.1 Motivation of coupling the bipolar electrochemistry with fluorescence spectroscopy

In the previous chapter, it was proven that the complete oxidation of QDs requires a sequence of oxidation events. However, the number of these sequences could not be determined because the direct single NP collision experiments which produce very low Faradaic current close to background current for small NPs and QDs. Although the fluorescence-based readout methods are very sensitive, it was not possible to visualize the events for very small fluorescent NPs (<10 nm) precisely by combining the fluorescence techniques with conventional electrochemistry. In addition to that, the methods used in the previous chapter were restricted to the luminescent particles.

Herein, the conventional electrochemistry was replaced by bipolar electrochemistry. The interaction of NPs at the electrode surface was studied indirectly via another fluorogenic dye which can produce an observable and sensitive optical readout. The redox species are oxidized on the anodic pole while the fluorgenic molecules are reduced on the cathodic pole as illustrated in Fig. 65. To satisfy this demand, the reporter must be fluorescent in reduced state (i.e the product) and non-emitting in oxidized state (the provided fluorgenic molecule).

When the output charges of the oxidation process are passed through the BE, the fluorogenic molecules are reduced as described in section (2.5.3) and Fig. 65. Consequently, fluorescence output is produced, which can be observed by a confocal laser microscope and detected by a camera focused on the solution directly adjacent to the cathodic pole of the BE. Due to the balance between the cathodic and the anodic current, the modified molecules/particles on the anodic pole are identified by the emerging fluorescence on the other end of the BE. Due to the linearity between the Faradic current response and the fluorescence output[37], the electrochemical current of a fluorogenic redox reaction can be derived from the change in fluorescence intensity. So, the fluorescence was used as alternative mean to measure the current response.

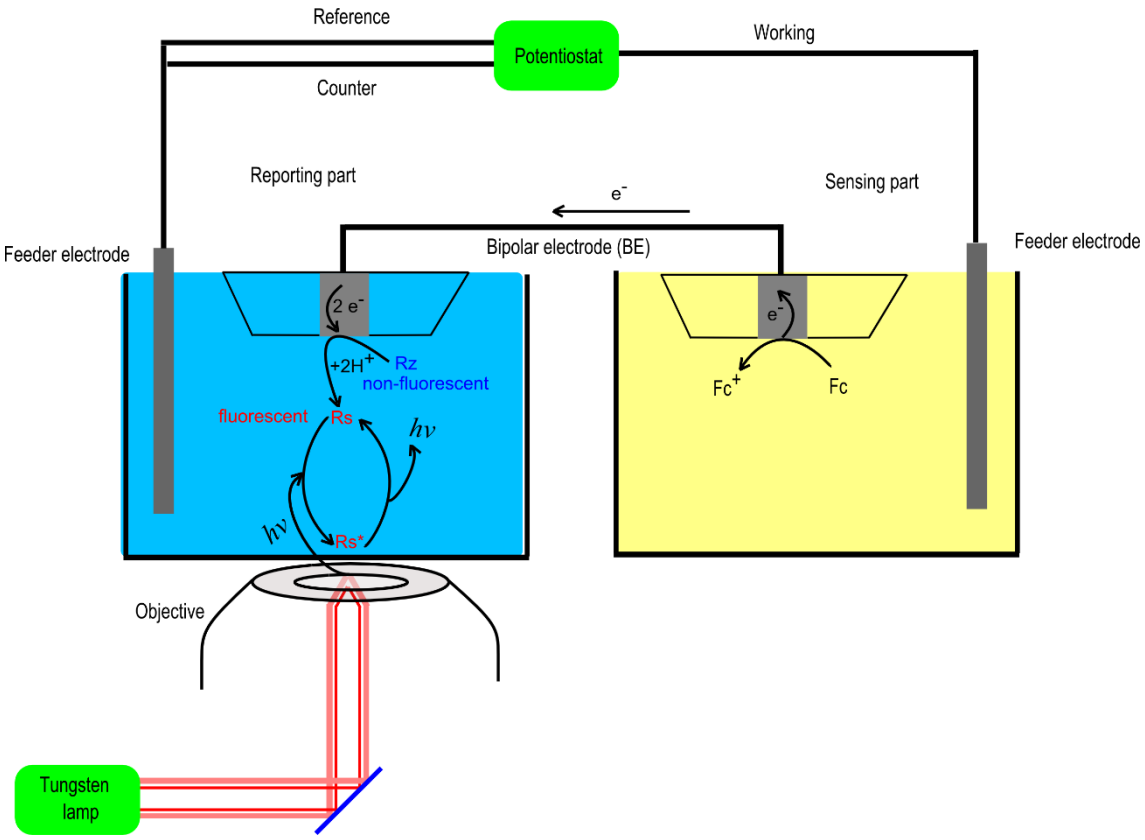

Fig 65: Mechansim of coupling the oxidation of Ferrocene (Fc) in the sensing part with the reduction of resazurin (Rz) in the reporting part.

4.7.2 Observation of the limitating current by cyclic voltammetry

In BPE, the oxidation of the redoxactive species must be balanced with the coupled reduction reaction on the other pole of the BE. So, the limiting current is very important in case of closed configuration BPE. The pole with a smaller limiting current is the limiting pole. It is this pole that determines the voltammetric response. However, one must keep in mind that different electrodes (and electrode processes) might become the limiting pole at different potentials. By selecting appropriate conditions, it must be ensured that the electrochemical conversion of the analyte consitutes the limiting process under all conditions analyzed. Here, the oxidation of FcMeOH on the anodic pole of BE was coupled to the reduction of resazurin on the cathodic pole. Resazurin is a weakly-fluorescent dye and was used as a fluorgenic reporter to indicate the oxidation events on the anodic poles. It is reduced easily to high fluorescent resorufin as seen in Fig. 66. If resazurin is reduced further, a non-fluorescent molecule called dihydroresorufin is produced.

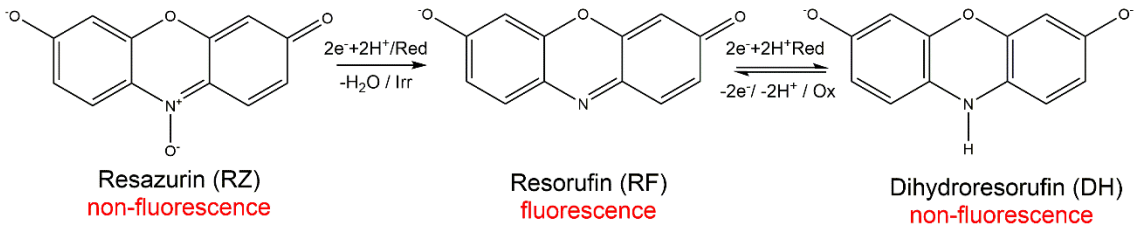

Figure 66: Reduction of weakly-fluorescnt resazurin to strongly fluorescnt resorufin then to non-fluorescnt dihdroresorifin.

FcMeOH was used as a reference electrochemical material because FcMeOH has a well defined reversible electrochemistry and was studied abundantly. Theoretically, the limiting current at the steady state can be calculated according to Eq. (19). At the same conditions, the reduction of resazurin limits the overall *i-v* response of the BPE because resazurin has a lower D (8.5×10^{-7} cm^2 s^{-1})[277] than FcMeOH (7.8×10^{-6} cm^2 s^{-1}). To determine the voltammetric response of the BPE experimentally, CVs were recorded by coupling the reduction of 1 mM resazurin in one cell and the oxidation of 1 mM FcMeOH in another cell in the potentiostatic mode with taken into account that the poles of the BE have similar diameter. The potential was swept towards negative and positive potential limits. Moreover, the efficiency of the BE was checked by this experiment. As displayed in Fig. 67, the CV has a sigmoidal shape, which is similar to the conventional electrochemistry. Fig. 67a shows that the limiting current (0.2 nA) appears in the positive part of the scan when the Pt feeder electrode in FcMeOH solution was set as a working electrode. The reciprocal of the sigmoidal appeared in Fig. 67b when the working electrode was placed in the resazurin solution. In the normal CV of FcMeOH like what was illustrated in Fig. 46, the oxidation peak appeared in the positive part of the scan. Unlike to that, the oxidation peak appeared in the negative part of the scan when the feeder electrode in FcMeOH solution was set as working electrode. The reason for that is the polartity at the pole of BE is opposite to the polarity at the feeder electrode. This means when the potential was swept towards negative potential through the feeder electrode, the potential was swept towards positive potential on the pole of the BE in the same solution. The limiting current in that case is in the negative part of the scan in the CV. In both results, the limiting current belongs to the reduction of resazurin. The pole that is placed in the resazurin solution is the limiting pole and the other is the excess pole. The capacitive current is another thing can be noted in the CV (Fig. 67). The high capacitive current is related to the high scan rate and also could be attributed to the bad sealing of the wire inside the cappillary.

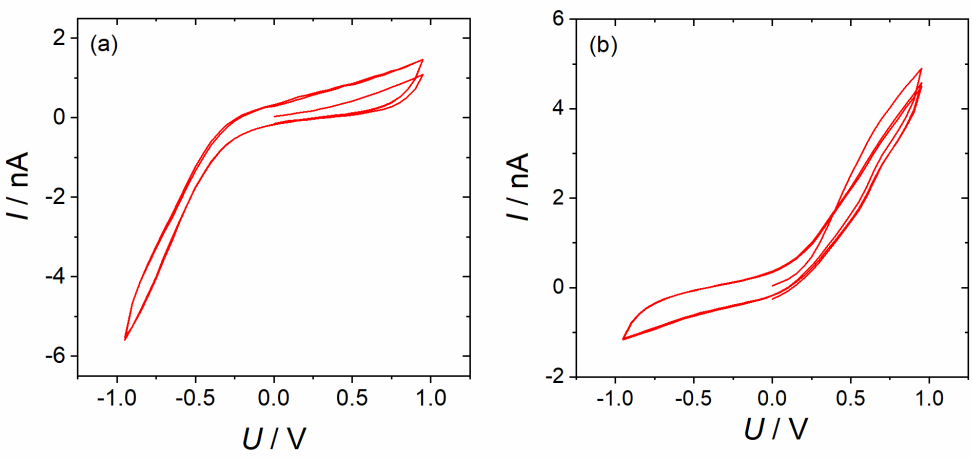

Figure 67: Cyclic voltammetric response of a Pt BE, one pole of a diameter 25 µm immersed in 1 mM FcMeOH diluted in 50 mM KCl electrolyte solution while the other pole of the same diameter was immersed in 1 mM resazurin in 50 mM carbonate buffer (pH 10). Scan rate 0.1 V s^{-1}, the Pt feeder electrode works as a working electrode in the (a) FcMeOH solution, (b) Resazurin solution.

From these perspectives, the upper limit of the oxidation current is restricted by the reaction on the cathodic pole. So, the maximum concentration of FcMeOH that can be detected by resazurin is limited. To make the overall volumetric response not limited by the reaction in the reporting part, the concentration of FcMeOH in the sensing part has to be less than 0.2 mM if 1 mM of resazurin was used in the other part. The limiting current has no consideration when high potential is applied because everything inside the solution even the solvent itself could be oxidized. In case of BPE, high driving force is applied because an additional voltage is required for coupling. Fig. 68 illustrates the effect of the potential window on the limiting current. Fig. 68a shows the oxidation of FcMeOH is the limiting current where the concentration of FcMeOH was less than the concentration of resazurin. When the potential window is increased (+2.0 V to -2.0 V), the oxidation current increased and became close to the reduction current as seen in Fig. 68b. Interestingly, the oxidation current was similar to the reduction current when the potential window was in between +3.0 V and -3.0 V (Fig. 68c). The overall potential was high enough to oxidize the solvent. Consequently, the oxidation of FcMeOH was overlapped with the oxidation of the water.

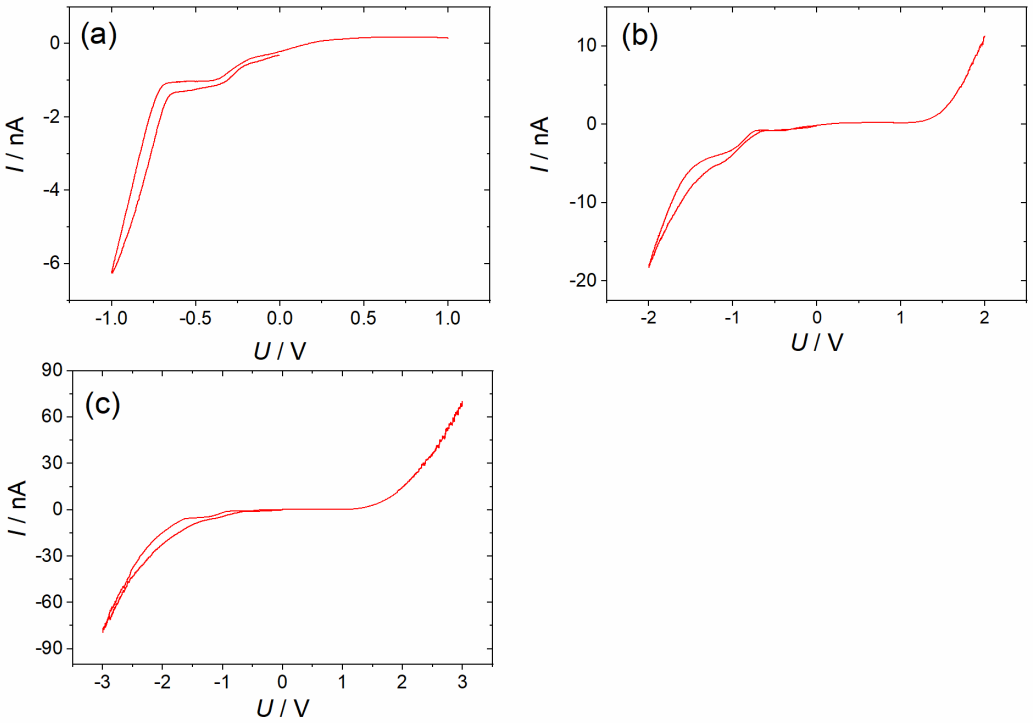

Figure. 68: Coupling the oxidation of 10 µM FcMeOH in 0.1 mM KNO_3 and the reduction of 1 mM resazurin in 0.1 M phosphate buffer solution (pH 7.2); (a) -1.0 V to +1.0 V, (b) -2.0 V to + 2.0 V, (c) -3.0 V to +3.0 V. Scan rate 10 mV s^{-1}, 25 µm of Pt BE was used for coupling.

4.7.3 Determining the detection limit of FcMeOH by using BPE

To study the electrochemical events of NPs at the electrode surface, the fluorescence intensity has to be calibrated with the corresponding charge transfer. Since the charge transfer through the BE is related to the concentration of the analyte, determining the minimum concentration of the analyte is a very important issue especially in case of single molecule detection. To discover the ability of BPE to detect the events for single NPs at the electrode surface, the minimum concentration of the redox species that produces enough charges to reduce the fluorogenic part must be defined. Because FcMeOH has known electrochemical properties, it was used for the calibration purpose. Each oxidized FcMeOH molecule produces one electron (Fig. 65).

To reduce one molecule of resazurin on the cathodic pole, two molecules of FcMeOH must be oxidized on the anodic pole. However, the number of photons that are equivalent to

one electron depends mainly on the quantum yield of the fluorogenic reporter. To study the oxidation events on the anodic pole by the corresponding photon output generated on the cathodic poles, the experiment was set up in a way that the total Faradaic signal is not limited by the resazurin reduction. When resazurin was reduced in a conventional electrochemistry cell, 0.2 mM was the minimum concentration that produces observable luminescence under the microscope control. However, increasing the concentration on the excess pole increases the overall volumetric response[191]. So, 1 mM of resazurin was used in our experiment. The slow voltammetric response is attributed to the additional voltage requirement from the coupling pole. As displayed in the previous section (4.7.2), 0.2 mM is the highest concentration of FcMeOH that can be used to ensure that the pole in FcMeOH solution is the limiting pole if 1 mM of resazurin was used to report the oxidation of FcMeOH.

Figure 69a shows the variation of luminescence response as a function of FcMeOH concentration, while Fig. 69b depicts the image readout. As obvious from the images and the values, there are no significant differences between the luminescence intensity at concentrations ≥ 0.2 mM of FcMeOH which confirms the theoretical calculation regarding the limiting current. This means that the pole in the resazurin solution is the limiting pole if the the limited oxidation current for FcMeOH iat concentrations above 0.2 mM excedes the possible reduction current of 1 mM resazurin.

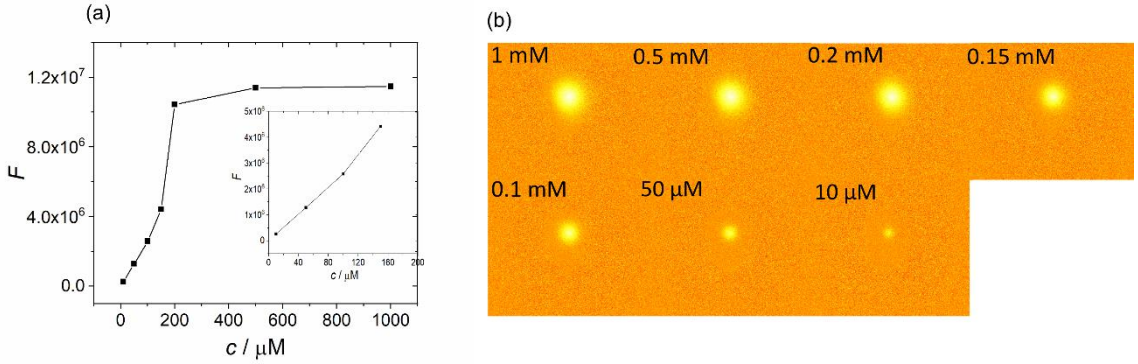

Figure 69: (a) Fluorescence intensity outputs that are produced at the cathodic pole when different concentrations of FcMeOH in 0.1 M KNO_3 solution were oxidized at the anodic pole, (b) images of different concentration response.

According to Eq. (19), the steady state current is proportional to the concentration of the analyte. Moreover, the current also has been proven to be directly proportional to the luminescence intensity as illustratred in Eq. 33[37], where $nF/K \cdot I_{ex}(r) \cdot S(r).\sigma(\lambda) \cdot \varnothing(\lambda)$ is constant.

Consequently, the relation between the concentration of the analyte and the fluorescence was derived.

$$i = \frac{nF}{K \cdot I_{ex}(r) \cdot S(r).\sigma(\lambda) \cdot \emptyset(\lambda)} \frac{dF}{dt} \quad (33)$$

If the oxidation current is the limiting current, the output luminescence on the cathodic pole should be proportional to the concentration of the analyte in the sensing part. This expectation is clear in the inset of Figure 69a where the fluorescence response was directly related to the concentration of the oxidized FcMeOH at concentrations less than 0.2 mM.

In these experiments, 10 µM was the minimum concentration that could be detected. The luminescence intensity was directly proportional to the driving force as illustrated in Fig. 7070. So, at concentration less than µM range an additional driving voltage is required to obtain a clear luminescence on the cathodic pole. However, applying higher driving voltage is very critical where the potential becomes more close to the redox potential of other components such as oxygen or water. So, it was impossible to go down with concentration below < 10 µM. Instead of Pt feeder electrodes, graphite feeder electrodes were used to increase the potential stability window of water and avoid the overlap between the oxidation potential of the analyte and the potential of water splitting. Moreover, the solution was purged and the cell was closed completely to avoid dissolving of the oxygen in the water. However, all of these precautions were useless in case of concentration was below 10 µM. For more precaution, the detection limit of Fc molecule in a highly pure acetonitrile solution was checked. The detection limit of Fc in acetonitrile solution was similar to the detection limit of FcMeOH in the water. At high potential, the potential starts to oxidize everything even if acetonitrile itself can be oxidized. The requirement to high potential is the problematic of BPE where the potential is not applied directly to the working electrode but it is dissipated through the solution.The effect of the potential on the oxidation of 10 µM of FcMeOH was studied by observing the fluorescence output for resazurin on the other pole. A nice correlation was seen between the potential and fluorescence output because more driving force generates more Faradic current (Fig. 70). At 1.2 V, a few molecules of FcMeOH started to oxidize and increased linearly when more driving force was applied. Fig. 70 shows a steady state increase of luminescence at different potentials which can be attributed to the migration effect. However, the molecules mostly move towards the electrode surface under a diffusion control especially at low concentration. The oxidation of water can boost the oxidation of Fc and consequently the corresponding luminescence slightly increase.

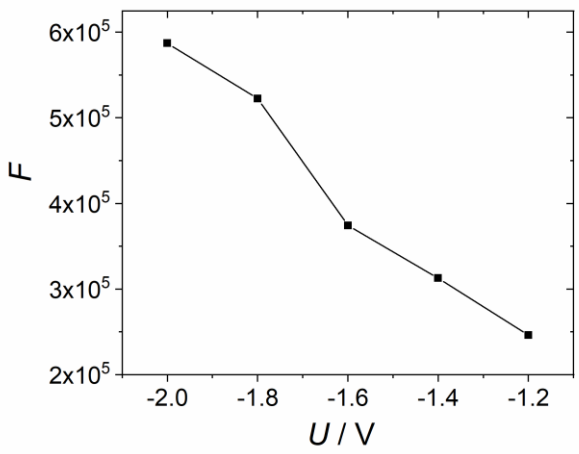

Figure 70: The relation between the fluorescence response of the reduction of 1 mM resazurin in 0.1 M PBS (pH 7.4) on the cathodic pole and the oxidation of 10 µM in 0.1 KNO_3 solution on the anodic pole at different driving potential. 25 µm Pt BE was used for coupling and Pt feeder electrode for applying potential.

4.7.4 Suitable dye used as a reporter for the oxidation of NPs

In order to separate the oxidation events on the anodic pole well, the resorufin formed by the reduction of resazurin on the reporter pole needs to be removed when the circuit is switched off. Because resazurin is reduced irreversibly as illustrated in Fig. 66, the removal of resorufin is achieved solely by diffusion out of the observation volume, which is slow and incomplete. This could affect the accuracy of the measurements and the time resolution of the oxidation events. Moreover, the accuracy of the measurement using resazurin was not satisfying because the fluorescence intensity baseline is not stable. Resazurin itself is not completely nonfluorescent, but instead shows a weak fluorescence. The irreversibility of resazurin electrochemistry was checked by scanning the potential from -1.0 V to 1.0 V at a glassy carbon electrode using a scan rate of 5 mV/s. As displayed in Fig. 71, resazurin was reduced irreversibly (the peak inside the black dashed circle) where the corresponding oxidation peak was missing. When the resazurin was reduced further, dihydroresorufin was formed. The second reduction of resazurin is reversible as it is clear from Fig. 71, where the reduction and the oxidation peaks are located inside the blue dashed circles.

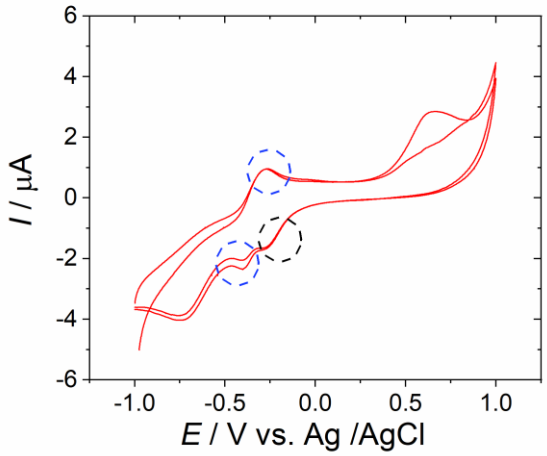

Figure 71: Cyclic voltammetry of 1mM resazurin at glassy carbon electrode, the scan rate is 5 mV s^{-1}.

The removal of the fluorescent compound from the bulk solution after the circuit is switched off by re-oxidation is an alternative to the removal by diffusion. Consequently, the oxidation events on the anodic pole could be detected with high throughput and resolution. However, the reaction rate between the fluorescent product and the oxidizing agent must be slower than the diffusion rate of fluorescent product. Otherwise, the fluorescent product inside the observation volume is oxidized fast before the detection. Diffusion coefficient is another precaution has to be taken into account. If the dye leaves the observation volume very fast, the accurate of the detection will be lost. The vanishing of the fluorescence by chemical reaction requires a reversible fluorescent dye. Number of dyes which are fluorescent in the reduced state and non-fluorescent in oxidized state is very limited. To solve this problem, dyes that are fluorescent in the reduced state must be oxidized chemically. Then, the produced molecules become non-fluorescent in the oxidized state which are re-reduced by BPE to the fluorescent molecules in the reduced state. Using electrochemical methods to produce non-fluorescent molecule in the oxidized state is not effective because an excess of the oxidizing agent is required for the BPE measurments. By this excess, the fluorescent dye can be re-oxidized again to non-fluorescent dye after the circuit is switched off.

N,N-bis(2,5-di-tert-butylphenyl)-3,4,9,10-perylenebis(dicarboximide) (DBPI). First, DBPI was used, which has a stable non-florescent intermediate in the oxidized form. DBPI has two reversible oxidative peaks in dichloroethane[278]. The first oxidative peak at 1.4 V and the second at 1.6 V. To obtain a stable non-fluorescent intermediate, the oxidative potential must

be between 1.4 V and 1.6 V. If the oxidative potential exceeds 1.6 V, a non-stable intermediate will form which quickly returns to the reduced form. So far, oxidizing it chemically was not successful because most suitable oxidizers are not sufficiently soluble in organic solvents or have strong absorption in the UV-Vis region (Fig. 72a).

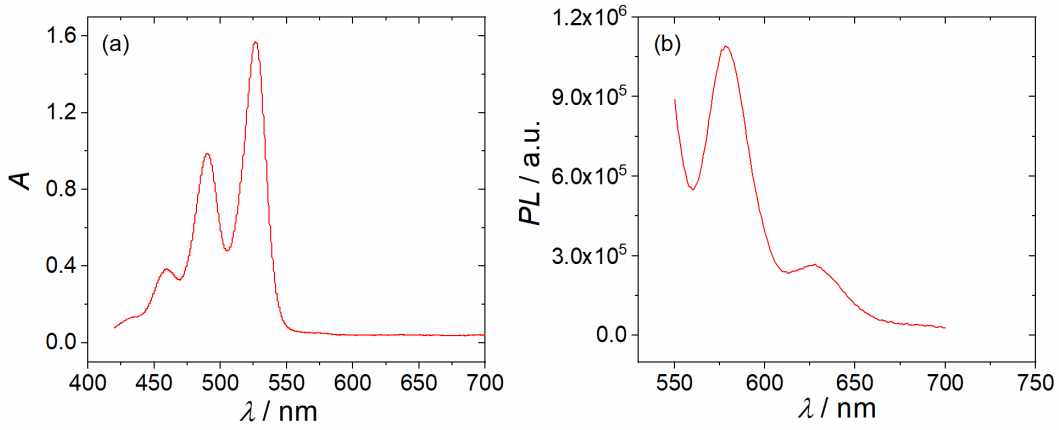

Figure 72: (a) Absorption, and (b) emission spectra of N,N-bis(2,5-di-tert-butylphenyl)-3,4,9,10-perylenebis(dicarboximide) (DBPI) in propylene carbonate solvent (λ_{ex} = 440 nm).

Tris-(bipyridine)-ruthenium(II) chloride is a fluorescent dye and water soluble. It has a stable non-fluorescent oxidized form tris-(bipyridine)-ruthenium(III) chloride that can be easily re-reduced in our experiment. Tris-(bipyridine)-ruthenium(II) chloride mostly was used as a reporter in approaches that use a chemiluminescence readout. In these methods, Ru(II) and a co-reactant such as tripropylamine (TPrA) are oxidized on the anodic pole to form Ru(III) and the cation radical of TPrA (Fig. 73). After the co-reactant is deprotonated, a very energetic electron transfers from the co-reactant to Ru(III). Consequently, the excited state of Ru(II), ($Ru(II)^*$), is formed. When the molecule in the excited state relaxes, the emission of one photon takes place.

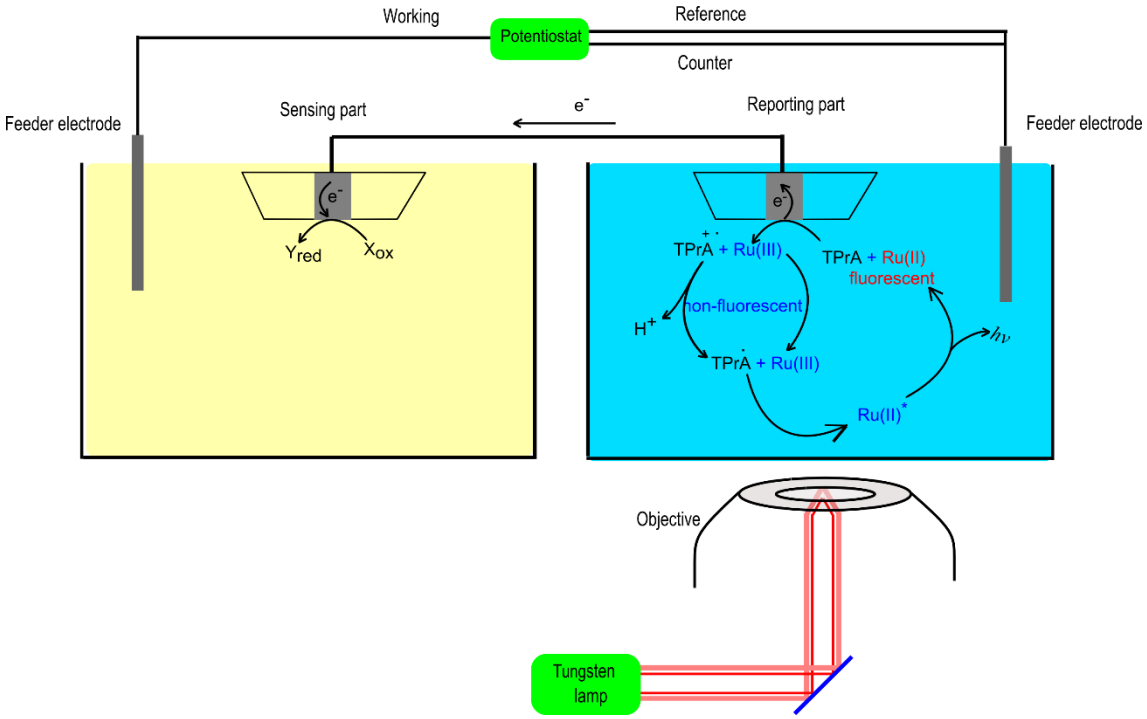

Figure 73: The mechanism of chemiluminescence reporter in BPE.

At the best case (100 % quantum yields), one electron coupled to the reduction on the cathodic pole produces one photon on the anodic pole. Furthermore, Ru(II) as chemiluminescence-based reporter is used to study just the reduction of the redox species on the cathodic pole.

4.7.5 Titration of Ru(II) by absorption and emission spectroscopy

Here, Ru(III) was used to generate luminescence without the need of a co-reactant. Ru(III) was prepared chemically outside of the BPE cell by oxidation with cerium (IV) as seen in Eq. (34).

$$\mathrm{Ru(II)} + \mathrm{Ce(IV)} \rightarrow \mathrm{Ru(III)} + \mathrm{Ce(III)} \qquad (34)$$

The prepared Ru(III) solution has to be completely non-fluorescent to obtain a stable baseline. The vanishing of the luminescence was checked firstly by a naked eye. The luminescence disappeared after addition 0.6 mL of 0.1 M Ce(IV) to 10 mL of 1 mM Ru(II). However, under blue light, some luminescence was left. This indicates that Ru(II) was not completely oxidized to Ru(III). When 1.0 mL of Ce(IV) was added, the luminescence completely disappeared. For

more accuracy, absorption and emission spectroscopy were used to monitor the stepwise adding of Ce(IV) to Ru(II).

The decrease in the fluorescence intensity of Ru(II) at 650 nm upon adding Ce(IV) is shown in Fig. 74. The emission intensity decreased slowly till the third addition (0.6 mL) of Ce(IV). After the fourth addition (0.2 mL more), the emission intensity was decreased dramatically which confirms that Ru(II) was completely consumed. When >1.0 mL of Ce(IV) was added, the emission and excitation intensity increased again (inset of Fig. 74a,b). Interestingly, the prepared solution was unstable especially when the solution was introduced to the light. After short time (some minutes), it started to produce luminescence gradually till it returned completely to Ru(II). However, the redox cycle of Ru(II) is unstable in aqueous solution as explained in the literature[279] due to its ability to oxidize the solvent in aqueous solution.

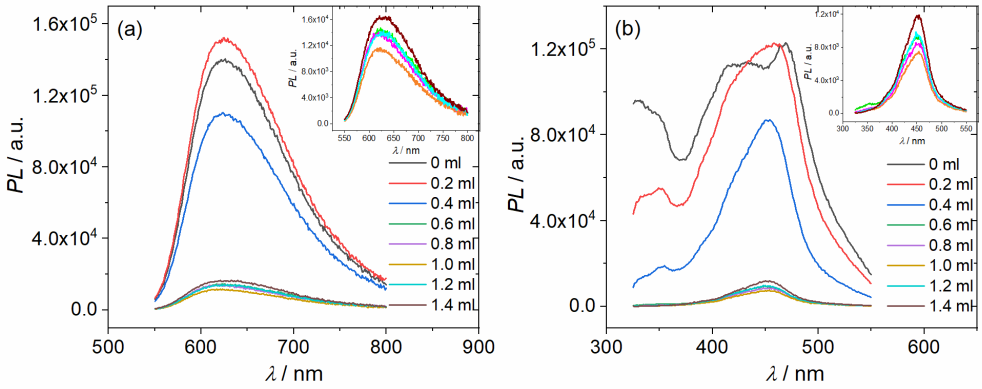

Figure 74: Controlling the stepwise addition of of 0.1 M Ce(IV) to 10 mL of 1 mM Ru(II) by (a) emission, (b) excitation, the excitation wavelength is 450 nm and emission wavelength is 607 nm.

As displayed in Fig. 75, two absorption peaks emerged at wavelength of 420 nm and 470 nm for Ru(II). The peak at 420 belongs to the ligand metal charge transfer ($\pi^* \rightarrow d$), while the other peak at 470 nm belongs to the metal-ligand charge transfer ($d \rightarrow \pi^*$)[280]. When the reaction between the cerium and ruthenium complex converts Ru(II) to Ru(III) by Eq. 34, an electron is removed from the metal orbital. Consequently, the $4d^5$ Ru(III) configuration is produced and the ($d \rightarrow \pi^*$) band is suppressed. The diminished intensity of the 470 nm absorption upon the oxidation with Ce(IV) supports that Ru(II) was oxidized to Ru(III). Nevertheless, the peak of 420 nm remains because it belongs to the ligand metal charge transfer.

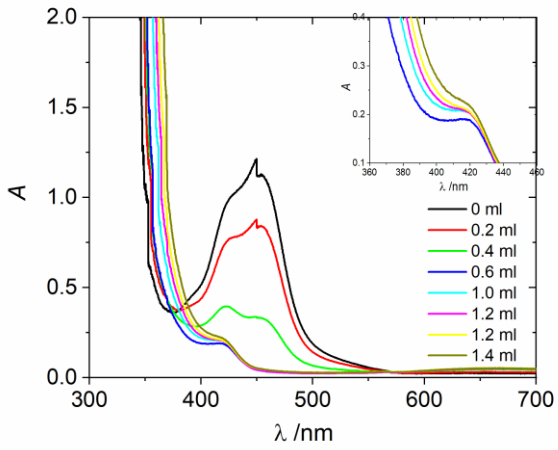

Figure 75: Controlling the stepwise addition of of 0.1 M Ce(IV) to 10 mL of 1mM Ru(II) by (a) emission.

The prepared Ru(III) and a slight excess of oxidizing agent Ce(IV) were placed in the reporter half-cell (cathodic pole) and the analyte was placed in the sensing half-cell (anodic pole). Figure 76 illustrates the mechanism of switching the lumeniscence between on and off states. When the circuit was switched on, FcMeOH molecules were oxidized and the resulting charges were transmitted through the BE. These charges promoted the reduction of Ru(III) complex to Ru(II) (fluorescent complex). The amount of generated Ru(II) dependeds on the number of oxidized FcMeOH molecules. When the circuit was switched off (Fig. 76), the produced fluorescent Ru(II) molecules interacted with Ce(IV) in the bulk solution and returned to the non-fluorescent state. Unlike the electrochemiluminescence-based method, one electron not only causes the emission of one photon, but the electron produces one fluorogenic molecule that undergoes multiple absorption-emission cycles with high frequency. So, fluorescence-based methods are potentially highly sensitive methods if there is no background fluorescence. In contrast, electrochemoluminscence is a more robust method in situations when background fluorescence cannot be completly supressed.

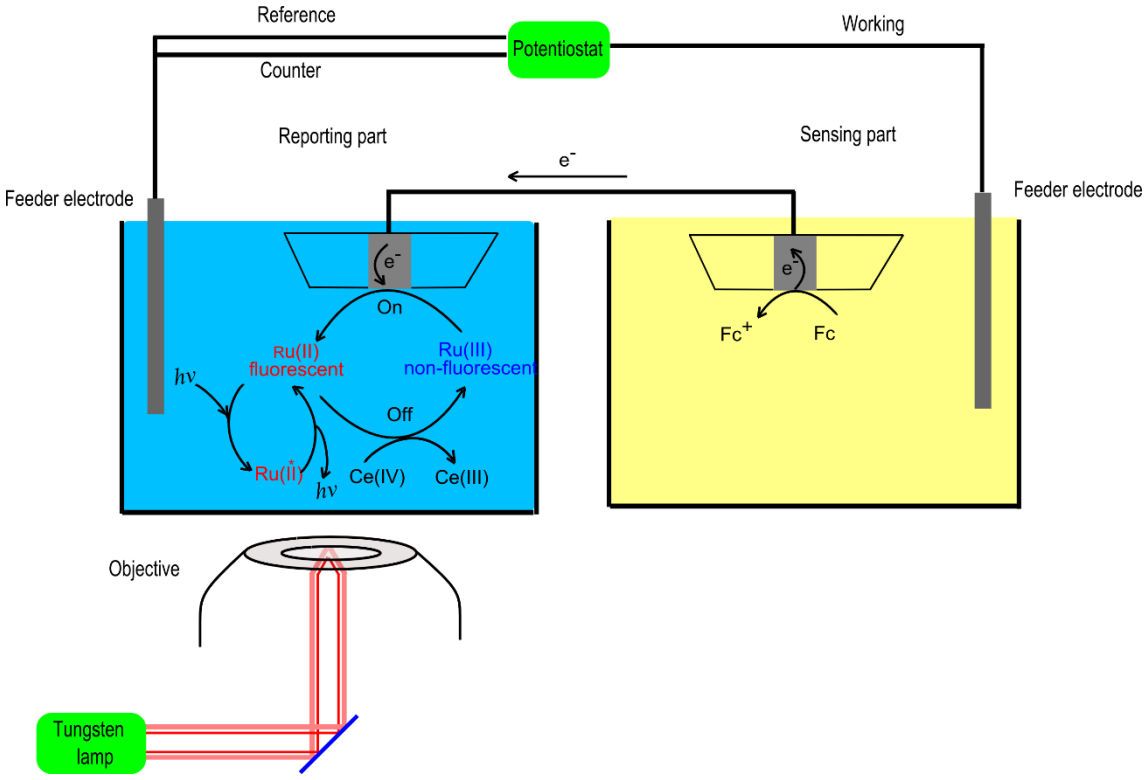

Figure 76: Coupling the reduction of Ru(III) with the oxidation of FcMeOH.

To check the effectivity of the reversible dye, the same concentration of Ru(III) and resazurin were coupled to the oxidation of 10 µM FcMeOH. Fig. 77 shows the behaviour of the resazurin and Ru(III) upon switching the circuit between on and off. By comparison, the signal from the resazurin reporter (Fig. 77a) shows less broadening than Ru(II) (Fig. 77b) which means that Ru(II) left the observation volume slower than resorufin. These results was expected because D of Ru(III) (3.3×10^{-8} cm^2 s^{-1}) is smaller than that of resazurin ($D = 7.8\times10^{-6}$ cm^2 s^{-1}). Although the chemical processes are mostely faster than the diffusion process, the electrogenerated Ru(II) diffused away from the electrode surface before being re-oxidized back chemically to Ru(III) due to the slow reaction rate between Ru(II) and Ce(IV). In case of irreversible dye such as resazurin, the fluorescent product leaves the electrode surface only by diffusion. This is not useful because the fluorescent product accumulates in the bulk solution and consequently affects on the accuracy of the detection. Ru(II) dye is preferred here over resazurin dye because of two reasons. Firstly, Ru(II) was re-oxidized by Ce(IV) and consequently the accumulation of Ru(II) in the bulk solution was avoided. Secondely, Ru(II) left the observation volume slower than resazurin which is useful for recording the photons precisely. Fast homogeous redox reaction is not useful in case of single events detection because counting the fluorescence

signal in the reporting part precisely is very important. If the fluorescent product leave the observation volume very fast, the sensitivity will be lost.

.

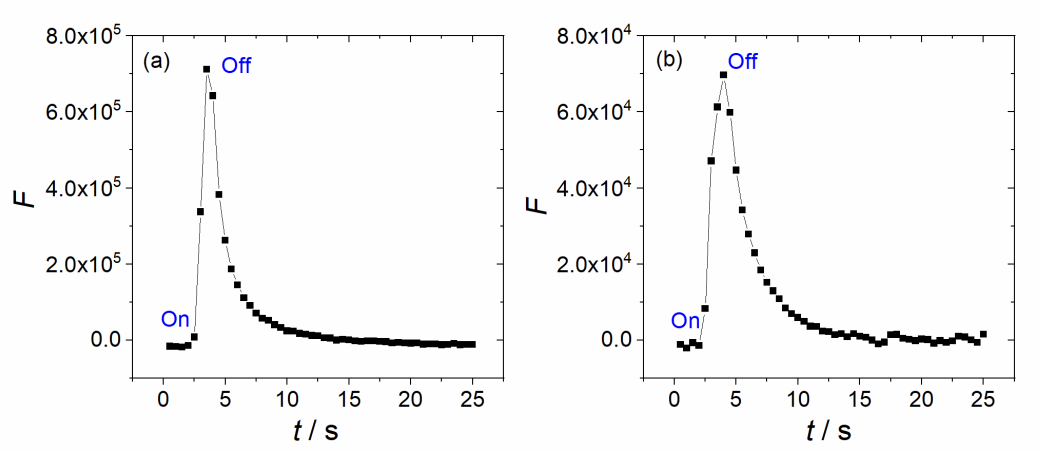

Figure 77: Reporting the oxidation of FcMeOH by the reduction of (a) resazurin, (b) Ru(III) complex.

5 Conclusion and outlook

The kinetic events of fluorescent NPs at a Pt (ME) surface were studied. For this purpose, FCS and electrochemical measurements were combined together. The diameter of the ME used as working electrode was typically around 1 μm to match the diameter of the optical observation volume and to minimize bulk contributions as well. CdSe/CdS QDs with negatively charged shells were used as example for semiconductor and Ag-Au NPs with cytidine shell as example for metallic NPs. In chapter 4.2, CV and DPV were performed as a preliminary experiments to check the electrochemical behaviour of these particles at macroelectrode surface. These experiments showed an irreversible oxidation of the QDs and Ag-Au NPs. Furthermore, a prominent reduction peak emerged at -0.6 V in the CV of Ag-Au NPs which was attributed to the reduction of cytidine negative shell.

FCS measurements in addition to the simulation data in chapter 4.6 confirm that QDs with carboxylate capping are adsorbed to the electrode at $E > + 0.6$ V vs. Ag/AgCl and oxidized partially. Emission lifetime decreased slightly at the oxidation potential which indicates the ability of QDs that are desorbed from the electrode surface to emit light. Although QDs are irreversibly oxidized, QDs are not significantly modified upon electrochemical oxidation during a single QD-electrode contact. Although these QDs are very small, they need a sequence of collisions like a large metallic NPs (> 10 nm) to be entirely oxidized or even transformed to lose their emission characteristics. In case of Ag-Au NPs (2 nm), $<N>$ decreased from 2.5 to 1.3. This means that half of the accumulated particles at the electrode surface were oxidized totally at +0.4 V.

To define number of sequences that NPs require to be completely disappeared, the fluorescence output should be synchronized with the current spikes. However, this synchronization failed because the direct single NP collision experiments with direct NP transformation produce very low Faradaic current. This current was very close to the thermal noise as shown in chapter 4.3. So, in chapter 4.7 the conventional electrochemistry was replaced with BPE and coupled with fluorescence microscopy. In this method, the interaction of NPs at the electrode surface was studied indirect via fluorogenic dye which has an observable and sensitive readout. The fluorescence output of very efficient fluorescent dye on the cathodic pole was used to observe a complete dissolution picture for the NPs on the anodic pole

Because resazurin is reduced to highly fluorescent resorufin that was used extensively in the literature, it was used for this purpose. By using resazrin as a reporter, the accuracy of the mesurements was not satisfied because resazurin is reduced irreversibly and the removal of resorufin is achieved solely by diffusion out of the observation volume, which is slow and incomplete. The accumulation of the fluorescent product in the bulk solution after the circuit was switched off affected the counting accuracy of the photons inside the observation volume. So, a reversible dye was required to remove the fluorescent product in the bulk solution after the circuit is switched off. Ru(II) was re-oxidized by excess of Ce(IV) inside the BPE cell after the circuit was switched off. This type of reaction was used here because the reaction rate is slow. If the reaction rate was faster than the diffusion, the fluorescent product in the confocal volume would be re-oxidized very fast. Consequently, the accurate of the measurements will be affected. Intersetingly, the Ru(II) complex needed more time than resorufin products to leave the observation volume. The slower diffusion for Ru(II) gave the opportunity to count the photons output precisely.

Because FcMeOH has a well known reversible electrochemistry, it was used as an electrochemical reference for the NPs measurements. It was used to establish a correlation between the produced current on the anodic pole and the photon output on the cathodic pole. Determining the detection limit of the analyte was the first step before going further to single NPs detection. Although all precautions were considered, the detection limit for FcMeOH was 10 µM. This detection limit is higher than the detetcion limit of a pure electrochemcial detection and thus unsatisfying for the pursued purpose. So far, combining the fluorescence spectroscopy with bipolar electrochemistry did not help for determining submicromolar concentrations because of the fluorescence background. The high overall potential required for BPE and the changing potential drop at each of the involved solid-liquid interfaces represents another problem. At high potential, everything inside the solution can be oxidized even the solvent itself.

The work reported in this thesis exposed a lot of challenges which are related not only to the sensitivity of the detection methods but also to the sensitivity of NPs detection itself. In the first, the thermal noise floor obstructed the identification of electronic signal generated by the collision of NPs with the surface of ME. Then, fluorescence background was an obstacle not only in case of NPs detection by conventional electrochemistry but also in case of bipolar electrochemistry with optical readout. Because the fluorescence background in the reporting part is not easy to remove, the conditions in the sensing part must be optimized. In the sensing

part, there are two problems such as the competition between the oxidation of water and the oxidation of the analyte in the sensing part. The other problem is the random diffusion of NPs inside the solution. In order to proceed in optimizing the BPE sensitivity, several possibilities can be considered such as insertion of an auxiliary compound beside the analyte in the solution. Also, the solution can be introduced to the electrochemical cell through a microfluidics channel as detailed below.

Auxiliary compound (Aux): To recognize the analyte precisely, the fluorescent output intensity in the reporting part must be correlated to the oxidation of the analyte in the sensing part. Therefore, oxidation of any unwanted substances must be prevented. The presence of other substances which can be oxidized increases the output luminescent intensity on the reporting side and consequently affects the accuracy of the analyte detection. If the solution is evacuated from the oxidized materials, the solvent is still there and indispensable. This is considered as a big dilemma in that regard because it should be oxidized and / or reduced at a certain potential. In the previous experiments, high potential (>2.5 V) was required to detect a clear fluorescence in the reporting part. This fluorescence was attributed to the water electrolysis beside the oxidation of the analyte in the sensing part because the fluorescence was seen also in absence of the analyte. The reason for simultaneous oxidation of the analyte and the solvent could be explained according to the basics of electrochemistry. In principle, the oxidation reaction cannot occur without a reduction reaction happening at the same time. The oxidation half-reaction and the reduction half-reaction form the whole reaction. As explained in chapter 5.7, the feeder electrode in the sensing part must be charged as negative if the analyte has to be oxidized on the BE in the same part. Therefore, a reduction on the feeder electrode and oxidation on BE occur simultaneously in the same solution. The reduction of the solvent is used to balance the oxidation of the analyte if no auxiliary compound is placed inside the solution. At potential window less than the potential window of water electrolysis, the oxidation of the analyte on the BE did not take place because no substance exists inside the solution that can be reduced at the feeder electrode. So, no fluorescence was seen till the applied potential reached the potential of water oxidation. At certain cell voltage, the water is not only reduced but also oxidized on another electrode at another potential[281]. This is not useful in case of bipolar experiments because the oxidation of water competes with the oxidation of the analyte. To avoid competition between the redox reaction of water and the oxidation of the analyte, an auxiliary compound is required. It should have a reductive potential less than the redox potential of water, but an oxidation potential higher than the analyte. Reduction of the

auxiliary compound on the feeder electrode balances the oxidation of the analyte on the BE as illustrated in Fig. 78. In that case, any fluorescence could be seen in the reporting part is attributed to the oxidation events of the analyte alone. If this idea is accomplished and the output of the oxidation events at very low concentration (< pM) could be seen, the probability to the study the oxidation events of single NPs at the surface of ME will increase. Consequently, a correlation can be built up between the concentration of NPs in the sensing part and the fluorescence output in the reporting part.

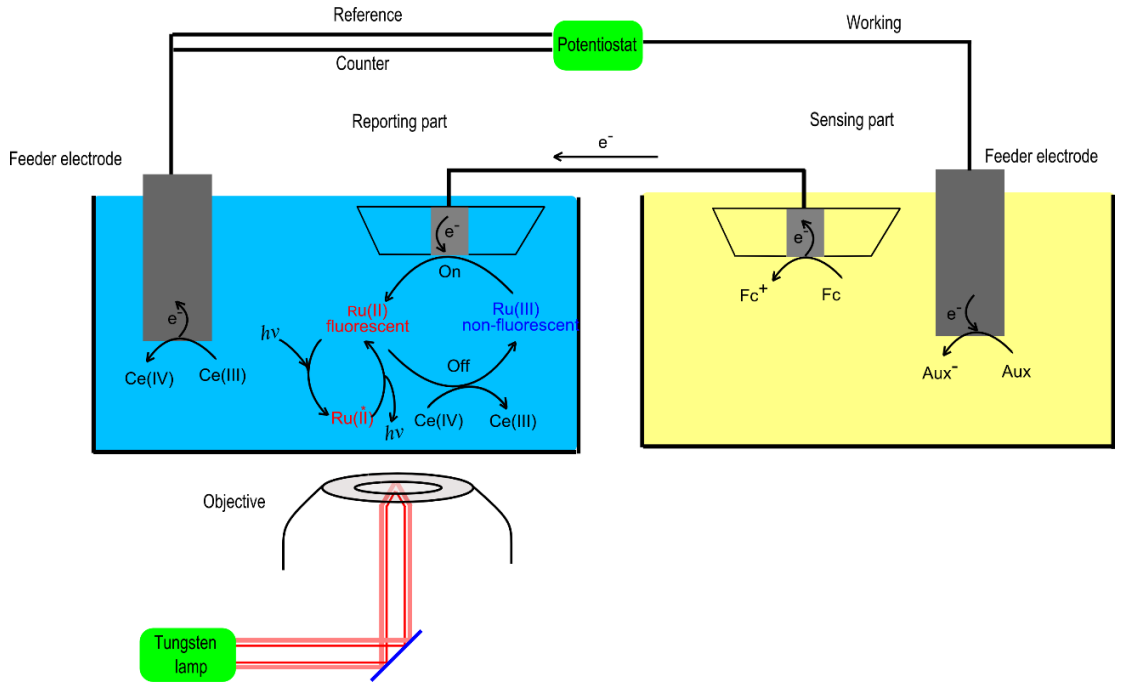

Figure 78: Mechanism of the coupled reactions that occur on the feeder and BE in the sensing and reporting part.

Microfluidics: In case of single NP detection, reaching a detection limit as low as possible is very important because the events of single NPs must be separated and identified. Also, directing the NPs to the surface of MEs instead of the random transport improves the precision of detection. So, injection of the NPs through a microfluidic channel could be an option to minimize the limit of detection and to increase the resolution of the oxidation events. This method was used as a good alternative to the conventional methods for NP separation and allows for minimum aggregation[282]. The position of a NP inside the bulk solution and its flow velocity can influence the detection signal. This method confines NPs in a very small volume and increases the capability of the detection. To direct the NPs to the ME surface with a certain velocity and avoid the random movements of the NP towards the ME, the channel is connected

directly with BE. So, the anodic pole of BE is part of the inner channel while the cathodic pole contacts a solution reservoir outside of the channel as illustrated in Fig. 79. The NPs are injected to the channel through the inlet and leave through the outlet. The fluorogenic molecules are placed in the reporting cell outside the channel. Decrease the required potential is another advantage for this method. As discussed in chapter 2.5, the potential difference between the poles of BE is a fraction of the total cell voltage between the the feeder electrodes. So, the potential drop within the electrolyte solution depends on the volume of the solution. By decreasing the volume, less driving force is required to overcome the solution a resistance and an overall lower cell voltage between the feeder electrodes should be sufficient. This would avoid the overlap between the potential window of water splitting and the analyte.

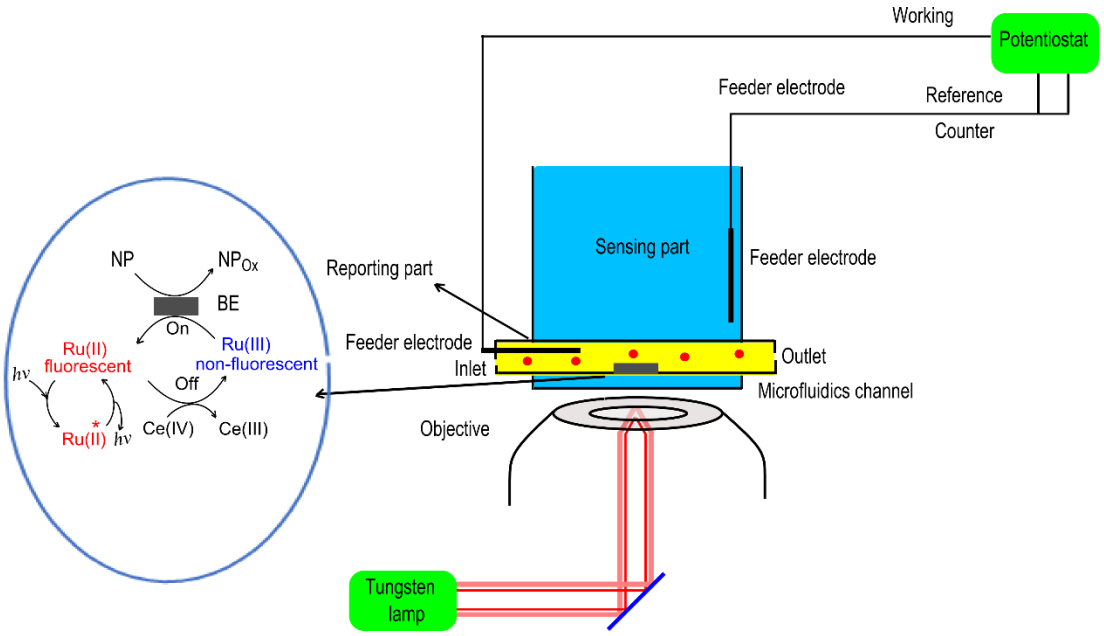

Figure 79: Coupling the oxidation of NPs inside the microfluidic channel and the reduction of Ru(II) outside the microfluidic channel.

6 References

[1] I. Robel, V. Subramanian, M. Kuno, P. V. Kamat, *J. Am. Chem. Soc.* **2006**, *128*, 2385.
[2] D. Astruc, F. Lu, J. R. Aranzaes, *Angew. Chem., Int. Ed.* **2005**, *44*, 7852.
[3] F. W. Campbell, R. G. Compton, *Anal. Bioanal. Chem.* **2010**, *396*, 241.
[4] P. V. Kamat, *J. Phys. Chem. B* **2002**, *106*, 7729.
[5] M. B. Gawande, A. Goswami, T. Asefa, H. Guo, A. V. Biradar, D.-L. Peng, R. Zboril, R. S. Varma, *Chem. Soc. Rev.* **2015**, *44*, 7540.
[6] E. Petryayeva, W. R. Algar, I. L. Medintz, *Appl. Spectrosc.* **2013**, *67*, 215.
[7] H. Huang, J.-J. Zhu, *Analyst* **2013**, *138*, 5855.
[8] A. P. Alivisatos, *J. Electroanal. Chem.* **1996**, *100*, 13226.
[9] a) X. Zhou, E. Choudhary, N. M. Andoy, N. Zou, P. Chen, *ACS Catal.* **2013**, *3*, 1448; b) S. Levin, J. Fritzsche, S. Nilsson, A. Runemark, B. Dhokale, H. Ström, H. Sundén, C. Langhammer, F. Westerlund, *Nat. Commun.* **2019**, *10*, 4426.
[10] a) C. Burda, X. Chen, R. Narayanan, M. A. El-Sayed, *Chem. Rev.* **2005**, *105*, 1025; b) C. B. Murray, D. J. Norris, M. G. Bawendi, *J. Am. Chem. Soc.* **1993**, *115*, 8706; c) Y. Xia, X. Xia, H.-C. Peng, *J. Am. Chem. Soc.* **2015**, *137*, 7947; d) M. T. M. Koper, *Nanoscale* **2011**, *3*, 2054; e) T. Vossmeyer, L. Katsikas, M. Giersig, I. G. Popovic, K. Diesner, A. Chemseddine, A. Eychmueller, H. Weller, *J. Phys. Chem.* **1994**, *98*, 7665.
[11] B. O. Dabbousi, J. Rodriguez-Viejo, F. V. Mikulec, J. R. Heine, H. Mattoussi, R. Ober, Jensen, K. F., M. G. Bawendi, *J. Phys. Chem. B* **1997**, *101*, 9463.
[12] A. P. Alivisatos, *Science* **1996**, *271*, 933.
[13] X. Xiao, A. J. Bard, *J. Am. Chem. Soc.* **2007**, *129*, 9610.
[14] X. Xiao, F.-R. F. Fan, J. Zhou, A. J. Bard, *J. Am. Chem. Soc.* **2008**, *130*, 16669.
[15] J. Yao, K. D. Gillis, *Analyst* **2012**, *137*, 2674.
[16] A. Schulte, R. H. Chow, *Anal. Chem.* **1998**, *70*, 985.
[17] F.-R. F. Fan, A. J. Bard, *Science* **1995**, *267*, 871.
[18] S. J. Kwon, H. Zhou, F.-R. F. Fan, V. Vorobyev, B. Zhang, A. J. Bard, *Phys. Chem. Chem. Phys.* **2011**, *13*, 5394.
[19] S. J. Kwon, A. J. Bard, *J. Am. Chem. Soc.* **2012**, *134*, 7102.
[20] B.-K. Kim, A. Boika, J. Kim, J. E. Dick, A. J. Bard, *J. Am. Chem. Soc.* **2014**, *136*, 4849.
[21] A. Boika, S. N. Thorgaard, A. J. Bard, *J. Phys. Chem. B* **2013**, *117*, 4371.
[22] J. E. Dick, A. T. Hilterbrand, A. Boika, J. W. Upton, A. J. Bard, *Proc. Natl. Acad. Sci. U. S. A.* **2015**, *112*, 5303.
[23] E. Laborda, A. Molina, C. Batchelor-McAuley, R. G. Compton, *ChemElectroChem* **2018**, *5*, 410.
[24] J. E. Dick, C. Renault, A. J. Bard, *J. Am. Chem. Soc.* **2015**, *137*, 8376.
[25] J. Ustarroz, M. Kang, E. Bullions, P. R. Unwin, *Chem. Sci.* **2017**, *8*, 1841.
[26] E. N. Saw, M. Kratz, K. Tschulik, *Nano Res.* **2017**, *10*, 3680.
[27] S. M. Oja, D. A. Robinson, N. J. Vitti, M. A. Edwards, Y. Liu, H. S. White, B. Zhang, *J. Am. Chem. Soc.* **2017**, *139*, 708.
[28] E. Kätelhön, A. Feng, W. Cheng, S. Eloul, C. Batchelor-McAuley, R. G. Compton, *J. Phys. Chem. C* **2016**, *120*, 17029.
[29] C. A. Little, X. Li, C. Batchelor-McAuley, N. P. Young, R. G. Compton, *J. Electroanal. Chem.* **2018**, *823*, 492.

[30] F. Zhang, M. A. Edwards, R. Hao, H. S. White, B. Zhang, *J. Phys. Chem. C* **2017**, *121*, 23564.
[31] Y. Fang, H. Wang, H. Yu, X. Liu, W. Wang, H.-Y. Chen, N. J. Tao, *Acc. Chem. Res.* **2016**, *49*, 2614.
[32] C. M. Hill, S. Pan, *J. Am. Chem. Soc.* **2013**, *135*, 17250.
[33] S. Sun, M. Gao, G. Lei, H. Zou, J. Ma, C. Huang, *Nano Res.* **2016**, *9*, 1125.
[34] E. Cortés, P. G. Etchegoin, E. C. Le Ru, A. Fainstein, M. E. Vela, R. C. Salvarezza, *J. Am. Chem. Soc.* **2010**, *132*, 18034.
[35] L. Li, U. Steiner, S. Mahajan, *Nano Lett.* **2014**, *14*, 495.
[36] M. Dias, P. Hudhomme, E. Levillain, L. Perrin, Y. Sahin, F.-X. Sauvage, C. Wartelle, *Electrochem. Commun.* **2004**, *6*, 325.
[37] J. P. Guerrette, S. J. Percival, B. Zhang, *J. Am. Chem. Soc.* **2013**, *135*, 855.
[38] C. Lei, D. Hu, E. J. Ackerman, *Chem. Commun.* **2008**, 5490.
[39] R. E. Palacios, F.-R. F. Fan, A. J. Bard, P. F. Barbara, *J. Am. Chem. Soc.* **2006**, *128*, 9028.
[40] C. Ma, L. P. Zaino, P. W. Bohn, *Chem. Sci.* **2015**, *6*, 3173.
[41] G. Wittstock, S. Rastgar, S. Scarabino, *Curr. Opin. Electrochem.* **2019**, *13*, 25.
[42] S. K. Haram, B. M. Quinn, A. J. Bard, *J. Am. Chem. Soc.* **2001**, *123*, 8860.
[43] M. Amelia, C. Lincheneau, S. Silvi, A. Credi, *Chem. Soc. Rev.* **2012**, *41*, 5728.
[44] J. Liu, W. Yang, Y. Li, L. Fan, Y. Li, *Phys. Chem. Chem. Phys.* **2014**, *16*, 4778.
[45] A. L. Efros, M. Rosen, *Annu. Rev. Mater. Sci.* **2000**, *30*, 475.
[46] W. Qin, R. A. Shah, P. Guyot-Sionnest, *ACS nano* **2012**, *6*, 912.
[47] T. J. Jacobsson, T. Edvinsson, *J. Phys. Chem. C* **2013**, *117*, 5497.
[48] X. Ma, A. Mews, T. Kipp, *J. Phys. Chem. C* **2013**, *117*, 16698.
[49] Stokes. G. G, *Philos. Trans. R. Soc.* **1852**, *142*, 463.
[50] J. R. Lakowicz, *Principles of fluorescence spectroscopy*, Springer, New York, **2006**.
[51] a) T. Imamura, T. Saitou, R. Kawakami, *Cancer Sci.* **2018**, *109*, 912; b) S. A. Kim, K. G. Heinze, P. Schwille, *Nat. Methods* **2007**, *4*, 963.
[52] a) A. Henglein, *Chem. Rev.* **1989**, *89*, 1861; b) L. Shang, S. Dong, G. U. Nienhaus, *Nano Today* **2011**, *6*, 401; c) D. Roy, S. Mandal, C. K. De, K. Kumar, P. K. Mandal, *Phys. Chem. Chem. Phys.* **2018**, *20*, 10332.
[53] D. C. Nguyen, R. A. Keller, *Anal. Chem.* **1987**, *59*, 2158.
[54] R. Hao, Y. Fan, B. Zhang, *J. Am. Chem. Soc.* **2017**, *139*, 12274.
[55] P. Chen, X. Zhou, H. Shen, N. M. Andoy, E. Choudhary, K.-S. Han, G. Liu, W. Meng, *Chem. Soc. Rev.* **2010**, *39*, 4560.
[56] Q. Zhang, J. Xie, Y. Yu, J. Y. Lee, *Nanoscale* **2010**, *2*, 1962.
[57] Y. Zhang, H. Jiang, X. Wang, *Anal. Chim. Acta* **2015**, *870*, 1.
[58] P. Malik, J. Singh, R. Kakkar, *Adv. Mat. Lett.* **2014**, *5*, 612.
[59] a) G. A. J. Amaratunga, M. Chhowalla, C. J. Kielyt, I. Alexandrou, R. Aharonov, R. M. Devenis, *Nature* **1996**, *383*, 321; b) K. D. Patel, R. K. Singh, H.-W. Kim, *Mater. Horiz.* **2019**, *6*, 434.
[60] K. Z. Brainina, L. G. Galperin, E. V. Vikulova, *J. Solid State Chem.* **2012**, *16*, 2357.
[61] O. S. Ivanova, F. P. Zamborini, *J. Am. Chem. Soc.* **2010**, *132*, 70.
[62] Y. Chen, H. Chen, J. Shi, *Adv. Mater.* **2013**, *25*, 3144.
[63] a) H. Gerischer, *Electrochim. Acta* **1990**, *35*, 1677; b) A. Eychmüller, A. Hässelbarth, L. Katsikas, H. Weller, *Ber. Bunsenyes. Phys. Chetn.* **1991**, *95*, 79.

[64] A. Grillone, E. R. Riva, A. Mondini, C. Forte, L. Calucci, C. Innocenti, C. Fernandez, V. Cappello, M. Gemmi, S. Moscato et al., *Adv. Healthcare Mater.* **2015**, *4*, 1681.
[65] L. M. Rossi, P. R. Silva, L. L. R. Vono, A. U. Fernandes, D. B. Tada, M. S. Baptista, *Langmuir* **2008**, *24*, 12534.
[66] L. E. Brus, *J. Chem. Phys.* **1983**, *79*, 5566.
[67] H.-Z. Wang, H.-Y. Wang, R.-Q. Liang, K.-C. Ruan, *Acta Bioch. Bioph. Sin.* **2004**, *36*, 681.
[68] J. McBride, J. Treadway, L. C. Feldman, S. J. Pennycook, S. J. Rosenthal, *Nano Lett.* **2006**, *6*, 1496.
[69] C. Kumar, *Semiconductor nanomaterials*, USA, **2010**.
[70] a) M. G. Bawendi, P. J. Carroll, W. L. Wilson, L. E. Brus, *J. Chem. Phys.* **1992**, *96*, 946; b) C. Burda, S. Link, M. Mohamed, M. El-Sayed, *J. Phys. Chem. B* **2001**, *105*, 12286; c) X. Wang, J. Wu, F. Li, H. Li, *J. Nanotechnol.* **2008**, *19*, 205501.
[71] J. Vela, H. Htoon, Y. Chen, Y.-S. Park, Y. Ghosh, P. M. Goodwin, J. H. Werner, N. P. Wells, J. L. Casson, J. A. Hollingsworth, *J. Biophotonics* **2010**, *3*, 706.
[72] C. Cheng, H. Yan, *Physica E 41* **2009**, *41*, 828.
[73] a) L.-W. Liu, S.-Y. Hu, Y. Pan, J.-Q. Zhang, Y.-S. Feng, X.-H. Zhang, *Beilstein J. Nanotechnol.* **2014**, *5*, 919; b) X. Wang, J. Yu, R. Chen, *Sci. Rep.* **2018**, *8*, 17323.
[74] W. W. Yu, L. Qu, W. Guo, X. Peng, *Chem. Mater.* **2003**, *15*, 2854.
[75] A. M. Smith, S. Nie, *Acc. Chem. Res.* **2010**, *43*, 190.
[76] J. Zheng, P. R. Nicovich, R. M. Dickson, *Annu. Rev. Phys. Chem.* **2007**, *58*, 409.
[77] G. N. Blackman, D. A. Genov, *Phys. Rev. B* **2018**, *97*.
[78] E. Roduner, *Chem. Soc. Rev.* **2006**, *35*, 583.
[79] A. Moores, F. Goettmann, *New J. Chem.* **2006**, *30*, 1121.
[80] E. Dulkeith, T. Niedereichholz, T. A. Klar, J. Feldmann, G. von Plessen, D. I. Gittins, K. S. Mayya, F. Caruso, *Phys. Rev. B* **2004**, *70*.
[81] J. Tiggesbaumker, L. Kolle, K.-H. Meiwes-Broer, A. Liebsch, *Phys. Rev. A* **1993**, *48*, 48.
[82] a) C. Guo, J. Irudayaraj, *Anal. Chem.* **2011**, *83*, 2883; b) M.-C. Daniel, D. Astruc, *Chem. Rev.* **2004**, *104*, 293; c) M. M. Alvarez, J. T. Khoury, T. G. Schaaff, M. N. Shafigullin, I. Vezmar, Whetten. R. L., *J. Phys. Chem. B* **1997**, *101*, 3706.
[83] B. Xu, K. S. Suslick, *Adv. Mater.* **2010**, *22*, 1078.
[84] E. P. A. M. Bakkers, E. Reitsma, J. J. Kelly, D. Vanmaekelbergh, *J. Phys. Chem. B* **1999**, *103*, 2781.
[85] S. G. Hickey, D. J. Riley, E. J. Tull, *J. Phys. Chem. B* **2000**, *104*, 7623.
[86] V. Rombach-Riegraf, P. Oswald, R. Bienert, J. Petersen, M. P. Domingo, J. Pardo, P. Gräber, E. M. Galvez, *Biochem. Biophys. Res. Commun.* **2013**, *430*, 260.
[87] J. Zhao, G. Nair, B. R. Fisher, M. G. Bawendi, *Phys. Rev. Lett.* **2010**, *104*, 157403.
[88] V. Fomenko, D. J. Nesbitt, *Nano. Lett.* **2008**, *8*, 287.
[89] P. K. HANSMA, V. B. Elings, O. Marti, C. E. Bracker, *Science* **1988**, *242*, 209.
[90] a) M. Bates, B. Huang, G. T. Dempsey, X. Zhuang, *Science* **2007**, *317*, 1749; b) M. J. Rust, M. Bates, X. Zhuang, *Nat. Methods* **2006**, *3*, 793.
[91] M. Böhmer, J. Enderlein, *J. Opt. Soc. Am. B* **2003**, *20*, 554.
[92] V. Vukojevic, M. Heidkampb, Y. Minga, B. Johanssona, L. Tereniusa, R. Rigle, *Proc. Natl. Acad. Sci* **2008**, *105*, 18176.
[93] B. B. Rotmann, *Biochemistry* **1961**, *47*, 1981.

[94] T. Hirschfeld, *Appl. Opt.* **1976**, *15*, 2965.
[95] a) N. J. Dovichi, J. C. Martin, J. H. Jett, M. Tschulik, R. A. Keller, *Anal. Chem.* **1984**, *56*, 348; b) D. E. Koppel, D. Axelord, J. Schlessinger, E. L. Elson, W. W. Webb, *Biophys. J.* **1976**, *16*, 1315; c) Sauter, T., W. Neuhauser, Blatt. R., Toschek. P. E, *Phys. Rev. Lett.* **1986**, *57*, 1696; d) Moerner. W. E., Kador. L, *Phys. Rev. Lett.* **1989**, *62*, 2535.
[96] Shera. E. B., N. k. Seitzinger, L. M. Davis, Keller. R. A., S. A. Soper, *Chem. Phys. Lett.* **1990**, *174*, 553.
[97] J. Wenger, J. Dintinger, N. Bonod, E. Popov, P.-F. Lenne, T. W. Ebbesen, H. Rigneault, *Opt. Commun.* **2006**, *267*, 224.
[98] R. Rigler, Ü. Mets, J. Widengren, P. Kask, *Eur. Biophys. J.* **1993**, *22*, 169.
[99] P. P. Jha, P. Guyot-Sionnest, *J. Phys. Chem. C* **2010**, *114*, 21138.
[100] C. Dong, H. Liu, J. Ren, *Langmuir* **2014**, *30*, 12969.
[101] N. G. Walter, *Ency. Anal. Chem.* **2008**, 1.
[102] D. Magde, E. Elson, W. W. Webb, *Phys. Rev. Lett.* **1972**, *29*, 705.
[103] M. Eiger, R. Rigler, *Proc. Natl. Acad. Sci. U. S. A.* **1994**, *91*, 5740.
[104] E. P. Petrov, P. Schwille in *Springer Series on Fluorescence* (Ed.: U. Resch-Genger), Springer Berlin Heidelberg, Berlin, Heidelberg, **2008**, pp. 145–197.
[105] D. Magde, W. W. Webb, E. L. Elson, *Biopolymers* **1978**, *17*, 361.
[106] E. van Craenenbroeck, Y. Engelborghs, *Biochemistry* **1999**, *38*, 5082.
[107] Y. Takahashi, Y. Okamoto, H. A. Popiel, N. Fujikake, T. Toda, M. Kinjo, Y. Nagai, *J. Biol. Chem.* **2007**, *282*, 24039.
[108] A. Loman, I. Gregor, C. Stutz, M. Mund, J. Enderlein, *Photochem. Photobiol. Sci.* **2010**, *9*, 627.
[109] J. Widengren, R. Rigler, Ü. Mets, *J. Fluoresc.* **1994**, *4*, 255.
[110] J. Widengren, Ü. Mets, R. Rigler, *J. Phys. Chem.* **1995**, *99*, 13368.
[111] E. L. Elson, D. Magde, *Biopolymers* **1974**, *13*, 1.
[112] P. Schwille, E. Haustein, *Nanophotonics* **2001**, 1.
[113] S. R. Aragón, R. Pecora, *J. Chem. Phys.* **1976**, *64*, 1791.
[114] J. R. Lakowicz (Ed.) *Topics in Fluorescence Spectroscopy*, Kluwer Academic Publishers, Boston, **2002**.
[115] R. Rigler, Ü. Mets, J. Widengren, P. Kask, *Eur. Biophys. J.* **1993**, *22*.
[116] J. Widengren, Ü. Mets, R. Rigler, *Chem.phys.* **1999**, *250*, 171.
[117] Schwille. P., F.-J. Meyer-Almes, R. Rigler, *Biophys. J.* **1997**, *72*, 1878.
[118] C. Dong, X. Huang, J. Ren, *Ann. N.Y. Acad. Sci.* **2008**, *1130*, 253.
[119] B. Lounis, H. A. Bechtel, D. Gerion, P. Alivisatos, W. E. Moerner, *Chem. Phys. Lett.* **2000**, *329*, 399.
[120] S. Saffarian, E. L. Elson, *Biophys. J.* **2003**, *84*, 2030.
[121] K. Chattopadhyay, S. Saffarian, E. L. Elson, C. Friedenand, *Proc. Natl. Acad. Sci. U. S. A.* **2002**, *99*, 14171.
[122] U. Haupts, S. Maiti, P. Schwille, W. W. Webb, *Proc. Natl. Acad. Sci. U. S. A.*, *95*, 13573–13578.
[123] R. R. Alfano, S. L. Shapiro, *Phys. Rev. Lett.* **1970**, *24*, 592.
[124] P. Russell, *Appl. Phys.* **2003**, *299*, 358.
[125] K. Štulik, C. AMATORE, K. Holub, Mareck, ,V., W. Kutner, *Pure Appl. Chem.* **2000**, *72*, 1483.
[126] A. J. Bard (Ed.) *Electroanalytical Chemistry*, Marcel Dekker, New York, Basel, **1989**.

[127] C. Amantore, B. Fosset, *Anal. Chem.* **1996**, *68*, 4377.
[128] A. J. Bard, L. R. Faulkner, *Electrochemical methods. Fundamentals and applications*, John Wiley & Sons, New York, **2001**.
[129] Y. Shao, M. V. Mirkin, G. Fish, S. Kokotov, D. Palanker, A. Lewis, *Anal. Chem.* **1997**, *69*, 1627.
[130] R. J. Forster, *Chem. Soc. Rev.* **1994**, *23*, 289.
[131] P. F. Barbara, T. J. Meyer, M. A. Ratner, *J. Phys. Chem.* **1996**, *100*, 13148.
[132] C.-H. Chen, E. R. Ravenhill, D. Momotenko, Y.-R. Kim, S. C. S. Lai, P. R. Unwin, *Langmuir* **2015**, *31*, 11932.
[133] S. V. Sokolov, S. Eloul, E. Kätelhön, C. Batchelor-McAuley, R. G. Compton, *Phy. chem. phys. chem.* **2016**, *19*, 28.
[134] X. Li, C. Batchelor-McAuley, R. G. Compton, *ACS Sens.* **2019**, *4*, 464.
[135] S. E. F. Kleijn, B. Serrano-Bou, A. I. Yanson, M. T. M. Koper, *Langmuir* **2013**, *29*, 2054.
[136] K. Ngamchuea, R. O. D. Clark, S. V. Sokolov, N. P. Young, C. Batchelor-McAuley, R. G. Compton, *Chem. Eur. J.* **2017**, *23*, 16085.
[137] W. Xu, G. Zou, H. Hou, X. Ji, *Small* **2019**, *15*, e1804908.
[138] D. A. Robinson, Y. Liu, M. A. Edwards, N. J. Vitti, S. M. Oja, B. Zhang, H. S. White, *J. Am. Chem. Soc.* **2017**, *139*, 16923.
[139] A. J. Bard, H. Zhou, S. J. Kwon, *Isr. J. Chem.* **2010**, *50*, 267.
[140] T. M. Alligrant, M. J. Anderson, R. Dasari, K. J. Stevenson, R. M. Crooks, *Langmuir* **2014**, *30*, 13462.
[141] C. P. Byers, B. S. Hoener, W.-S. Chang, M. Yorulmaz, S. Link, C. F. Landes, *J. Phys. Chem. B* **2014**, *118*, 14047.
[142] Y.-Y. Peng, R.-C. Qian, M. E. Hafez, Y.-T. Long, *ChemElectroChem* **2017**, *4*, 977.
[143] M. Kang, D. Perry, Y.-R. Kim, A. W. Colburn, R. A. Lazenby, P. R. Unwin, *J. Am. Chem. Soc.* **2015**, *137*, 10902.
[144] S. C. S. Lai, P. V. Dudin, J. V. Macpherson, P. R. Unwin, *J. Am. Chem. Soc.* **2011**, *133*, 10744.
[145] Y.-G. Zhou, N. V. Rees, R. G. Compton, *Angew. Chem.* **2011**, *50*, 4219.
[146] Y. Fang, W. Wang, X. Wo, Y. Luo, S. Yin, Y. Wang, X. Shan, N. Tao, *J. Am. Chem. Soc.* **2014**, *136*, 12584.
[147] S. Kang, A. F. Nieuwenhuis, K. Mathwig, D. Mampallil, S. G. Lemay, *ACS nano* **2013**, *7*, 10931.
[148] C. Ma, N. M. Contento, P. W. Bohn, *J. Am. Chem. Soc.* **2014**, *136*, 7225.
[149] D. Han, L. P. Zaino, K. Fu, P. W. Bohn, *J. Phys. Chem. C* **2016**, *120*, 20634.
[150] J. C. Byers, B. P. Nadappuram, D. Perry, K. McKelvey, A. W. Colburn, P. R. Unwin, *Anal. Chem.* **2015**, *87*, 10450.
[151] A. D. Castañeda, T. M. Alligrant, J. A. Loussaert, R. M. Crooks, *Langmuir* **2015**, *31*, 876.
[152] R. Dasari, D. A. Robinson, K. J. Stevenson, *J. Am. Chem. Soc.* **2013**, *135*, 570.
[153] T. M. Alligrant, R. Dasari, K. J. Stevenson, R. M. Crooks, *Langmuir* **2015**, *31*, 11724.
[154] H. Zhou, F.-R. F. Fan, A. J. Bard, *J. Phys. Chem. Lett.* **2010**, *1*, 2671.
[155] D. Wakerley, A. G. Güell, L. A. Hutton, T. S. Miller, A. J. Bard, J. V. Macpherson, *Chem. Commun.* **2013**, *49*, 5657.
[156] J. Kim, B.-K. Kim, S. K. Cho, A. J. Bard, *J. Am. Chem. Soc.* **2014**, *136*, 8173.

[157] Z. Guo, S. J. Percival, B. Zhang, *J. Am. Chem. Soc.* **2014**, *136*, 8879.
[158] N. P. Sardesai, D. Andreescu, S. Andreescu, *J. Am. Chem. Soc.* **2013**, *135*, 16770.
[159] E. J. E. Stuart, Y.-G. Zhou, N. V. Rees, R. G. Compton, *RSC Adv.* **2012**, *2*, 6879.
[160] C. S. Lim, S. M. Tan, Z. Sofer, M. Pumera, *ACS nano* **2015**, *9*, 8474.
[161] L.-J. Zhao, R.-C. Qian, W. Ma, H. Tian, Y.-T. Long, *Anal. Chem.* **2016**, *88*, 8375.
[162] a) W. Cheng, R. G. Compton, *TrAC, Trends Anal. Chem.* **2014**, *58*, 79; b) L. Chen, E. E. L. Tanner, C. Lin, R. G. Compton, *Chem. Sci.* **2018**, *9*, 152.
[163] T. R. Bartlett, S. V. Sokolov, R. G. Compton, *ChemistryOpen* **2015**, *4*, 600.
[164] N. V. Rees, Y.-G. Zhou, R. G. Compton, *RSC Adv.* **2012**, *2*, 379.
[165] C. A. Little, R. Xie, C. Batchelor-McAuley, E. Kätelhön, X. Li, N. P. Young, R. G. Compton, *Phys. Chem. Chem. Phys.* **2018**, *20*, 13537.
[166] E. J. E. Stuart, K. Tschulik, D. Omanović, J. T. Cullen, K. Jurkschat, A. Crossley, R. G. Compton, *Nanotechnology* **2013**, *24*, 444002.
[167] C. Batchelor-McAuley, J. Ellison, K. Tschulik, P. L. Hurst, R. Boldt, R. G. Compton, *Analyst* **2015**, *140*, 5048.
[168] B. M. Quinn, P. G. van 't Hof, S. G. Lemay, *J. Am. Chem. Soc.* **2004**, *126*, 8360.
[169] S. E. F. Kleijn, S. C. S. Lai, M. T. M. Koper, P. R. Unwin, *Angew. Chem.* **2014**, *53*, 3558.
[170] A. R. Jung, S. Lee, J. W. Joo, C. Shin, H. Bae, S. G. Moon, S. J. Kwon, *J. Am. Chem. Soc* **2015**, *137*, 1762.
[171] a) Y. Wang, X. Shan, N. Tao, *Faraday Discuss.* **2016**, *193*, 9; b) Y. Wang, Z. Cao, Q. Yang, W. Guo, B. Su, *Anal. Chim. Acta* **2019**, *1074*, 1.
[172] S. Zaleski, A. J. Wilson, M. Mattei, X. Chen, G. Goubert, M. F. Cardinal, K. A. Willets, R. P. van Duyne, *Acc. Chem. Res.* **2016**, *49*, 2023.
[173] C. M. Hill, R. Bennett, C. Zhou, S. Street, J. Zheng, S. Pan, *J. Phys. Chem. C* **2015**, *119*, 6760.
[174] C. M. Hill, D. A. Clayton, S. Pan, *Phys. Chem. Chem. Phys.* **2013**, *15*, 20797.
[175] V. Brasiliense, A. N. Patel, A. Martinez-Marrades, J. Shi, Y. Chen, C. Combellas, G. Tessier, F. Kanoufi, *J. Am. Chem. Soc.* **2016**, *138*, 3478.
[176] T. Yuan, W. Wang, *Curr. Opin. Electroche.* **2017**, *6*, 17.
[177] a) L. Bouffier, T. Doneux, *Curr. Opin. Electroche.* **2017**, *6*, 31; b) M. Nirmal, B. O. Dabbousi, M. G. Bawendi, J. J. Macklin, J. K. Trautman, T. D. Harris, L. E. Brust, *Nature* **1996**, *383*.
[178] E. J. Blackie, E. C. Le Ru, P. G. Etchegoin, *J. Am. Chem. Soc.* **2009**, *131*, 14466.
[179] W. Wang, *Chem. Soc. Rev.* **2018**, *47*, 2485.
[180] D. Jiang, Y. Jiang, Z. Li, T. Liu, X. Wo, Y. Fang, N. Tao, W. Wang, H.-Y. Chen, *J. Am. Chem. Soc.* **2017**, *139*, 186.
[181] R. E. Palacios, F.-R. F. Fan, J. Grey, J. Suk, A. J. Bard, P. F. Barbara, *Nat. Mater.* **2007**, *6*, 680.
[182] S. E. Fosdick, M. J. Anderson, E. G. Nettleton, R. M. Crooks, *J. Am. Chem. Soc.* **2013**, *135*, 5994.
[183] Y. Fan, R. Hao, C. Han, B. Zhang, *Anal. Chem.* **2018**, *90*, 13837.
[184] R. Godin, G. Cosa, *J. Phys. Chem. C* **2016**, *120*, 15349.
[185] C. Han, R. Hao, Y. Fan, M. A. Edwards, H. Gao, B. Zhang, *Langmuir* **2019**, *35*, 7180.
[186] a) J. F. Hicks, F. P. Zamborini, R. W. Murray, *J. Phys. Chem. B* **2002**, *106*, 7751; b) Y. Yu, Y. Gao, K. Hu, P.-Y. Blanchard, J.-M. Noël, T. Nareshkumar, K. L. Phani, G.

Friedman, Y. Gogotsi, M. V. Mirkin, *ChemElectroChem* **2015**, *2*, 58; c) M. Miyake, T. Torimoto, M. Nishizawa, T. Sakata, H. Mori, H. Yoneyama, *Langmuir* **1999**, *15*, 2714.
[187] G. Loget, A. Kuhn in *Electrochemistry* (Eds.: J. D. Wadhawan, R. G. Compton), Royal Society of Chemistry, Cambridge, **2012**, pp. 71–103.
[188] J. P. Guerrette, S. M. Oja, B. Zhang, *Anal. Chem.* **2012**, *84*, 1609.
[189] B.-Y. Chang, K.-F. Chow, J. A. Crooks, Mavre. F., R. M. Crooks, *Analyst* **2012**, *137*, 2827.
[190] X. Zhang, C. Chen, J. Li, L. Zhang, E. Wang, *Anal. Chem.* **2013**, *85*, 5335.
[191] J. T. Cox, J. P. Guerrette, B. Zhang, *Anal. Chem.* **2012**, *84*, 8797.
[192] C.-M. Wang, C.-H. Hsieh, C.-Y. Chen, W.-S. Liao, *Anal. Chim. Acta* **2018**, *1015*, 1.
[193] J. Duval, J. M. Kleijn, H. P. van Leeuwen, *J. Electroanal. Chem.* **2001**, *505*, 1.
[194] K.-F. Chow, B.-Y. Chang, B. A. Zaccheo, F. Mavré, R. M. Crooks, *J. Am. Chem. Soc.* **2010**, *132*, 9228.
[195] S. E. Fosdick, R. M. Crooks, *J. Am. Chem. Soc.* **2012**, *134*, 863.
[196] B. Gupta, B. Goudeau, A. Kuhn, *Angew. Chem.* **2017**, *56*, 14183.
[197] W. Wei, G. Xue, E. S. Yeung, *Anal. Chem.* **2002**, *74*, 934.
[198] J.-C. Bradley, H.-M. Chen, J. Crawford, J. Eckert, K. Ernazarova, T. Kurzeja, Lin. M., M. McGee, W. Nadler, S. G. Stephens, *Nature* **1997**, *389*, 268.
[199] S. Inagi, *Polym. J.* **2016**, *48*, 39.
[200] K.-N. Jung, H.-S. Shin, M.-S. Park, J.-W. Lee, *ChemElectroChem* **2019**, *6*, 3842.
[201] X. Ma, L. Qi, W. Gao, F. Yuan, Y. Xia, B. Lou, *Electrochimica. Acta* **2019**, *308*, 20.
[202] R. Hao, Y. Fan, C. Han, B. Zhang, *Anal. Chem.* **2017**, *89*, 12652.
[203] L. Bouffier, N. Sojic, A. Kuhn, *Electrophoresis* **2017**, *38*, 2687.
[204] L. Bouffier, V. Ravaine, N. Sojic, A. Kuhn, *Curr. Opin. Colloid Interface Sci.* **2016**, *21*, 57.
[205] S. M. Oja, J. P. Guerrette, M. R. David, B. Zhang, *Anal. Chem.* **2014**, *86*, 6040.
[206] S. M. Oja, B. Zhang, *Anal. Chem.* **2014**, *86*, 12299.
[207] T. J. Davies, S. Ward-Jones, C. E. Banks, J. del Campo, R. Mas, F. X. Muñoz, R. G. Compton, *J. Electroanal. Chem.* **2005**, *585*, 51.
[208] M.-S. Wu, Z. Liu, H.-W. Shi, H.-Y. Chen, J.-J. Xu, *Anal. Chem.* **2015**, *87*, 530.
[209] F. Zhu, B. Mao, J. Yan, *Rev. Anal. Chem.* **2015**, *34*, 463.
[210] Z. A. Kostiuchenko, B. Zhang, S. G. Lemay, *J. Phys. Chem. C* **2016**, *120*, 22777.
[211] Y.-L. Ying, Y.-T. Long, *Sci. China Chem.* **2017**, *60*, 1187.
[212] R. Gao, Y. Lin, Y.-L. Ying, Y.-X. Hu, S.-W. Xu, L.-Q. Ruan, R.-J. Yu, Y.-J. Li, H.-W. Li, L.-F. Cui et al., *Nat. Protoc.* **2019**, *14*, 2015.
[213] H. Li, L. Bouffier, S. Arbault, A. Kuhn, C. F. Hogan, N. Sojic, *Electrochem. Commun.* **2017**, *77*, 10.
[214] M. Seo, S. Y. Yeon, J. Yun, T. D. Chung, *Electrochimica. Acta* **2019**, *314*, 89.
[215] S. Wu, Z. Zhou, L. Xu, B. Su, Q. Fang, *Biosens. Bioelectron.* **2014**, *53*, 148.
[216] S. A-Long, Z. Xing-Wang, *Chinese J. Anal. Chem.* **2014**, *42*, 1220.
[217] F. Yuan, L. Qi, T. H. Fereja, D. V. Snizhko, Z. Liu, W. Zhang, G. Xu, *Electrochim. Acta* **2018**, *262*, 182.
[218] J.-D. Zhang, T. Yu, J.-Y. Li, J.-J. Xu, H.-Y. Chen, *Electrochem. Commun.* **2014**, *49*, 75.
[219] S. Yu, M. Mehrgardi, C. Shannon, *Electrochem. Commun.* **2018**, *88*, 24.
[220] A. Arora, J. C. T. Eijkel, W. E. Morf, A. Manz, *Anal. Chem.* **2001**, *73*, 3282.

[221] L. Bouffier, D. Manojlovic, A. Kuhn, N. Sojic, *Curr. Opin. Electroche.* **2019**, *16*, 28.
[222] a) L. Bouffier, S. Arbault, A. Kuhn, N. Sojic, *Anal. Bioanal. Chem.* **2016**, *408*, 7003; b) V. Eßmann, C. S. Santos, T. Tarnev, M. Bertotti, W. Schuhmann, *Anal. Chem.* **2018**, *90*, 6267.
[223] W. Xu, K. Fu, P. W. Bohn, *ACS Sens.* **2017**, *2*, 1020.
[224] W. Xu, K. Fu, C. Ma, P. W. Bohn, *Analyst* **2016**, *141*, 6018.
[225] S. Ramakrishnan, C. Shannon, *Langmuir* **2010**, *26*, 4602.
[226] R. Ramaswamy, C. Shannon, *Langmuir* **2011**, *27*, 878.
[227] H. Xing, X. Zhang, Q. Zhai, J. Li, E. Wang, *Anal. Chem.* **2017**, *89*, 3867.
[228] L. Bouffier, T. Doneux, B. Goudeau, A. Kuhn, *Anal. Chem.* **2014**, *86*, 3708.
[229] S. M. Khoshfetrat, H. Khoshsafar, A. Afkhami, M. A. Mehrgardi, H. Bagheri, *Anal. Chem.* **2019**, *91*, 6383.
[230] M.-S. Wu, G.-S. Qian, J.-J. Xu, H.-Y. Chen, *Anal. Chem.* **2012**, *84*, 5407.
[231] V. Eßmann, D. Jambrec, A. Kuhn, W. Schuhmann, *Electrochem. Commun.* **2015**, *50*, 77.
[232] M. Fabien, R. Meallet-Renault, J.-J. Vachon, R. B. Pansu, P. Audebert, *Chem. Commun.* **2008**, 1913.
[233] W. Xu, J. S. Kong, Y.-T. E. Yeh, P. Chen, *Nat. Mater.* **2008**, *7*, 992.
[234] J. Lu, Y. Fan, M. Howard, J. C. Vaughan, B. Zhang, *J. Am. Chem. Soc.* **2017**, *139*, 2964.
[235] D. Qiu, S. Wang, Y. Zheng, Z. Deng, *Nanotechnology* **2013**, *24*, 505707.
[236] Y. Bao, J. Li, Y. Wang, L. Yu, J. Wang, W. Du, L. Lou, Z. Zhu, H. Peng, J. Zhu, *Opt. Mater.* **2012**, *34*, 1588.
[237] Y. Zhang, H. Jiang, W. Ge, Q. Li, X. Wang, *Langmuir* **2014**, *30*, 10910.
[238] J. Zong, Y. Zhu, X. Yang, J. Shen, C. Li, *Chem. Commun.* **2011**, *47*, 764.
[239] D. Magde, G. E. Rojas, P. G. Seybold, *Photochem. Photobiol.* **1999**, *70*, 737.
[240] M. A. Mezour, M. Morin, J. Mauzeroll, *Anal. Chem.* **2011**, *83*, 2378.
[241] A. A. de Thomaz, D. B. Almeida, V. B. Pelegati, H. F. Carvalho, C. L. Cesar, *J. Phys. Chem. B* **2015**, *119*, 4294.
[242] M. A. Medina, P. Schwille, *BioEssays* **2002**, *24*, 758.
[243] C. N. Kirchner, Hallmeier. K. H., R. Szargan, T. Raschke, C. Radehaus, G. Wittstock, *Electroanalysis* **2007**, *19*, 1023.
[244] T. C. Culbertson, C. S. Jacobson, J. M. Ramsey, *Talanta* **2002**, *56*, 365.
[245] A. J. García-Sáez, P. Schwille, *Methods* **2008**, *46*, 116.
[246] W. Becker, *Burst analyzer 2.0*, Becker&Hickl GmbH, Berlin, **2014**.
[247] W. Becker, *The bh TCSPC Handbook*, **2017**.
[248] Y.-G. Kim, S.-K. Oh, R. M. Crooks, *Chem. Mater.* **2004**, *16*, 167.
[249] a) J. J. Michels, J. Huskens, D. N. Reinhoudt, *J. Chem. Soc., Perkin Trans.* **2002**, *2*, 102; b) C. Amantore, A. Chovin, P. Garrigue, L. Servant, N. Sojic, S. Szunerits, L. Thouin, *Anal. Chem.* **2004**, *76*, 7202.
[250] a) M. Nirmal, D. J. Norris, Kuno M., M. G. Bawendi, A. L. Efros, M. Rosen, *Phys. Rev. Lett.* **1995**, *75*, 3728; b) L. A. Efros, M. Rosen, *Phys. Rev. B* **1996**, *54*, 4843; c) A. Tackeuchi, R. Ohtsubo, K. Yamaguchi, M. Murayama, T. Kitamura, T. Kuroda, T. Takagahara, *Appl. Phys. Lett.* **2004**, *84*, 3576.
[251] R. Vinayakan, T. Shanmugapriya, P. V. Nair, P. Ramamurthy, K. G. Thomas, *J. Phys. Chem. C* **2007**, *111*, 10146.

[252] M. J. Bowers, J. R. McBride, S. J. Rosenthal, *J. Am. Chem. Soc.* **2005**, *127*, 15378.
[253] a) W. Han, S. Fan, Q. Li, Y. Hu, *Science* **1997**, *277*, 1287; b) H. J. Queisser, E. E. Haller, *Science* **1998**, *281*, 945; c) J. Goldberger, R. He, Y. Zhang, S. Lee, H. Yan, H.-J. Choi, P. Yang, *Nature* **2003**, *422*, 596; d) H. M. Huang, Y. Wu, H. Feick, N. Tran, E. Weber, P. Yang, *Adv. Mater.* **2001**, *13*, 113.
[254] A. D. Dukes, M. A. Schreuder, J. A. Sammons, J. R. McBride, N. J. Smith, S. J. Rosenthal, *J. Chem. Phys.* **2008**, *129*, 121102.
[255] a) Y. Kim, C. Ippen, T. Greco, J. Lee, M. S. Oh, C. J. Han, A. Wedel, J. Kim, *Opt. Mater. Express* **2014**, *4*, 1436; b) C. Z. Eddy, H. M. Johanesen, J. J. Butler, D. B. Cordes, *Int. J. Undergrad. Res. Creat. Act.* **2015**, *7*, 1; c) B. N. Pal, Y. Ghosh, S. Brovelli, R. Laocharoensuk, V. Klimov, J. A. Hollingsworth, H. Htoon, *Nano. Lett* **2012**, *12*, 331; d) S. Chandramohan, B. D. Ryu, H. K. Kim, C.-H. Hong, E.-K. Suh, *Opt. Lett.* **2011**, *36*, 802.
[256] F. Tam, C. Moran, N. Halas, *J. Phys. Chem. B* **2004**, *108*, 17290.
[257] a) K. Pinwattana, J. Wang, C.-T. Lin, H. Wu, D. Du, Y. Lin, O. Chailapakul, *Biosens. Bioelectron.* **2010**, *26*, 1109; b) J. Debgupta, D. B. Shinde, V. K. Pillai, *Chem. Commun.* **2012**, *48*, 3088.
[258] E. Kuçur, W. Bücking, R. Giernoth, T. Nann, *J. Phys. Chem. B* **2005**, *109*, 20355.
[259] S. Ogawa, K. Hu, F.-R. F. Fan, A. J. Bard, *J. Phys. Chem. B* **1997**, *101*, 5707.
[260] S. N. Inamdar, P. P. Ingole, S. K. Haram, *Chemphyschem* **2008**, *9*, 2574.
[261] E. Kucur, J. Riegler, G. A. Urban, T. Nann, *J. Phys. Chem.* **2003**, *119*, 2333.
[262] C. C. Lima França, Da Silva Terto. E. G., M. V. Dias-Vermelho, A. A. C. Silva, N. O. Dantas, F. C. De. Abreu, *J. Solid State Electrochem.* **2016**, *20*, 2533.
[263] A. L. Efros, M. Rosen, M. Kuno, M. Nirmal, D. J. Norris, M. Bawendi, *Phys. Rev. B* **1996**, *54*, 4843.
[264] V. Babentsov, F. Sizov, *Opto-electron.rev.* **2008**, *16*.
[265] A. C. A. Silva, M. J. B. Silva, da Luz, F. A. C., D. P. Silva, S. V. Deus, N. O. Dantas, *Nano Lett.* **2014**, *14*, 5452.
[266] S. Eloul, R. G. Compton, *J. Phys. Chem. Lett.* **2016**, *7*, 4317.
[267] J. Jiang, G. Oberdörster, P. Biswas, *J. Nanopart. Res.* **2009**, *11*, 77.
[268] K. D. Wegner, N. Hildebrandt, *Chem. Soc. Rev.* **2015**, *44*, 4792.
[269] a) E. P. Petrov, P. Schwille, *Springer Ser. Fluoresc.* **2008**, *6*, 145; b) S. Ito, T. Sugiyama, N. Toitani, G. Katayama, H. Miyasaka, *J. Phys. Chem. B* **2007**, *111*, 2365.
[270] C. Hosokawa, H. Yoshikawa, H. Masuhara, *Phys. Rev. E* **2005**, *72*, 21408.
[271] S. Nath, J. Meuvis, J. Hendrix, S. A. Carl, Y. Engelborghs, *Biophys. J.* **2010**, *98*, 1302.
[272] a) S. Doose, J. M. Tsay, F. Pinaud, S. Weiss, *Anal. Chem.* **2005**, *77*, 2235; b) A. V. R. Murthy, P. Patil, S. Datta, S. Patil, *J. Phys. Chem. C* **2013**, *117*, 13268; c) S. Patra, A. Samanta, *J. Phys. Chem. C* **2013**, *117*, 23313; d) J. J. Peterson, D. J. Nesbitt, *Nano Lett.* **2009**, *9*, 338.
[273] D. Tonti, F. van Mourik, M. Chergui, *Nano Lett.* **2004**, *4*, 2483.
[274] a) A. Fernando, S. Parajuli, M. A. Alpuche-Aviles, *J. Am. Chem. Soc.* **2013**, *135*, 10894; b) S. G. Hickey, D. J. Riley, *Electrochim. Acta* **2000**, *45*, 3277.
[275] M. A. Hines, P. Guyot-Sionnest, *J. Phys. Chem.* **1996**, *100*, 468.
[276] a) T. N. Bhat, M. K. Rajpalke, B. Roul, M. Kumar, S. B. Krupanidhi, N. Sinha, *Phys. Status Solidi B* **2011**, *248*, 2853; b) A. N. Kravtsova, I. A. Pankin, A. P. Budnyk, V. V. Butova, T. A. Lastovina, A. V. Soldatov, *J. Struct. Chem.* **2016**, *57*, 926; c) C. Carrillo-Carrión, S. Cárdenas, B. M. Simonet, M. Valcárcel, *Chem. Commun.* **2009**, 5214.

[277] S. Khazalpour, D. Nematollahi, *RSC Adv.* **2014**, *4*, 8431.
[278] H. M. Al-Bishri, E. H. El-Mossalamy, I. El-Hallag, S. El-Daly, *J. Korean Chem. Soc.* **2011**, *55*, 169.
[279] G. P. McDermott, P. Jones, N. W. Barnett, D. N. Donaldson, P. S. Francis, *Anal. Chem.* **2011**, *83*, 5453.
[280] K. Kalyanasundaram, *Coord. Chem. Rev.* **1982**, *46*, 159.
[281] Y. Li, J. Z. Zhang, *Laser Photonics Rev.* **2010**, *4*, 517.
[282] T. Salafi, K. K. Zeming, Y. Zhang, *Lab chip* **2016**, *17*, 11.

Curriculum vitae

1) Personal details

Name	Abdallatif Alshalfouh
Adreass	Lambertistrasse 51 a, 26121 Oldenburg, Germany
Mobille no	004917662393981
Email address	aalshalfouh-2010@hotmail.com
Nationality	Palestinian
Date of birth	05.01.1988
Social situation	married and have five daughters

2) Qualifications

Year	Qualification	Institute
2006	Graduated secondary school	Abo Obaida secondary school / Gaza
2006-2010	Bachelor in chemistry	Islamic university / Gaza
2011- 2014	master in chemistry	Alazhar University / Gaza
2016- 2020	PhD in physical chemistry	Oldenburg university / Germany

3) Tutoring experience

Year	Institute	Subject
2010-2013	Islamic University / Gaza	Analytical and organic chemistry lab
2016-2019	Oldenburg university / Germany	Physical chemistry lab

4) Languages

Language	Listening level	Speaking level
English	very good	good
German	good	good

5) Courses, lectures or other academic events I attended

1- German courses in Münster, 01-Oct-2015 to 31-Mar-2016.
2- Creative Science Writing organized by graduated school (OLtech), 27 to 28-Apr-2017.
3- Oral Presentation skills in Bremerhaven (OLtech), 05 to 07-Jul-2017
4- English course (OLtech course) between Nov-2017 and Feb-2018
5- GDCh talks inside the university (many lectures)
6- Good scientific practice (OLtech course), 08-May-2018
7- Zeit Selbstmanagement, 12 to 13-Jun-2019
8- English language workshop 2, 03-May-2019
9- Karriereplanung und Kursbestimmung auf dem Weg zur Professur, 28 to 29-Oct-2019
10- Editing, Processing and Analysis of Scientific Images, 10 to 12-Aug-2020

Publications and conferences

1- Alshalfouh, A.; Oezaslan, M.; Dosche, C.; Wittstock, G. Electrochemistry of CdSe Quantum Dots Studied by Single Molecule Spectroscopy. *ChemElectroChem* **2019**, *6*, 1884–1893.

Conference Talks

1- Alshalfouh, A.; Dosche, C.; Wittstock, G.; Electrochemical properties of QDs evaluated by single molecule spectroscopy and time resolved florescence spectroscopy. Central European Conference on Photochemistry, Bad Hofgastein, Austria, 02 to 04-Feb-**2018**

2- Alshalfouh, A.; Dosche, C.; Wittstock, G.; Combination of single particle collision electrochemistry and single molecule spectroscopy. Bunsentagung (117th Kinetics in the real word), Hannover, Germany, 10 to 12-May-**2018**

3- Alshalfouh, A.; Dosche, C.; Wittstock, G.; Studying the residence time of single NPs on the microelectrode surface by single molecule fluorescence spectroscopy. Electrochemical Surface Science: From Fundamentals to Applications, Ulm, Germany, 24 to 26-Sep-**2018**

Conference Posters

4- Alshalfouh, A.; Dosche, C.; Wittstock, G.; Single particle Interactions on mmicroelectrode surfaces. Bunsen Tagung (116th general assembly of the German society for physical chemistry), Kaiserslautern, Germany, 25 to 27-May-**2017**

5- Alshalfouh, A.; Dosche, C.; Wittstock, G.; Study of dynamics and kinetics of individual QD at UME surface. Nanophotonics conference, Barcelona, Spain, 13 to 15-Sep-**2017**

6- Alshalfouh, A.; Dosche, C.; Wittstock, G.; Studying the interaction of NPs at the electrode surface by bipolar electrochemistry. 70th Annual meeting of the international society of electrochemistry, Durban, South Africa, 04 to 09-Aug-**2019**

Declaration of own work

I hereby declare that I have accomplished this personal thesis independently, that I have not utilized other than the cited sources, and that I have expressly denoted all material which has been cited either actually or by content from the pre-owned sources. As indicated by my insight, the substance or parts of this proposal thesis have not been introduced to some other assessment authority and have not been published. The publication recorded under "publications" was made during the dissertation. The thesis has not been submitted, in entire or partially, to another academic university for assessment in a doctoral procedure.

Signature Oldenburg, Aug 20, 2020